



University of Kentucky
UKnowledge

Theses and Dissertations--Electrical and
Computer Engineering

Electrical and Computer Engineering

2015

AVERAGE-VALUE MODELING OF HYSTERESIS CURRENT CONTROL IN POWER ELECTRONICS

Hanling Chen

University of Kentucky, hanling.chen@uky.edu

[Right click to open a feedback form in a new tab to let us know how this document benefits you.](#)

Recommended Citation

Chen, Hanling, "AVERAGE-VALUE MODELING OF HYSTERESIS CURRENT CONTROL IN POWER ELECTRONICS" (2015). *Theses and Dissertations--Electrical and Computer Engineering*. 78.
https://uknowledge.uky.edu/ece_etds/78

This Doctoral Dissertation is brought to you for free and open access by the Electrical and Computer Engineering at UKnowledge. It has been accepted for inclusion in Theses and Dissertations--Electrical and Computer Engineering by an authorized administrator of UKnowledge. For more information, please contact UKnowledge@lsv.uky.edu.

STUDENT AGREEMENT:

I represent that my thesis or dissertation and abstract are my original work. Proper attribution has been given to all outside sources. I understand that I am solely responsible for obtaining any needed copyright permissions. I have obtained needed written permission statement(s) from the owner(s) of each third-party copyrighted matter to be included in my work, allowing electronic distribution (if such use is not permitted by the fair use doctrine) which will be submitted to UKnowledge as Additional File.

I hereby grant to The University of Kentucky and its agents the irrevocable, non-exclusive, and royalty-free license to archive and make accessible my work in whole or in part in all forms of media, now or hereafter known. I agree that the document mentioned above may be made available immediately for worldwide access unless an embargo applies.

I retain all other ownership rights to the copyright of my work. I also retain the right to use in future works (such as articles or books) all or part of my work. I understand that I am free to register the copyright to my work.

REVIEW, APPROVAL AND ACCEPTANCE

The document mentioned above has been reviewed and accepted by the student's advisor, on behalf of the advisory committee, and by the Director of Graduate Studies (DGS), on behalf of the program; we verify that this is the final, approved version of the student's thesis including all changes required by the advisory committee. The undersigned agree to abide by the statements above.

Hanling Chen, Student

Dr. Aaron Cramer, Major Professor

Dr. Caicheng Lu, Director of Graduate Studies

AVERAGE-VALUE MODELING OF HYSTERESIS CURRENT CONTROL IN
POWER ELECTRONICS

DISSERTATION

A dissertation submitted in partial fulfillment of the
requirements for the degree of Doctor of Philosophy in the
College of Engineering at the University of Kentucky

By

Hanling Chen

Lexington, Kentucky

Co-Directors: Dr. Aaron M. Cramer, Assistant Professor of Electrical Engineering
and Dr. Bruce L. Walcott, Professor of Electrical Engineering

Lexington, Kentucky

2015

Copyright© Hanling Chen 2015

ABSTRACT OF DISSERTATION

AVERAGE-VALUE MODELING OF HYSTERESIS CURRENT CONTROL IN POWER ELECTRONICS

Hysteresis current control has been widely used in power electronics with the advantages of fast dynamic response under parameter, line and load variation and ensured stability. However, a main disadvantage of hysteresis current control is the uncertain and varying switching frequency which makes it difficult to form an average-value model. The changing switching frequency and unspecified switching duty cycle make conventional average-value models based on PWM control difficult to apply directly to converters that are controlled by hysteresis current control.

In this work, a new method for average-value modeling of hysteresis current control in boost converters, three-phase inverters, and brushless dc motor drives is proposed. It incorporates a slew-rate limitation on the inductor current that occurs naturally in the circuit during large system transients. This new method is compared with existing methods in terms of simulation run time and rms error. The performance is evaluated based on a variety of scenarios, and the simulation results are compared with the results of detailed models. The simulation results show that the proposed model represents the detailed model well and is faster and more accurate than existing methods. The slew-rate limitation model of hysteresis current control accurately captures the salient detail of converter performance while maintaining the computational efficiency of average-value models. Validations in hardware are also presented.

KEYWORDS: Average-value modeling, boost converter, brushless dc motor drive, dc-dc converter, hysteresis current control, three-phase inverter

Hanling Chen

Student's signature

September 29, 2015

Date

AVERAGE-VALUE MODELING OF HYSTERESIS CURRENT CONTROL IN
POWER ELECTRONICS

By
Hanling Chen

Aaron Cramer
Co-Director of Dissertation

Bruce Walcott
Co-Director of Dissertation

Caicheng Lu
Director of Graduate Studies

September 29, 2015
Date

ACKNOWLEDGMENTS

Firstly, I would like to express my sincere gratitude to my advisor Prof. Aaron Cramer for the continuous support of my Ph.D study and related research, for his patience, motivation, and immense knowledge. His guidance helped me in all the time of research and writing of this thesis.

Besides my advisor, I would like to thank the rest of my thesis committee: Prof. Bruce Walcott, Prof. Yuan Liao, Prof. Joseph Sottile, and Prof. Chi-Sing Man for their insightful comments and encouragement.

My sincere thanks also goes to Dr. Benjamin Loop, for sharing his insights related to this work.

I thank my fellow labmates Fei Pan and Xiao Liu, for helping me with the experiments that were needed for this thesis.

Last but not the least, I would like to thank my parents for their love and support.

TABLE OF CONTENTS

Acknowledgments	iii
Table of Contents	iv
List of Tables	vi
List of Figures	vii
Chapter 1 Introduction	1
Chapter 2 Background and Literature Review	6
2.1 Boost Converter	6
2.2 Three-Phase Inverter	10
2.3 Reference Frame Theory	15
2.4 Hysteresis Current Control	21
Chapter 3 Average-Value Modeling of Hysteresis Current Control in Boost Converter	26
3.1 Previous Approaches	28
3.2 Proposed Approach	32
3.3 Simulation Comparisons	36
3.4 Frequency-Domain Comparison	46
3.5 Experimental Validation	47
3.6 Conclusion	49
Chapter 4 Average-Value Modeling of Hysteresis Current Control in Three- Phase Inverters	53
4.1 Notation	55
4.2 Three-Phase Inverter System	55
4.3 Perfect Hysteresis Current Control Model	58
4.4 Proposed Average-Value Models	59
4.5 Results	65
4.6 Conclusion	72
Chapter 5 Average-Value Modeling of Hysteresis Current Controlled Brush- less DC Motor Drives	73
5.1 Brushless DC Machine	74
5.2 Perfect Hysteresis Model	75
5.3 Proposed Average-Value Models	76
5.4 Simulation Results	81
5.5 Experimental Validation	86

5.6 Conclusion	88
Chapter 6 Conclusion and Future Work	90
Appendix	94
A.1 Bidirectional DC-DC Converter Design	94
A.2 Lab Pictures	101
Bibliography	105
Vita	121

LIST OF TABLES

2.1	Inverter Switching States	13
3.1	Boost Converter Parameters	36
3.2	Efficiency and Accuracy Comparison for Each Method for Case I (i_L^* step)	40
3.3	Efficiency and Accuracy Comparison for Each Method for Case II (v_{in} step)	42
3.4	Efficiency and Accuracy Comparison for Each Method for Case III (R step)	44
3.5	Efficiency and Accuracy Comparison for Each Method for Experiment I (i_L^* step)	48
3.6	Efficiency and Accuracy Comparison for Each Method for Experiment II (R step)	48
4.1	Simulation Results for Case I	68
4.2	Simulation Results for Case II	70
4.3	Simulation Results for Case III	71
5.1	Motor Parameters	83
5.2	Number of Output Calls and RMS Error for Each Method	83
5.3	Number of Output Calls and RMS Error for Each Method	85
5.4	Motor Parameters	87
5.5	Number of Output Calls and RMS Error for Each Method	88

LIST OF FIGURES

2.1	Boost converter	6
2.2	Three-phase inverter with output filter system	11
2.3	Space-vector diagram	13
2.4	Hysteresis current control	23
3.1	Boost converter	29
3.2	Graphically solving output voltage	35
3.3	Relationship between current error and number of time steps for each method for Case I. I–V signify Methods I–V. P signifies the proposed method.	39
3.4	Inductor current for Case I (i_L^* step). D signifies the detailed model. I–V signify Methods I–V. P signifies the proposed method.	40
3.5	Capacitor voltage for Case I (i_L^* step). D signifies the detailed model. I–V signify Methods I–V. P signifies the proposed method.	41
3.6	Inductor current for Case II (v_{in} step). D signifies the detailed model. I–V signify Methods I–V. P signifies the proposed method.	42
3.7	Capacitor voltage for Case II (v_{in} step). D signifies the detailed model. I–V signify Methods I–V. P signifies the proposed method.	43
3.8	Inductor current for Case III (R step). D signifies the detailed model. I–V signify Methods I–V. P signifies the proposed method.	44
3.9	Capacitor voltage for Case III (R step). D signifies the detailed model. I–V signify Methods I–V. P signifies the proposed method.	45
3.10	Transfer function analysis. I–V signify Methods I–V. P signifies the proposed method.	47
3.11	Experimentally measured and simulated inductor current for Experiment I (i_L^* step). D signifies the experimentally measure waveforms. I–V signify Methods I–V. P signifies the proposed method. The waveforms have been low-pass filtered with a time constant of 2 μ s to remove measurement noise. 49	49
3.12	Experimentally measured and simulated capacitor voltage for Experiment I (i_L^* step). D signifies the experimentally measure waveforms. I–V signify Methods I–V. P signifies the proposed method. The waveforms have been low-pass filtered with a time constant of 2 μ s to remove measurement noise. 50	50
3.13	Experimentally measured and simulated inductor current for Experiment II (R step). D signifies the experimentally measure waveforms. I–V signify Methods I–V. P signifies the proposed method. The waveforms have been low-pass filtered with a time constant of 2 μ s to remove measurement noise. 51	51
3.14	Experimentally measured and simulated capacitor voltage for Experiment II (R step). D signifies the experimentally measure waveforms. I–V signify Methods I–V. P signifies the proposed method. The waveforms have been low-pass filtered with a time constant of 2 μ s to remove measurement noise. 52	52

4.1	Three-phase inverter with output filter system	56
4.2	Output filter of a three-phase inverter in synchronous reference frame . .	57
4.3	Grid-connected three-phase inverter in synchronous reference frame . . .	58
4.4	Three regions of inverter voltage capability	59
4.5	Commanded voltage and effective voltage	60
4.6	Region II	62
4.7	Relationship between required and effective modulation index	63
4.8	Experimental Case I inductor current.	67
4.9	Experimental Case I capacitor voltage.	68
4.10	Experimental Case II inductor current.	69
4.11	Experimental Case II capacitor voltage.	70
4.12	Experimental Case III grid current.	71
5.1	Brushless dc motor drive system	75
5.2	Inverter voltage capability in stationary reference frame	76
5.3	Region II	79
5.4	Relationship between commanded and effective modulation index	80
5.5	Closed-loop controller for motor drive	83
5.6	Simulated q - and d -axis currents. D signifies the detailed model. PH signifies perfect hysteresis. EV signifies the effective voltage, SRL signifies slew-rate-limitation. d signifies d-axis currents, q signifies q-axis currents.	84
5.7	Simulated torque. D signifies the detailed model. PH signifies perfect hysteresis. EV signifies the effective voltage, SRL signifies slew-rate-limitation.	84
5.8	Simulated q - and d -axis currents. D signifies the detailed model. PH signifies perfect hysteresis. EV signifies the effective voltage, SRL signifies slew-rate-limitation.	85
5.9	Simulated q - and d -axis torque. D signifies the detailed model. PH signifies perfect hysteresis. EV signifies the effective voltage, SRL signifies slew-rate-limitation.	86
5.10	Simulation comparison	88
5.11	Hardware validation	89

Chapter 1 Introduction

The study of power electronic converters is essential for humanity to begin to address today's energy and environmental challenges. Power converters are used in variable frequency drives (VFD) to allow energy savings to be realized in heating, ventilation, and air conditioning and other facility and industrial applications [1–3]. Motor drives are also prevalent with other power converters in the drivetrains of hybrid electric vehicles [4–6], allowing transportation needs to be met more efficiently and with less pollution [7,8]. Various converters are employed to integrate renewable energy sources such as solar [9,10] and wind [11–13]. The converters are used within power systems to achieve flexible transmission of power [14,15], improve power quality [16,17], and improve system resilience [18], efforts that will ultimately enable a smart grid [19,20]. The study of dc-dc converters has gained importance in applications such as maximum power point tracker (MPPT), fuel cell vehicles [21–23], solar energy harvesting [24], wave energy conversion [25,26], hybrid wind and solar energy systems [27], heat energy recovery [28], power systems [29,30], and smart grid systems. Three-phase inverters play an important role in converting dc power into ac which can be used for connecting the renewable energy to the grid [31–33], or as the uninterruptible power supply (UPS) [34–36]. Motor drives have gained importance with brushless dc motors by becoming widely used in electric vehicles [37–39], aerospace [40–42], robotics [43–45] with the advantages of high efficiency and torque density [46–48].

Pulse width modulation (PWM) and hysteresis current control are two commonly used methods in the control of power converters. PWM controllers are designed at the operating point and are sensitive to parameter variation [49–51]. This usually results in unfavorable situations in today's applications where high performance is required such as maximum power point tracking, wind turbines, and active power

filters [52–54]. Hysteresis current control, on the other hand, with the advantages of ensured stability under parameter, line and load changes, more control bandwidth freedom [55,56], robustness, simple implementation, fast response to supply, load and parameter variations, reduced order system dynamics, automatic protection against overcurrent conditions, constant switching frequency in steady-state and no steady-state errors [52,57,58], has been widely used in active filters, machine drives, and high performance converters [59–69] where a fast response to reference current changes is required.

However, modeling and simulation of hysteresis current control in power electronics have not been discussed much. The primary average-value modeling of hysteresis current control is to model it as perfect hysteresis current control, that is, the actual current is always equal to the commanded current. A few average-value models for hysteresis current controlled dc-dc converters have been proposed. But they all have some limitations and cannot be applied to other power converter topologies directly. Herein, new approaches to model hysteresis current control in dc-dc converters, three-phase inverters, and motor drives are proposed. These approaches demonstrate good accuracy and computational efficiency with respect to existing techniques. The organization of this work is as follows.

Chapter 2 gives background information on boost converters, three-phase inverters, and motor drives. The mathematical representation of the system and the equations for current and voltage state variables are given. In the detailed model of power converters, the actual switching actions are presented. However, if the study of the switching is not of interest, average-value models can be used to dramatically speedup the simulations. The state-space averaging method is reviewed in boost converters. This chapter also describes reference frame theory and the transformation of stationary circuit variables into an arbitrary reference frame. Reference frame transformation is a useful tool in the analysis of three-phase circuits. It can be used to

transform stationary state variables into an arbitrary reference frame. By choosing the right reference frame speed, three-phase ac variables can be transformed into dc values. Then, three-phase ac inverter and motor drive systems can be analyzed using similar methods as dc systems. In this chapter, PWM control in dc-dc converters and three-phase inverters is also reviewed. Compared with PMW control, hysteresis current control has the advantages of simplicity and independence from load or converter parameters. This chapter reviews the advantages and disadvantages of hysteresis current control and research progress to eliminate those disadvantages. Existing average-value modeling of hysteresis current control in dc-dc converters and three-phase inverters are summarized.

Chapter 3 presents average-value modeling of hysteresis current control in boost converters. Five existing average-value models are reviewed and compared with the proposed slew-rate limitation model. The effect of modeling parameters on system accuracy and run time is analyzed. It is found that the proposed method has a tradeoff between simulation run time and accuracy, which offers modeling flexibility. All the methods are evaluated based on the simulation run time and rms error compared with the simulation results from the detailed model. A wide variety of operating scenarios are simulated, such as a step change in current command, a step change in input voltage, and a step change in output resistance. The proposed slew-rate limitation model is found to be as accurate as all the existing methods but is faster. Also, the proposed model as well as all the existing methods are compared with the detailed model in the frequency domain. The proposed slew-rate limitation method accurately predicts the frequency response, so it can be used in applications where the frequency response is needed, such as stability analysis and controller design. Lastly, hardware validation of the proposed method is given.

Chapter 4 presents average-value modeling of hysteresis current control in three-phase inverters. The primary existing method of average-value modeling of hysteresis

current control in three-phase inverters is to model it as perfect hysteresis current control. However, this method cannot accurately model either the transient event such as a step current command or the overmodulation. Large current and voltage errors will be introduced when the inverter is operated under those conditions. This chapter first analyzes the relationship between the commanded voltage and the actual achievable voltage and defines it as the modulation index. Mathematical representation of the modulation index for the three operating regions is formulated. Then the three-phase inverter is transformed into the synchronous reference frame using reference frame theory. Two new methods for average-value modeling of hysteresis current control in three-phase inverters, an effective voltage model and a slew-rate limitation model, are proposed. A wide variety of operating scenarios are simulated, including a step current command change in both the linear operating region and the overmodulation region when the inverter is connected to a three-phase passive load through an LC filter, and a step current command change when the inverter is connected to the grid through an L filter. Hardware validation for those scenarios are also given in this chapter. It is found that the proposed methods are more accurate than the existing perfect hysteresis current control and also maintain the computational efficiency of average-value models.

Chapter 5 presents average-value modeling of hysteresis current control of brushless dc motor drives. Hysteresis current control offers fast and accurate speed and torque control which have become popular with today's applications such as electric vehicles. Unlike a three-phase inverter connected to an output load through an LC filter, the three-phase inverter is connected to a motor directly. This chapter uses the same formula for overmodulation index from the last chapter. The motor drive system is transformed into the rotor reference frame using reference frame theory. Two new proposed methods, an effective voltage model and a slew-rate limitation model, are compared with the existing perfect hysteresis current model in two cases: an

open-loop pulse train step current command and a closed-loop step speed command. It is found that the proposed methods are more accurate than the existing perfect hysteresis current control and are also fast. Hardware validation of an open-loop step current command is also shown.

Chapter 6 summarizes the contribution of this work and suggests potential avenues for future research.

Chapter 2 Background and Literature Review

This chapter gives background information on boost converters, three-phase inverters, and reference frame theory. The state-space averaging method is reviewed in boost converters. In this chapter, PWM control in dc-dc converters and three-phase inverters is also reviewed. Compared with PMW control, hysteresis current control has the advantages of simplicity and independence from load or converter parameters. This chapter reviews the advantages and disadvantages of hysteresis current control and research progress to eliminate those disadvantages. Existing average-value modeling of hysteresis current control in dc-dc converters and three-phase inverters are summarized.

2.1 Boost Converter

A boost converter, which is also called a step up converter, produces an output dc voltage that is higher than the input dc voltage. A figure of a boost converter is shown in Figure 2.1. It consists of an inductor with inductance L , a capacitor with capacitance C , and two switches D_1 and D_2 . In practice, there are also series

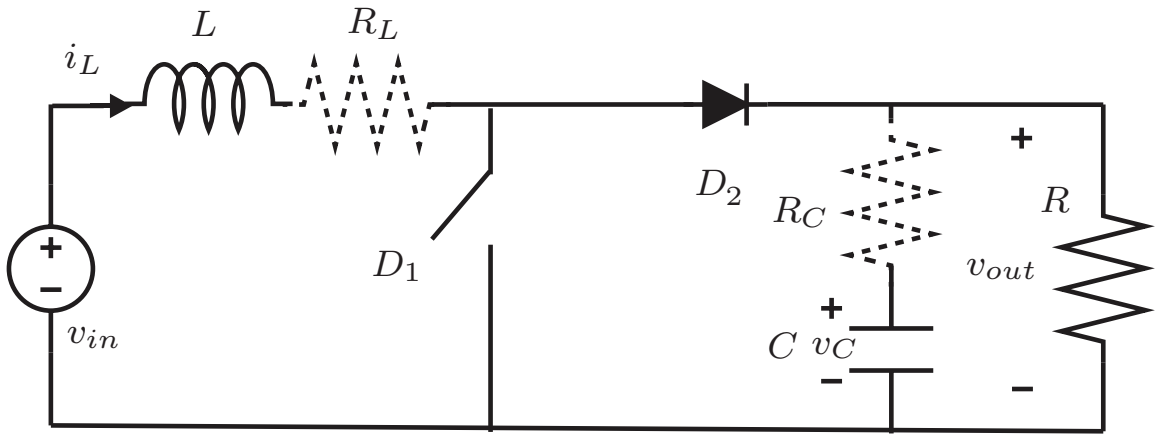


Figure 2.1: Boost converter

resistances R_L and R_C associated with the inductor and capacitor, respectively. Those series resistances are neglected in this chapter. Throughout this work, the switches are being considered as ideal switches. D_1 is capable of blocking voltage in the forward direction or conducting current in the reverse direction. D_1 is usually a transistor that can be opened and closed at will. D_2 is capable of blocking voltage in the reverse direction or conducting current in the forward direction. D_2 is typically a diode and switches on and off based on circuit voltages and currents without external control. By Kirchhoff's voltage law (KVL), both switches cannot be closed at the same time. By Kirchhoff's current law (KCL), at least one switch must be closed whenever current is flowing through the inductor.

When this circuit operates in continuous conduction mode (i.e., the inductor current is always positive), the circuit can be analyzed using two switching topologies: when only D_1 is on and when only D_2 is on. When D_1 is on and D_2 is off, the state equations for the inductor current and capacitor voltage can be expressed as follows:

$$L \frac{di_L}{dt} = v_{in} \quad (2.1)$$

$$C \frac{dv_C}{dt} = -\frac{v_C}{R}. \quad (2.2)$$

These equations can be represented in state-space form as

$$\begin{bmatrix} \dot{i}_L \\ \dot{v}_C \end{bmatrix} = \begin{bmatrix} 0 & 0 \\ 0 & -\frac{1}{RC} \end{bmatrix} \begin{bmatrix} i_L \\ v_C \end{bmatrix} + \begin{bmatrix} \frac{1}{L} \\ 0 \end{bmatrix} v_{in}. \quad (2.3)$$

In this case, the voltage across the inductor can be expressed as

$$v_L = v_{in}. \quad (2.4)$$

When D_1 is off and D_2 is on, the state equations for the inductor current and capacitor voltage can be expressed as follows:

$$L \frac{di_L}{dt} = v_{in} - v_C \quad (2.5)$$

$$C \frac{dv_C}{dt} = i_L - \frac{v_C}{R}. \quad (2.6)$$

These equations can be represented in state-space form as

$$\begin{bmatrix} \dot{i}_L \\ \dot{v}_C \end{bmatrix} = \begin{bmatrix} 0 & -\frac{1}{L} \\ \frac{1}{C} & -\frac{1}{RC} \end{bmatrix} \begin{bmatrix} i_L \\ v_C \end{bmatrix} + \begin{bmatrix} \frac{1}{L} \\ 0 \end{bmatrix} v_{in}. \quad (2.7)$$

In this case, the voltage across the inductor can be expressed as

$$v_L = v_{in} - v_{out}. \quad (2.8)$$

If in one cycle, the time when D_1 is on is d , and the time when D_2 is on is $1-d$, then the average voltage across the inductor is

$$v_{Lavg} = dv_{in} + (1-d)(v_{in} - v_{out}). \quad (2.9)$$

In steady-state operation, the average voltage across an inductor is zero in one period. So the input and output voltage has the following relationship in a boost converter

$$v_{out} = \frac{v_{in}}{1-d}. \quad (2.10)$$

From input and output power conservation, the input and output current in a boost converter has the following relationship

$$i_{out} = (1-d)i_{in}. \quad (2.11)$$

Simulation models are useful tools for power electronics design and analysis. The state-space equations can be solved by simulation programs such as Matlab/Simulink. Basically, there are two types of modeling: detailed modeling and average-value modeling. A detailed model of the converter can be realized by switching back and forth between the two sets of state-space equations shown above. Detailed model simulations are very accurate because they model the actual switching of the devices, but they take a long time to execute because state variables do not reach steady-state

values. Persistent switching between topologies causes the ordinary differential equation (ODE) solver to reset periodically. When the exact device switching details (e.g., ripple voltages and currents) are not of interest, average-value models can be used to speed up the simulation. The average-value model reflects the average value of a circuit state variable during one switching period. At high switching frequency, the inductor current and the capacitor voltage change linearly during each of the two switching subintervals and the ripple waveforms are similar to triangular waveforms. Thus, the derivative of the input current and output voltage, which are slopes of the waveforms, can be treated as constants. The state equation when D_1 is on and D_2 is off can be written as

$$\dot{\mathbf{x}} = \mathbf{A}_1 \mathbf{x} + \mathbf{B}_1 \mathbf{u}, \quad (2.12)$$

and the state equation when D_1 is off and D_2 is on can be written as

$$\dot{\mathbf{x}} = \mathbf{A}_2 \mathbf{x} + \mathbf{B}_2 \mathbf{u}. \quad (2.13)$$

It is assumed that (2.12) holds for dT and (2.13) holds for $(1 - d)T$ in one cycle, where d is the duty cycle and T is the period. Averaging over one switching period and neglecting higher order terms results in the average-value state equation [70]:

$$\bar{\dot{\mathbf{x}}} = \bar{\mathbf{A}} \bar{\mathbf{x}} + \bar{\mathbf{B}} \bar{\mathbf{u}}, \quad (2.14)$$

where

$$\bar{\mathbf{A}} = d\mathbf{A}_1 + (1 - d)\mathbf{A}_2 \quad (2.15)$$

$$\bar{\mathbf{B}} = d\mathbf{B}_1 + (1 - d)\mathbf{B}_2, \quad (2.16)$$

and the quantities $\bar{\mathbf{x}}$ and $\bar{\mathbf{u}}$ represent the average values over one switching period of \mathbf{x} and \mathbf{u} , respectively. The average-value model can be expressed as

$$\begin{bmatrix} \dot{i}_L \\ \dot{v}_C \end{bmatrix} = \begin{bmatrix} 0 & -\frac{1}{L}(1 - d) \\ \frac{1}{C}(1 - d) & -\frac{1}{RC} \end{bmatrix} \begin{bmatrix} i_L \\ v_C \end{bmatrix} + \begin{bmatrix} \frac{1}{L} \\ 0 \end{bmatrix} v_{in}. \quad (2.17)$$

It can be noted that the above equation depends on d . In the average-value model, the steady-state values of the state variables are constant, which makes it easier to analyze and simulate the system.

The output voltage of a dc-dc converter is controlled by the duration of switching on and off time. One way to control the output of boost converters is to control the duty cycle d directly, such as PWM. In this method, a 0 to 1 triangle wave signal is compared with the duty cycle d . The frequency of the triangle wave determines the switching frequency. In PWM control, the switching frequency is constant and usually ranging from a few kilohertz to a few hundred kilohertz. This control method will output a 0 when the triangle wave is larger than the duty cycle, and will output a 1 when the triangle wave is less than the duty cycle. The 0 and 1 signal is being used to control the turn on and off of the switches in dc-dc converters. PWM control has the advantage of fixed frequency, which makes output filter design easily. The disadvantage of PWM control is that the controller is usually tuned for a specific operating point. It has limited dynamic performance where a large operating range is desired [71].

2.2 Three-Phase Inverter

Three-phase inverters change the dc input voltage to a three-phase ac output voltage where amplitude, frequency and phase can be controlled. They are widely used in active filters, motor drives, and renewable energy grid connections [53, 72–74].

A basic three-phase inverter with an LC filter is shown in Figure 4.1. As can be seen, it consists of six switches and freewheeling diodes which forms the three-phase legs. The switches in each phase leg are switched in a complementary manner.

From Figure 4.1, the three-phase output line to neutral voltages can be expressed as [75]

$$v_{an} = v_{ag} - v_{ng} \quad (2.18)$$

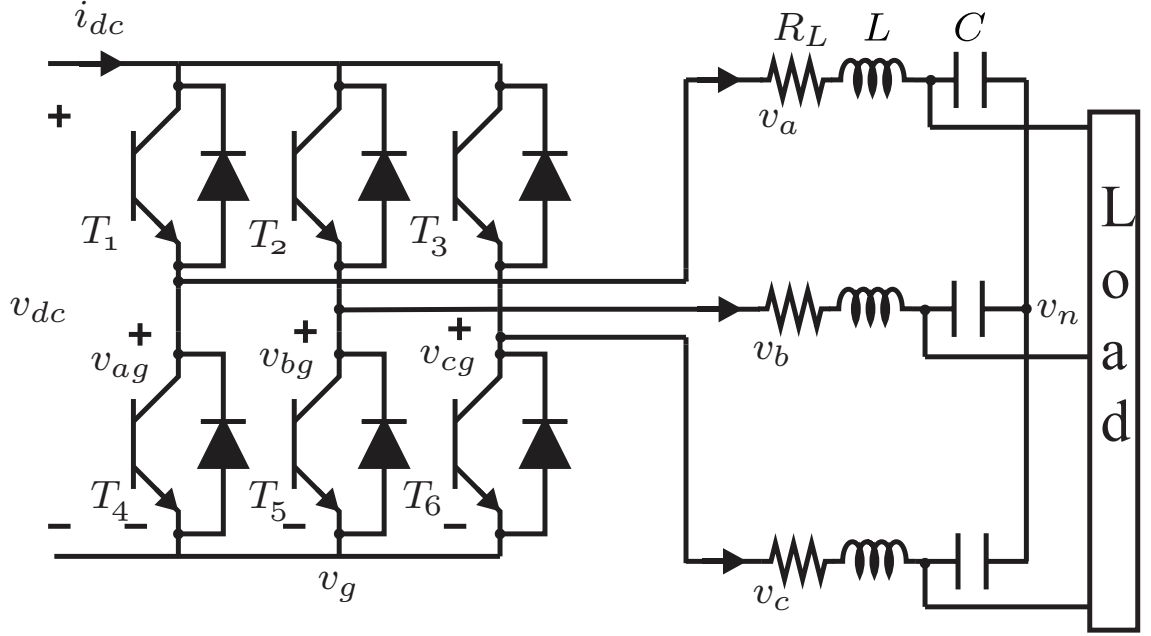


Figure 2.2: Three-phase inverter with output filter system

$$v_{bn} = v_{bg} - v_{ng} \quad (2.19)$$

$$v_{cn} = v_{cg} - v_{ng}, \quad (2.20)$$

where v_{ag} , v_{bg} , v_{cg} are the lower switches' voltages of the three-phase inverter, and v_{ng} is the difference between two neutral voltages. By summing (2.18) – (2.20) and observing the voltages in a balanced three-phase system sum to zero, the neutral-to-ground voltage can be calculated as

$$v_{an} + v_{bn} + v_{cn} = 0, \quad (2.21)$$

v_{ng} can be calculated to be

$$v_{ng} = \frac{v_{ag} + v_{bg} + v_{cg}}{3}. \quad (2.22)$$

Substitution of (2.22) into (2.18) – (2.20), allows the voltage equations to be expressed

in matrix form as

$$\begin{bmatrix} v_{an} \\ v_{bn} \\ v_{cn} \end{bmatrix} = \frac{1}{3} \begin{bmatrix} 2 & -1 & -1 \\ -1 & 2 & -1 \\ -1 & -1 & 2 \end{bmatrix} \begin{bmatrix} v_{ag} \\ v_{bg} \\ v_{cg} \end{bmatrix}. \quad (2.23)$$

One way to analyze the three-phase voltages is to use space vector representation. The q - and d -axis modulation indexes are defined as the q - and d -axis voltages in the stationary reference frame normalized to the dc voltage:

$$m_q = \frac{v_q}{v_{dc}} \quad (2.24)$$

$$m_d = \frac{v_d}{v_{dc}}, \quad (2.25)$$

where v_q and v_d are the q - and d -axis voltages and v_{dc} is the dc input voltage. The six switches in the three legs have a combination of eight switching states. The space vector diagram is shown in Figure 2.3. Those switching states and the corresponding q - and d -axis vectors are shown in Table 2.1 [75], where $m_{q,x}$ and $m_{d,x}$ are the x th q - and d -axis modulation indexes, respectively. Notice that the voltage vectors have a magnitude of $\frac{2}{3}$ of the input dc voltage.

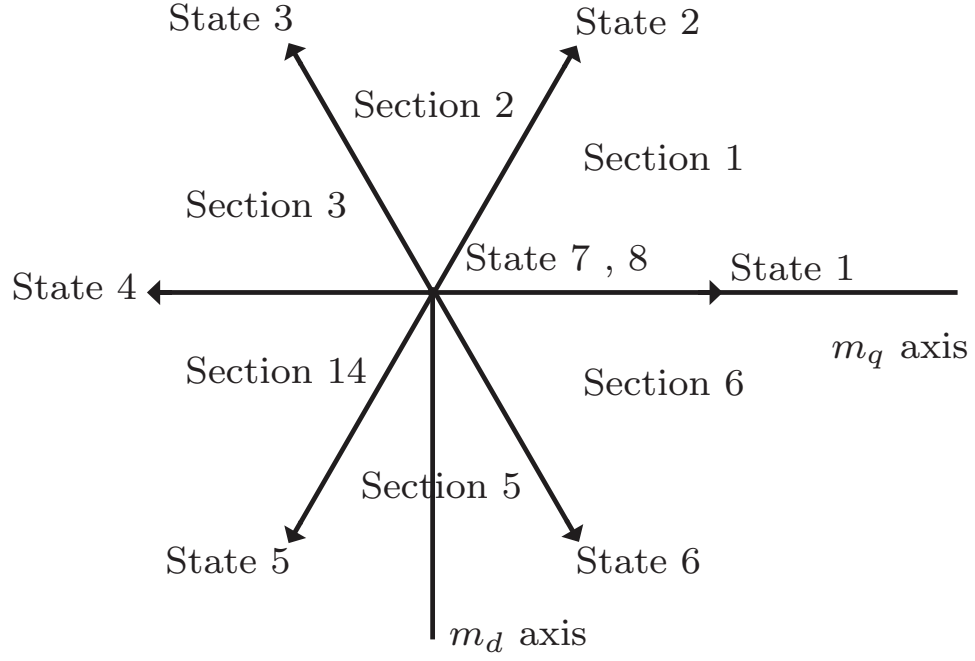


Figure 2.3: Space-vector diagram

Table 2.1: Inverter Switching States

State	T_1/\bar{T}_4	T_2/\bar{T}_5	T_3/\bar{T}_6	$m_{q,x}$	$m_{d,x}$
1	1	0	0	$\frac{2}{3}\cos(0^\circ)$	$-\frac{2}{3}\sin(0^\circ)$
2	1	1	0	$\frac{2}{3}\cos(60^\circ)$	$-\frac{2}{3}\sin(60^\circ)$
3	0	1	0	$\frac{2}{3}\cos(120^\circ)$	$-\frac{2}{3}\sin(120^\circ)$
4	0	1	1	$\frac{2}{3}\cos(180^\circ)$	$-\frac{2}{3}\sin(180^\circ)$
5	0	0	1	$\frac{2}{3}\cos(240^\circ)$	$-\frac{2}{3}\sin(240^\circ)$
6	1	0	1	$\frac{2}{3}\cos(300^\circ)$	$-\frac{2}{3}\sin(300^\circ)$
7	1	1	1	0	0
8	0	0	0	0	0

Many control techniques have been developed for three-phase inverters, such as PWM, sine-triangle modulation, third-harmonic injection, space vector modulation, and hysteresis current control [75]. Among them, PWM, sine-triangle modulation, and third-harmonic injection are based on controlling the duty cycle d but with different reference signals. PWM control is the most basic form and it controls the

fundamental component of the output voltage. In PWM, the duty cycle is varying between 0 and 1, and the reference signal is a triangle waveform which is also varying between 0 and 1. PWM has the disadvantage of low-frequency harmonics [75]. To solve this problem, sine-triangle modulation is introduced. In sine-triangle modulation, the duty cycle is varying according to a sinusoidal waveform and is being compared to a triangle waveform which is varying between -1 and 1 . Sine-triangle modulation has the disadvantage that the output line-to-neutral peak voltage is limited to $\frac{v_{dc}}{2}$, whereas simple duty cycle modulation has an amplitude of $\frac{2v_{dc}}{\pi}$ [75]. The amplitude can be increased further in sine-triangle modulation by operating in the overmodulation region at the cost of introducing low-frequency harmonics. In this case, the duty cycle d is larger than 1. Third-harmonic injection, which is based on sine-triangle modulation, can increase the line-to-neutral peak voltage. The injected third-harmonic term can reduce the peak value of the phase duty-cycle waveforms [75]. The duty cycle can be increased to $\frac{2}{\sqrt{3}}$ without operating in the overmodulation region. The fundamental component of the line-to-neutral voltage is increased to $\frac{v_{dc}}{\sqrt{3}}$. Another PWM control method is the space vector modulation. It has the advantage of better dc bus utilization and lower frequency harmonic distortion. This method is particular designed to work with voltage commands in qd variables.

Space vector modulation is conceptually different from PWM methods [76]. Comparisons between sine-triangle modulation and space vector modulation are presented in [77–80]. In [77], the relationship between space vector modulation and regular-sampled PWM is studied in both three-phase inverters and rectifiers. It is found that by using the null-vectors in space vector modulation and third harmonic injection in sine-triangle modulation, the two methods can have the same output waveform under certain conditions. Analytical expression is derived for space vector modulation that results in minimum total current harmonic distortion. It is shown in [78] that the space vector modulation can be viewed as a particular form of PWM. A comprehen-

sive analysis of the relationship between sine-triangle modulation and space vector modulation is given in [79]. The relationships between the modulation signals and space vector sectors, the switching pattern of space vector modulation and the type of PWM modulation are given. It is shown in [80] that the space vector modulation is identical to double-sided third harmonic injected PWM.

Operating in the overmodulation region has the advantage of better dc input voltage utilization. It is beneficial in the cost perspective. This is also important for electric vehicles to increase the speed range with limited power [81], achieve fast dynamic torque, and high speed operation [82]. An overmodulation PWM drive is proposed in [83] for permanent magnet synchronous motor. An algorithm to generate the reference current in the overmodulation region to improve the dynamic and steady-state performance of a permanent magnetic synchronous machine is proposed in [84]. Overmodulation strategies for induction motor drives are proposed in [82, 85]. A generalized overmodulation method for current regulated three-phase voltage source inverters is proposed in [86].

2.3 Reference Frame Theory

Reference frame theory was first introduced in machines to eliminate the time varying inductance when the rotor rotates [87]. By choosing the right reference frame speed, voltage and current in three-phase ac values can be transformed into constant dc values. Reference frame transformation has become a useful tool for modeling [88–90] and control [91–93] of three-phase circuits. Usually, the electrical reference frame is chosen as the synchronous reference frame in three-phase inverters, and the rotor reference frame is used in synchronous motor drives. Transformation of three-phase variables in the stationary reference frame to an arbitrary reference frame can be

expressed as [75]

$$\mathbf{f}_{qd0s} = \mathbf{K}_s \mathbf{f}_{abcs}, \quad (2.26)$$

where

$$\mathbf{f}_{qd0s} = [f_{qs} \ f_{ds} \ f_{0s}]^T \quad (2.27)$$

$$\mathbf{f}_{abcs} = [f_{as} \ f_{bs} \ f_{cs}]^T \quad (2.28)$$

$$\mathbf{K}_s = \frac{2}{3} \begin{bmatrix} \cos \theta & \cos(\theta - \frac{2\pi}{3}) & \cos(\theta + \frac{2\pi}{3}) \\ \sin \theta & \sin(\theta - \frac{2\pi}{3}) & \sin(\theta + \frac{2\pi}{3}) \\ \frac{1}{2} & \frac{1}{2} & \frac{1}{2} \end{bmatrix} \quad (2.29)$$

$$\omega = \frac{d\theta}{dt}. \quad (2.30)$$

In the above equations, \mathbf{f} can represent voltage, current, or other circuit variables, \mathbf{f}_{abc} is the vector representation of three-phase quantities in abc variables, and \mathbf{f}_{qd0} is the vector representation of the transformed quantities in $qd0$ variables, and θ is the position of the reference frame. The inverse transformation \mathbf{K}_s^{-1} is

$$\mathbf{K}_s^{-1} = \begin{bmatrix} \cos \theta & \sin \theta & 1 \\ \cos(\theta - \frac{2\pi}{3}) & \sin(\theta - \frac{2\pi}{3}) & 1 \\ \cos(\theta + \frac{2\pi}{3}) & \sin(\theta + \frac{2\pi}{3}) & 1 \end{bmatrix}. \quad (2.31)$$

Three basic circuits will be analyzed using the reference frame transformation: a resistive circuit, an inductive circuit, and a capacitive circuit.

In a three-phase resistive circuit, the voltage and current has the relationship

$$\mathbf{v}_{abcs} = \mathbf{r}_s \mathbf{i}_{abcs}, \quad (2.32)$$

where \mathbf{r}_s is the matrix representation of the three-phase resistances in the form

$$\begin{bmatrix} r_{as} & 0 & 0 \\ 0 & r_{bs} & 0 \\ 0 & 0 & r_{cs} \end{bmatrix}. \quad (2.33)$$

From (2.26)

$$\mathbf{v}_{qd0s} = \mathbf{K}_s \mathbf{r}_s (\mathbf{K}_s^{-1}) \mathbf{i}_{qd0s}. \quad (2.34)$$

In a balanced three-phase circuit, the three-phase resistances have equal value

$$r_{as} = r_{bs} = r_{cs} = r_s, \quad (2.35)$$

and

$$\mathbf{K}_s \mathbf{r}_s (\mathbf{K}_s^{-1}) = \mathbf{r}_s. \quad (2.36)$$

So, in a balanced three-phase resistive circuit, the voltage and current have the following relationship in the $qd0$ reference frame:

$$v_{qs} = r_s \dot{i}_{qs} \quad (2.37)$$

$$v_{ds} = r_s \dot{i}_{ds} \quad (2.38)$$

$$v_{0s} = r_s \dot{i}_{0s}. \quad (2.39)$$

In a three-phase inductive circuit, the voltage can be expressed as

$$\mathbf{v}_{abcs} = p \boldsymbol{\lambda}_{abcs}, \quad (2.40)$$

where p is the derivative operator, and $\boldsymbol{\lambda}_{abcs}$ is the vector representation of three-phase flux linkages, which can be expressed as

$$\boldsymbol{\lambda}_{abcs} = \mathbf{L}_s \mathbf{i}_{abcs}, \quad (2.41)$$

where \mathbf{L}_s is the matrix representation of the three-phase inductances. From (2.26)

$$\mathbf{v}_{qd0s} = \mathbf{K}_s p [\mathbf{K}_s^{-1} \boldsymbol{\lambda}_{qd0s}]. \quad (2.42)$$

Using the product rule of derivative and trigonometric identities, the above equation can be simplified into

$$\begin{bmatrix} v_{qs} \\ v_{ds} \\ v_{0s} \end{bmatrix} = \omega \begin{bmatrix} 0 & 1 & 0 \\ -1 & 0 & 0 \\ 0 & 0 & 0 \end{bmatrix} \begin{bmatrix} \lambda_{qs} \\ \lambda_{ds} \\ \lambda_{0s} \end{bmatrix} + p \begin{bmatrix} \lambda_{qs} \\ \lambda_{ds} \\ \lambda_{0s} \end{bmatrix}. \quad (2.43)$$

In a balanced three-phase inductive circuit, the three-phase inductances are the same, and \mathbf{L}_s is a diagonal matrix with equal value. So the voltage equations for a three-phase inductive circuit in the $qd0$ reference frame can be expressed as

$$v_{qs} = \omega L_s i_{ds} + L_s p i_{qs} \quad (2.44)$$

$$v_{ds} = -\omega L_s i_{qs} + L_s p i_{ds} \quad (2.45)$$

$$v_{0s} = L_s p i_{0s}. \quad (2.46)$$

In brushless dc motors, the flux linkage is

$$\boldsymbol{\lambda}_{abcs} = \mathbf{L}_s \mathbf{i}_{abcs} + \boldsymbol{\lambda}'_m, \quad (2.47)$$

where \mathbf{L}_s has both the self inductance of each phase winding and mutual inductance between windings [75]:

$$\mathbf{L}_s = \begin{bmatrix} L_{asas} & L_{asbs} & L_{ascs} \\ L_{asbs} & L_{bsbs} & L_{bscs} \\ L_{ascs} & L_{bscs} & L_{cscs} \end{bmatrix}, \quad (2.48)$$

$$L_{asas} = L_{ls} + L_A - L_B \cos 2\theta_r \quad (2.49)$$

$$L_{asbs} = -\frac{1}{2}L_A - L_B \cos 2(\theta_r - \frac{\pi}{3}) \quad (2.50)$$

$$L_{ascs} = -\frac{1}{2}L_A - L_B \cos 2(\theta_r + \frac{\pi}{3}) \quad (2.51)$$

$$L_{bsbs} = L_{ls} + L_A - L_B \cos 2(\theta_r - \frac{2\pi}{3}) \quad (2.52)$$

$$L_{bscs} = -\frac{1}{2}L_A - L_B \cos 2(\theta_r + \pi) \quad (2.53)$$

$$L_{cscs} = L_{ls} + L_A - L_B \cos 2(\theta_r + \frac{2\pi}{3}), \quad (2.54)$$

where L_{ls} is the stator leakage inductance, L_{asas} , L_{bsbs} , L_{cscs} are self inductance of each phase winding, and L_{asbs} , L_{ascs} , L_{bscs} are mutual inductance between phase windings,

$$L_A = \left(\frac{N_s}{2}\right)^2 \pi \mu_0 r l \alpha_1 \quad (2.55)$$

$$L_B = \frac{1}{2} \left(\frac{N_s}{2}\right)^2 \pi \mu_0 r l \alpha_2, \quad (2.56)$$

N_s is the total equivalent turns per phase, l is the axial length of the air gap of the machine, r is the radius to the mean of the air gap, $(\alpha_1 + \alpha_2)^{-1}$ is the minimum air-gap length and $(\alpha_1 - \alpha_2)^{-1}$ is the maximum, λ'_m is the flux linkage associated with the permanent magnetic which can be expressed as

$$\lambda'_m = \lambda'_m \begin{bmatrix} \sin \theta_r \\ \sin(\theta_r - \frac{2\pi}{3}) \\ \sin(\theta_r + \frac{2\pi}{3}) \end{bmatrix}, \quad (2.57)$$

where θ_r is the rotor position. So the voltage equations for a brushless dc motor in the $qd0$ reference frame can be expressed as

$$v_{qs}^r = \omega_r (L_d i_{ds}^r + \lambda_m^r) + L_q p i_{qs}^r \quad (2.58)$$

$$v_{ds}^r = -\omega_r L_q i_{qs}^r + L_d p i_{ds}^r \quad (2.59)$$

$$v_{0s}^r = L_{ls} p i_{0s}^r, \quad (2.60)$$

where p is the derivative operator, $\omega_r = \frac{d\theta_r}{dt}$, L_{ls} is the leakage inductance, $L_q = L_{ls} + L_{mq}$, $L_d = L_{ls} + L_{md}$, and L_{mq} and L_{md} are magnetizing inductances:

$$L_{mq} = \frac{3}{2} (L_A - L_B) \quad (2.61)$$

$$L_{md} = \frac{3}{2} (L_A + L_B). \quad (2.62)$$

In a three-phase capacitive circuit, the current can be expressed as

$$\mathbf{i}_{abcs} = p\mathbf{q}_{abcs}, \quad (2.63)$$

where

$$\mathbf{q}_{abcs} = \mathbf{C}_s \mathbf{v}_{abcs}, \quad (2.64)$$

\mathbf{C}_s is the matrix representation of the three-phase capacitances. Similar to a three-phase inductive circuit, \mathbf{C}_s will be a diagonal matrix with equal values in a balanced three-phase circuit. From (2.26)

$$\mathbf{i}_{qd0s} = \mathbf{K}_s p[\mathbf{K}_s^{-1} \mathbf{q}_{qd0s}]. \quad (2.65)$$

The above equation can be simplified by using the product rule for derivative and trigonometric identities. So the current equations for a three-phase capacitive circuit in the $qd0$ reference frame can be expressed as

$$i_{qs} = \omega C_s v_{ds} + C_s p v_{qs} \quad (2.66)$$

$$i_{ds} = -\omega C_s v_{qs} + C_s p v_{ds} \quad (2.67)$$

$$i_{0s} = C_s p v_{0s}, \quad (2.68)$$

where p is the derivative operator. By combining the three basic circuit elements, complicated systems such as three-phase inverters with an LC filter and series resistance connected to a passive load, three-phase inverters with an L filter and series resistance connected to the grid, and brushless dc motors with series resistance, can be modeled and analyzed in the $qd0$ reference frame.

A balanced three-phase current or voltage can be expressed as

$$f_{as} = \sqrt{2} f_s \cos \theta_{ef} \quad (2.69)$$

$$f_{bs} = \sqrt{2} f_s \cos(\theta_{ef} - \frac{2\pi}{3}) \quad (2.70)$$

$$f_{cs} = \sqrt{2} f_s \cos(\theta_{ef} + \frac{2\pi}{3}), \quad (2.71)$$

where f_s is the rms value, f_{as} , f_{bs} , and f_{cs} represent three-phase current or voltage, and

$$\omega_e = \frac{d\theta_{ef}}{dt}. \quad (2.72)$$

Applying the arbitrary reference transformation on the three-phase variables yields

$$f_{qs} = \sqrt{2}f_s \cos(\theta_{ef} - \theta) \quad (2.73)$$

$$f_{ds} = -\sqrt{2}f_s \sin(\theta_{ef} - \theta) \quad (2.74)$$

$$f_{0s} = 0. \quad (2.75)$$

As can be seen, the 0- axis quantities in a balanced three-phase circuit is zero.

2.4 Hysteresis Current Control

PWM [94,95] and hysteresis current control [96,97] are two commonly used methods in the control of power converters. PWM has the advantage of fixed switching frequency which makes the output filter design easily. The disadvantage of PWM is that the controller is usually tuned and there is a tradeoff between dynamic performance over a wide operating range and the performance at a specific operating point [71]. On the other hand, hysteresis current control has the advantages of robust control, ensured stability and fast dynamic response under parameter, line, and load variation, and offers greater control bandwidth [98]. These advantages derive from the fact that hysteresis current control is a form of sliding mode control [99]; a converter operating under hysteresis current control exhibits reduced-order system dynamics in steady-state. Simple hardware implementations are possible using analog comparators, and in certain topologies hysteresis current control can provide automatic protection against overcurrent conditions. For these reasons, hysteresis current control has been widely used in dc-dc converters [59–69, 100–102], motor drives [103–105], distribution systems [66], motion control, filters, inverters [73, 106–109], UPS [110, 111], power delivering, grid connected renewable energy [112–115], and battery chargers [116].

In hysteresis control, two switching boundaries, high and low, are defined in terms of a single state variable [117]. Two boundaries with a small separation control the switches' turn-on and turn-off actions. Hysteresis current control for a converter is shown in Figure 2.4. The commanded current is i^* . The upper and lower control boundaries, $i^* + h$ and $i^* - h$, are specified by the desired performance, where h is the hysteresis band. The current will start increasing after the circuit is activated. When the current reaches the control band, switching actions will control the circuit. If the current hits the upper boundary, the switches will change to a state to decrease the current. If the current hits the lower boundary, the switches will change to another state to increase the current. If the current is between the two boundaries, no switching actions will be taken. In dc-dc converters, the hysteresis current control will control the inductor current to follow the commanded current, which is usually a constant value. In three-phase inverters and motor drives, the hysteresis current control will control the three-phase inductor current to follow the commanded current, which is usually a sinusoidal waveform for each phase.

Despite its implementation simplicity, hysteresis current control has suffered from some disadvantages as well. In its most basic form, hysteresis current control results in an uncertain and varying switching frequency. This can complicate filter design as the switching harmonics may have varying frequencies associated with them. This difficulty can be largely alleviated by adaptive techniques that stabilize the switching frequency [118–129]. Another disadvantage is difficulty with digital implementation. With a discrete-time process executing with a fixed period, switching frequency jitter can be introduced, but this effect can also be mitigated by more sophisticated digital implementations [130]. These implementations involve improving the timing resolution of the switching events such that switching events can occur between current samples.

Another disadvantage of hysteresis current control is modeling difficulty. While

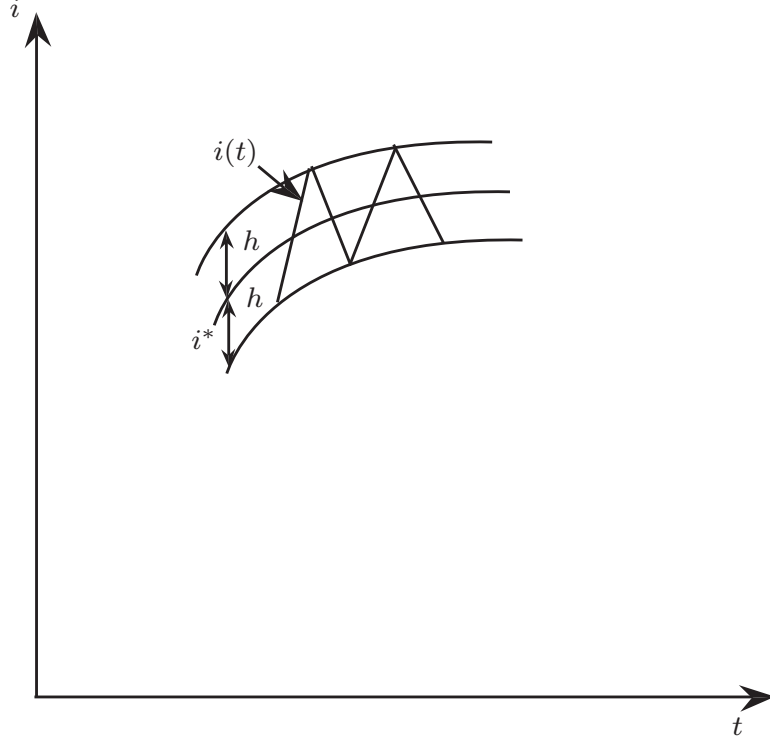


Figure 2.4: Hysteresis current control

hysteresis current control results in reduced-order system dynamics in steady-state, the varying switching frequency creates difficulty in constructing average-value models that are appropriate for transient simulations. Average-value models are beneficial for control design [131, 132] and for the simulation of larger scale systems [133–135]. Accurate dynamic average-value models are important for stability analysis and converter optimization over wide operating conditions [131]. In simulation-based optimization [132] as well as the modeling and simulation of multi-converter systems [136] and power-electronics-based systems [137, 138], average-value models of converters that are both accurate and numerically efficient are necessary. The changing switching frequency and unspecified duty cycle make conventional average-value models of power converters based on PWM control difficult to apply directly to modeling converters that are controlled by hysteresis current control. It has been argued in [139] that hysteresis current control has been understudied in the literature because of this

modeling difficulty.

In [140], hysteresis current control in dc-dc converters is modeled using a small-signal method. Low frequency current injected-absorbed method is used for average-value model. This model is valid for up to one half of the switching frequency. It is mentioned in [141] that small-signal model cannot predict system stability during large signal disturbance or large parameter variation. Thus, a large-signal modeling approach is presented. This large-signal model is based on the assumption that the inductor current is equal to the commanded current, i.e. perfect hysteresis current control model. It is argued in [142] that while the small-signal model [140] predicts the frequency-domain response correctly, it cannot model the time-domain response. While the large-signal model [141] shows time-domain response, it lacks the fast simulation advantage from average-value models. In this paper, a continuous representation of the hysteresis control action is proposed. It is valid if the switching surface is close to a sliding surface. Existing methods for average-value modeling of dc-dc converters include [75, 132, 139, 141, 143]. Among those methods, [132, 139, 143] model hysteresis current control as if it is PWM controlled and formulate a duty cycle that is a function of the current errors between the commanded current and the actual current. Perfect hysteresis current control is assumed in [75, 141]; that is the actual current will always equal to the commanded current. A steady-state current error needs to exist in order to form the duty cycle in [132, 143]. The commanded current derivative is needed in [139, 141]. All those methods will either introduce modeling limitations or errors in steady-state or transient events. Those five methods are compared in detail in Chapter 3.

The primary existing method of average-value modeling of hysteresis current controlled three-phase inverters and motor drives is to assume perfect hysteresis current control. If perfect hysteresis current control is obtained, the system exhibits reduced-order dynamics and high-bandwidth control. However, this method does not account

for transient current changes or the effects of overmodulation on achievable currents. Operating in the overmodulation region will result in an increased fundamental voltage and better dc voltage utilization. This is advantageous in motor drives because it can increase the output voltage without increasing the input dc voltage and reduce losses [144, 145]. An accurate average-value reduced order model of a hysteresis current controlled brushless dc drive is proposed in [146], in which five distinct operating modes are identified. Mathematically models are set forth for each operating modes. Among the five modes, mode 1 is the low speed mode, which can be referred to as the normal linear operating region. While mode 2 through mode 5 are used to model the overmodulation region. In this paper, the average-value model is in the *abc* stationary reference frame and the mathematical equations are quite complicated. Chapter 4 and Chapter 5 reviews the existing perfect hysteresis current control model and propose two new average-value modeling of hysteresis current control in three-phase inverter and motor drives, respectively.

Chapter 3 Average-Value Modeling of Hysteresis Current Control in Boost Converter

In this chapter, a new method for average-value modeling and simulation of boost converters subject to hysteresis current control is proposed. It incorporates a slew-rate limitation on the inductor current that occurs naturally in the circuit during large system transients. This new method is compared with five existing methods in terms of simulation accuracy and run time. The performance is evaluated based on a variety of scenarios, and the simulation results are compared with the results of a detailed model. The simulation results show that the proposed method represents the detailed model well and is faster and more accurate than existing methods. Hardware validation is also presented. The slew-rate-limitation model of boost converters subject to hysteresis current control accurately captures the salient details of converter performance while retaining the computational efficiency of average-value models. This model can be used for time-domain simulation studies where both numerical efficiency and accuracy are required.

Many control techniques have been developed for dc-dc converters such as PWM, peak current mode control, and hysteresis current control. Each of these techniques has relative advantages and disadvantages, but boost converters subject to hysteresis current control are considered herein. Hysteresis current control can ensure stability and fast dynamic response under parameter, line, and load variation and offers greater control bandwidth. These advantages derive from the fact that hysteresis current control approximates ideal sliding mode control [99]; a converter operating under hysteresis current control exhibits reduced-order system dynamics when the current lies within the hysteresis band. Simple hardware implementations are possible using analog comparators, and hysteresis current control can provide automatic protection against overcurrent conditions in certain topologies. For these reasons, hysteresis

current control has been widely used in dc-dc converters.

However, hysteresis current control has some disadvantages as well. In its most basic form, hysteresis current control results in an uncertain and varying switching frequency. This can complicate filter design as the switching harmonics may have varying frequencies associated with them. This difficulty can be largely alleviated by adaptive techniques that stabilize the switching frequency [118]. Another disadvantage is difficulty with digital implementation. With a discrete-time process executing with a fixed period, switching frequency jitter can be introduced, but this effect can also be mitigated by more sophisticated digital implementations [130]. These implementations involve improving the timing resolution of the switching events such that switching events can occur between current samples.

Another disadvantage of hysteresis current control is modeling difficulty. While hysteresis current control results in reduced-order system dynamics when the current lies within the hysteresis band, the varying switching frequency creates difficulty in constructing average-value models that are appropriate for transient simulations. Changing switching frequency and unspecified switch duty cycle make conventional average-value models of dc-dc converters based on PWM control difficult to apply directly to modeling converters that are controlled by hysteresis current control. It is stated in [139] that hysteresis current control has been understudied in the research literature because of this modeling difficulty. In [140], hysteresis current control in dc-dc converters is modeled using a small-signal method. In [141], a large-signal modeling approach is presented. It is argued in [142] that there are tradeoffs between small- and large-signal modeling approaches. Accurate transient dynamic average-value models are important for stability analysis and converter optimization over a wide range of operating conditions [131]. In simulation-based optimization (e.g. multi-objective optimization) [132, 147, 148] as well as the modeling and simulation of multi-converter systems and power-electronics-based systems (e.g. electric ground vehicles,

ships, and aircraft) [136–138], where the converter constitutes a small fraction of the entire system and long time-domain simulations must be performed, average-value simulation models of converters that are both accurate and numerically efficient are necessary. Existing methods for average-value modeling and simulation of dc-dc converters subject to hysteresis current control include [75, 132, 139, 141, 143], and these five methods are described below.

Herein, a novel average-value simulation model of boost converters subject to hysteresis current control using slew-rate limitation is proposed. This model is intended to be used for accurate yet computationally efficient time-domain simulation. It is shown to be both accurate and computationally efficient with respect to existing models and is validated experimentally. The remainder of this chapter is organized as follows. In Section 2, existing methods for average-value modeling of hysteresis current control are summarized, and their advantages and disadvantages are discussed. The slew-rate-limitation-based model is proposed in Section 3. In Section 4, the existing methods and the proposed method are compared in the context of time-domain simulation in order to assess their accuracy and numerical efficiency. Experimental validation of the proposed simulation method is described in Section 5. Conclusions are drawn in Section 6.

3.1 Previous Approaches

A common approach to average-value modeling of hysteresis current control is to model the circuit as if it is PWM controlled and then formulate an effective duty cycle [132, 139, 143]. Once the duty cycle is obtained, a conventional average-value model of the dc-dc converter based on PWM control can be adopted. This approach involves mapping a current error (i.e., a difference between the commanded current of the hysteresis modulator and the actual current) to an effective duty cycle. A boost converter is shown in Figure 3.1. An average-value model of this converter can be

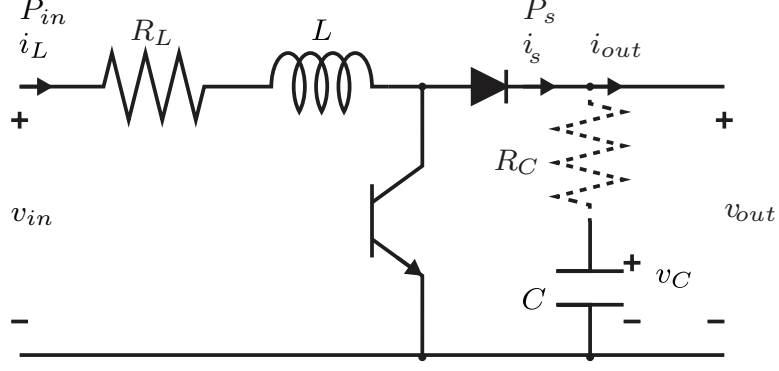


Figure 3.1: Boost converter

expressed as

$$L \frac{di_L}{dt} = v_{in} - R_L i_L - (1 - d) v_C \quad (3.1)$$

$$C \frac{dv_C}{dt} = (1 - d) i_L - i_{out}, \quad (3.2)$$

where d is the effective duty cycle of the switch and the other symbols are defined in Figure 3.1. The dependence of the circuit parameters on switching frequency is neglected for each of the simulation models considered herein.

Method I

One way to approximate the duty cycle for hysteresis control can be found in [132]. With this method, the effective duty cycle is expressed as

$$d = \text{bound} \left(\frac{i_L^* - i_L}{2h} + \frac{1}{2}, 0, 1 \right), \quad (3.3)$$

where i_L^* is the commanded inductor current, h is the hysteresis band used to control the current, and the bound operator is defined as

$$\text{bound}(x, a, b) = \begin{cases} a & x < a \\ x & a \leq x \leq b \\ b & x > b. \end{cases} \quad (3.4)$$

Under this technique, the duty cycle will be unity if the (average-value) current error exceeds the hysteresis band, will be zero if the negative of the current error exceeds

the hysteresis band, and will vary linearly between these conditions. Such a technique requires a steady-state current error to exist in order to achieve a given steady-state duty cycle (with the exception of a steady-state duty cycle of 0.5). The magnitude of the steady-state current error is proportional to the hysteresis current band h . This creates steady-state errors in the time-domain simulations of the converter.

Method II

A related method, found in [143], represents the effective duty cycle as

$$d = \text{bound}(k_h(i_L^* - i_L), 0, 1), \quad (3.5)$$

where k_h is a parameter of the simulation model. In the same manner as Method I, a steady-state current error must exist to achieve a given steady-state duty cycle. For this method, the steady-state current error can be reduced by selecting larger values of k_h , but larger values of k_h will tend to increase simulation run time.

Method III

A third method, described in [139], first estimates the increasing and decreasing time derivatives of the instantaneous inductor current m_i and m_d , respectively:

$$m_i = \frac{v_{in} - R_L i_L}{L} \quad (3.6)$$

$$m_d = \frac{v_{in} - R_L i_L - v_C}{L}. \quad (3.7)$$

Then, the amount of time for each device to be on is calculated by dividing the change in instantaneous inductor current by the time derivative of the instantaneous inductor current. The time for the instantaneous current to increase from $i_L - h$ to $i_L^* + h + \Delta i_L^*$ is

$$t_{ld} = \frac{i_L^* - i_L + 2h}{m_i - \frac{di_L^*}{dt}}, \quad (3.8)$$

where $\Delta i_L^* = \frac{di_L^*}{dt} t_{ld}$ is the change in the commanded inductor current during the time the lower device is on. The time for the instantaneous current to decrease from $i_L + h$ to $i_L^* - h + \Delta i_L^*$ is

$$t_{ud} = \frac{i_L^* - i_L - 2h}{m_d - \frac{di_L^*}{dt}}, \quad (3.9)$$

where $\Delta i_L^* = \frac{di_L^*}{dt} t_{ud}$ is the change in the commanded inductor current during the time the upper device is on. The effective duty cycle d can be approximated as

$$d = \text{bound} \left(\frac{t_{ld}}{t_{ld} + t_{ud}}, 0, 1 \right). \quad (3.10)$$

This method requires knowledge of the time derivative of the commanded inductor current. In some cases, this derivative may be available in the simulation model, but this is not generally true. For example, a step change in commanded inductor current could be requested. In the general case, numerical differentiation of i_L^* is used in the simulation model.

Method IV

Method IV, discussed in [75] in the context of current-regulated motor drive modeling assumes perfect hysteresis control, i.e., the average value of the inductor current i_L is always equal to the commanded current i_L^* . The switch power must equal the input power less resistive losses. The modeling for a boost converter is as follows:

$$i_L = i_L^* \quad (3.11)$$

$$C \frac{dv_C}{dt} = \frac{v_{in} i_L^* - R_L i_L^{*2}}{v_C} - i_{out}. \quad (3.12)$$

By assuming perfect hysteresis current control, a reduction in run time (compared to a model based on (3.1) and (3.2)) is expected because of the elimination of a state variable, but details about the dynamic behavior of the converter are lost, reducing accuracy.

Method V

A similar method in [141] also assumes perfect hysteresis current control, i.e.,

$$i_L = i_L^*. \quad (3.13)$$

The effective duty cycle can be approximated from (3.2) as

$$d = 1 - \frac{C \frac{dv_c}{dt} + i_{out}}{i_L}. \quad (3.14)$$

Substituting (3.13) and (3.14) into (3.1) and solving yields

$$C \frac{dv_C}{dt} = \frac{v_{in} i_L^* - R_L i_L^{*2} - L i_L^* \frac{di_L^*}{dt}}{v_C} - i_{out}. \quad (3.15)$$

This method, like Method III, requires knowledge of the time derivative of the inductor current command.

3.2 Proposed Approach

The proposed technique involves the use of slew-rate limitation to model the inductor current. This approach is motivated by the observation that the average value of the inductor current would ideally follow the commanded current, but it is subject to rate constraints. This method approaches modeling from a different perspective from existing models. Rather than formulate an effective duty cycle, the proposed method treats the time derivative of the inductor current behaviorally. In particular, it is recognized that the inductor current will follow the commanded inductor current (as in Methods IV and V), but that its derivative will be bounded by the voltages present in the circuit. In the circuit depicted in Figure 3.1, the time derivative of the inductor current in the two operating states (i.e. when the diode is conducting and when the diode is blocking), can be expressed as

$$L \frac{di_L}{dt} = v_{in} - R_L i_L - v_C \quad (3.16)$$

$$L \frac{di_L}{dt} = v_{in} - R_L i_L, \quad (3.17)$$

respectively. From the above equations, the time derivative of the inductor current can be approximated such that the inductor current follows the commanded inductor current but is bounded as follows:

$$\frac{di_L}{dt} = \text{bound} \left(\frac{i_L^* - i_L}{\tau_s}, \frac{v_{in} - R_L i_L - v_C}{L}, \frac{v_{in} - R_L i_L}{L} \right), \quad (3.18)$$

where τ_s is a time constant of the model. There is a tradeoff between accuracy and simulation run time associated with the choice of τ_s . Smaller values of τ_s will result in better accuracy but tend to increase run time. The output voltage is modeled by (3.2) in a similar manner to Methods IV and V. However, using the time derivative of the inductor current, it is possible to represent the instantaneous power flowing into the magnetic field of the inductor as

$$P_L = \frac{d}{dt} \frac{1}{2} L i_L^2 = L i_L \frac{di_L}{dt}. \quad (3.19)$$

Thus, the power flowing through the switching pole can be expressed as

$$P_s = v_{in} i_L - R_L i_L^2 - L i_L \frac{di_L}{dt}. \quad (3.20)$$

As the inductor current is a state variable of the proposed model and the time derivative of the inductor current is calculated in (3.18), (3.19) can be used to represent the instantaneous power flowing into the magnetic field of the inductor. Conservation of power and the behavior of the output capacitor yield

$$C \frac{dv_C}{dt} = \frac{v_{in} i_L - R_L i_L^2 - L i_L \frac{di_L}{dt}}{v_C} - i_{out}. \quad (3.21)$$

Unlike Method V, it is not necessary to know the time derivative of the inductor current command to evaluate this expression.

A couple of observations about the proposed method are worthwhile. As the current error saturates, the proposed method acts exactly like the detailed switching circuit, allowing for it to have high accuracy during transient events. Furthermore, the slew-rate-limitation representation is sufficiently smooth to allow the ordinary

differential equation (ODE) solver to solve the system without taking very small time steps. While the parameter τ_s is a time constant associated with the proposed model, the method is not equivalent to sampling the current error at a rate of $1/\tau_s$. In fact, the simulation algorithm is able to use time steps several orders of magnitude larger than τ_s . Also, the proposed model does not have a parameter related to the hysteresis current band h . This may seem counterintuitive, but the hysteresis current band only affects the current ripple and switching frequency; it does not significantly affect the average behavior of the currents.

ESR Incorporation

For some applications (e.g., loss calculation and stability analysis [149–152]), it may be advantageous to consider capacitor equivalent series resistance (ESR) in the proposed model. The incorporation of ESR is challenging because v_{out} is not available as a state variable. Instead, v_C is a state variable, and an algebraic relationship exists among v_{out} , i_s and i_{out} .

The current flowing through the switch current can be expressed as

$$i_s = \text{bound} \left(\frac{\gamma}{v_{out}}, 0, |i_L| \right) \text{sign } i_L, \quad (3.22)$$

where

$$\gamma = \left[v_{in} - R_L i_L - \frac{L}{\tau_s} (i_L^* - i_L) \right] |i_L|. \quad (3.23)$$

This is not a function of either v_{out} or i_{out} . The output current can be expressed as

$$i_{out} = \frac{v_C - v_{out}}{R_C} + i_s. \quad (3.24)$$

Substitute (3.22) into (3.24) yields

$$i_{out} = \frac{v_C - v_{out}}{R_C} + \text{bound} \left(\frac{\gamma}{v_{out}}, 0, |i_L| \right) \text{sign } i_L. \quad (3.25)$$

This expression can be represented graphically as shown in Figure 3.2. In this figure, the relationship between the output voltage and current of the converter is plotted.

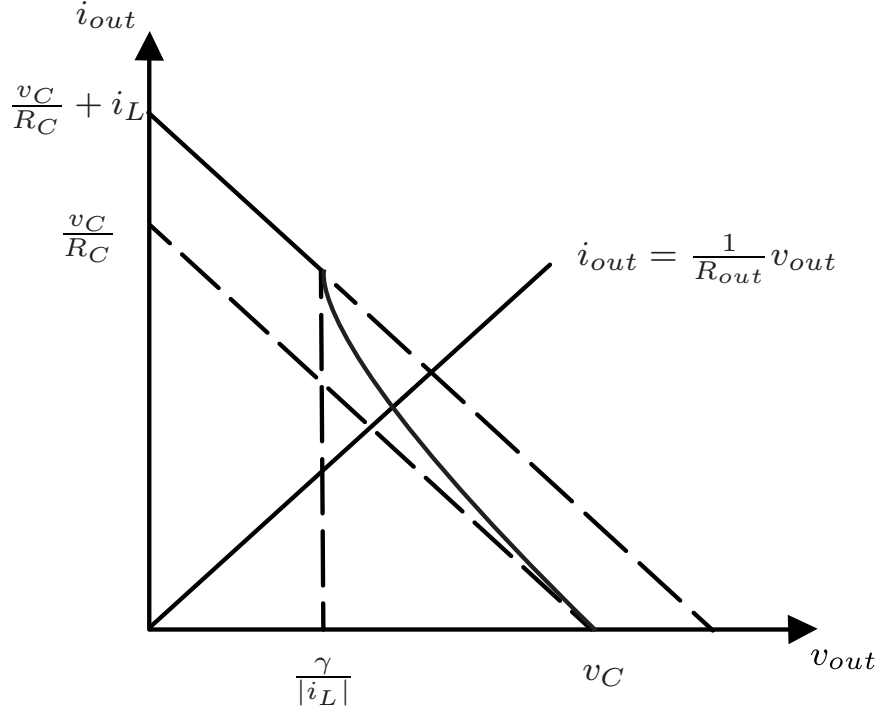


Figure 3.2: Graphically solving output voltage

Load-line analysis can be used to establish the output voltage and current by finding the intersection of this curve with the curve presented by the load. For example, in the case of a resistive load R_{out} , the load line is the straight line shown in Figure 3.2.

The output voltage can be expressed as

$$v_{out} = \alpha \begin{cases} v_C, & \text{if } \gamma < 0 \\ v_C + R_C i_L, & \text{else if } v_C \leq \frac{\gamma}{\alpha |i_L|} - R_C i_L, \\ \frac{v_C + \sqrt{\Delta}}{2}, & \text{otherwise} \end{cases} \quad (3.26)$$

where

$$\alpha = \frac{R_{out}}{R_{out} + R_C} \quad (3.27)$$

and

$$\Delta = v_C^2 + \frac{4R_C \gamma \text{sign } i_L}{\alpha}. \quad (3.28)$$

Table 3.1: Boost Converter Parameters

Parameter	Value
L	1.52 mH
R_L	35.4 m Ω
C	470 μ F
h	2.5 A

3.3 Simulation Comparisons

In order to compare alternative methods of representing boost converters subject to hysteresis current control, a converter with the parameters listed in Table 3.1 is studied. A detailed model of the converter and each of the methods described above are simulated for three cases, each lasting 15 ms and intended to show the dynamic response of the models to different transient conditions. In Case I, the input voltage is 150 V, the load resistance is 6 Ω , and the inductor current command is stepped from 30 A to 45 A at 5 ms. In Case II, the inductor current command is 45 A, the load resistance is 6 Ω , and the input voltage is stepped from 100 V to 150 V at 5 ms. In Case III, the inductor current command is 45 A, the input voltage is 150 V, and the load resistance is stepped from 4 Ω to 6 Ω at 5 ms. For all the cases, the initial inductor current and capacitor voltage for each method are set to their corresponding steady-state values.

Each method is simulated using MATLAB R2012b Simulink's ode23tb integration algorithm with a maximum time step equal to the total simulation time 15 ms, a default relative tolerance of 10^{-3} , and an absolute tolerance calculated in the default manner as the product of the relative tolerance and the maximum absolute value of the state variable over the course of simulation [153]. The maximum time step is ineffective in each case because the length of the simulation is 15 ms; the time step of the ODE solver is controlled by solver tolerances and zero crossing detection only. The methods are compared on the basis of numerical efficiency and accuracy. Two measures are used to quantify numerical efficiency: number of time steps used by

the ODE solver and run time averaged over 100 simulations. The simulations are performed on an Intel Core i7 2.8-GHz processor with 4 GB of memory. Accuracy is measured by comparing the inductor current and capacitor voltage waveforms predicted by each model with the waveforms predicted by the detailed model sampled at 1 ns. The rms error associated with these waveforms is calculated. It is expected that every method would have some error because the detailed model waveforms include switching ripple. For example, when a triangular instantaneous current with peak-to-peak current ripple of $2h$ is represented by its average value, the rms error can be shown to be $h/\sqrt{3}$. For the value of h considered herein, this value is approximately 1.44 A. The simulation results that follow show that the inductor current rms error approaches this number.

Method II and the proposed method have parameters that may be varied to adjust the tradeoff between numerical efficiency and accuracy. In order to understand the effect that these variations have, Case I is simulated as these parameters are varied over wide ranges. In Method II, the parameter k_h is varied over the range 10^{-3} – 10^{12} A⁻¹. In the proposed method, the parameter τ_s is varied over the range 10^{-12} – 10^3 s. For each of these values, the number of time steps and the current error are calculated. The numbers of time steps and the current errors of the other methods are also calculated for this case.

Relative current error is the difference between simulated current rms error and the theoretical minimum current rms error ($h/\sqrt{3}$) which is approximately 1.44 A. The Pareto-optimal front associated with the number of time steps and the relative current error for each method are shown in Figure 3.3. It can be seen from this figure that the proposed method dominates each method except for Method IV, which is a reduced-order method. This means that for any desired level of accuracy, the proposed method can be simulated using fewer time steps than the other methods (except Method IV). Likewise, for a given allowable number of time steps, the pro-

posed method can produce a more accurate result than the other methods (except Method IV). Method IV, not being dominated by the proposed method, may be appropriate for use in simulations in which reduced accuracy may be accepted in exchange for reduced run time, but it is seen in the time-domain studies that follow that it has obvious difficulties predicting the dynamic behavior of the converter in response to changes in the inductor current command. The proposed method produces the points in Figure 3.3 with both the smallest current error and the fewest number of time steps, and the proposed method provides great flexibility to adjust the tradeoff between accuracy and numerical efficiency by varying τ_s to meet the needs of the simulation. In order to perform more detailed comparisons of the methods, points in the “knee” of each Pareto-optimal front are identified and used for subsequent studies. For Method II, k_h is selected to be 3.55 A^{-1} . For the proposed method, τ_s is selected to be $3.16 \text{ }\mu\text{s}$.

Figure 3.4 shows the inductor current and Figure 3.5 shows the capacitor voltage results of the detailed model and the average-value models for Case I, a step increase in commanded inductor current. It can be seen that Method I exhibits a great deal of steady-state error in both variables. Method III does not model the inductor current transient accurately. Also, Method IV and Method V do not follow the finite rise time associated with the inductor current because they assume perfect current control. Consequently, Method IV does not predict the initial decrease in capacitor voltage following the step increase in current command. Method V shows a slight initial decrease in capacitor voltage; the use of a differentiator in Method V can be problematic for the ODE solver because it does not use the differentiator to control the solution error. If a smaller time step were explicitly used, Method V may be expected to more accurately predict the voltage dip [141]. The numbers of time steps, run times, and current and voltage errors are shown in Table 3.2. It can be seen that the proposed method uses fewer timesteps and requires less run time than

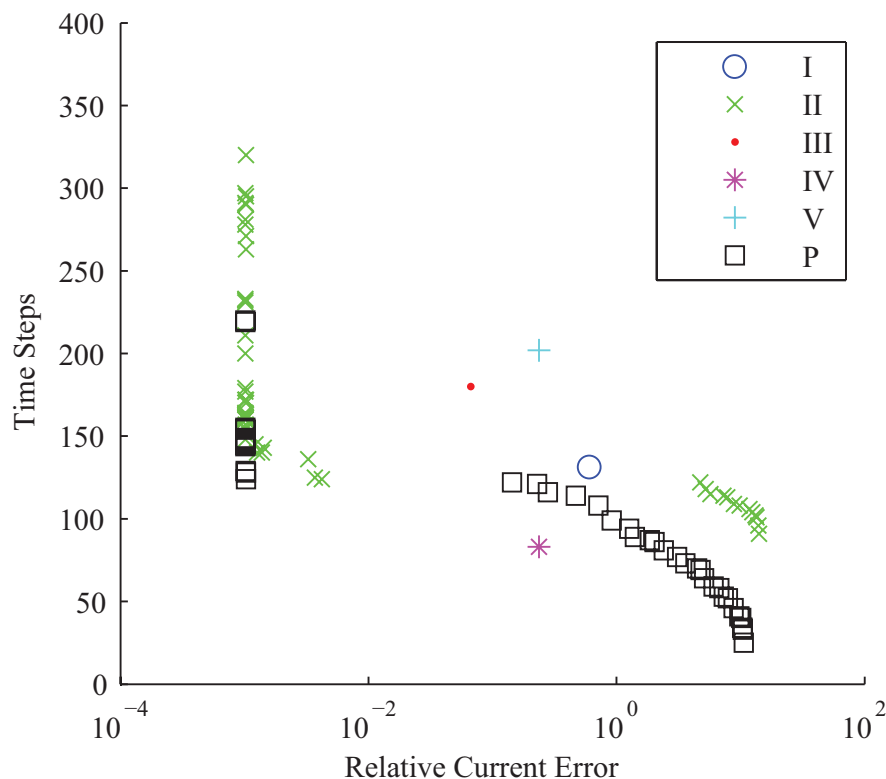


Figure 3.3: Relationship between current error and number of time steps for each method for Case I. I-V signify Methods I-V. P signifies the proposed method.

each of the existing methods except for the reduced-order Method IV. The proposed method has smaller current and voltage error than each of the existing methods. Compared with Method IV, which executed faster than the proposed method, the proposed method had 14% less current error and 59% less voltage error. Compared with Method II, which is the next most accurate method for this case, the proposed method had 0.16% less current error and 2.2% less voltage error while requiring 8.8% fewer time steps and 18% less run time. These results are expected from Figure 3.3.

Figure 3.6 shows the the inductor current and Figure 3.7 shows the capacitor voltage simulation results of the detailed model and the average-value models for Case II, a step increase in input voltage. Again, Method I exhibits a great deal of steady-state error in both variables and reacts to the step change in input voltage, a reaction that the detailed model does not predict. It can also be seen that Method II

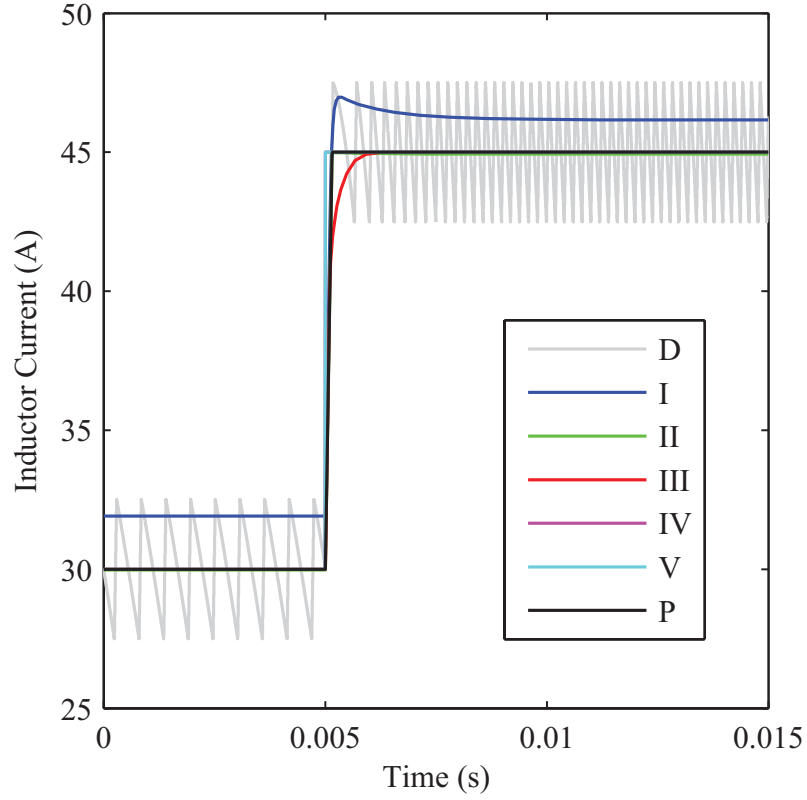


Figure 3.4: Inductor current for Case I (i_L^* step). D signifies the detailed model. I–V signify Methods I–V. P signifies the proposed method.

Table 3.2: Efficiency and Accuracy Comparison for Each Method for Case I (i_L^* step)

Method	Time Steps	Run Time (ms)	Current Error (A)	Voltage Error (V)
I	131	21.2	2.05	3.87
II	136	23.7	1.45	1.10
III	180	28.1	1.51	1.22
IV	83	18.1	1.68	2.62
V	202	21.1	1.68	2.13
Proposed	124	19.5	1.44	1.07

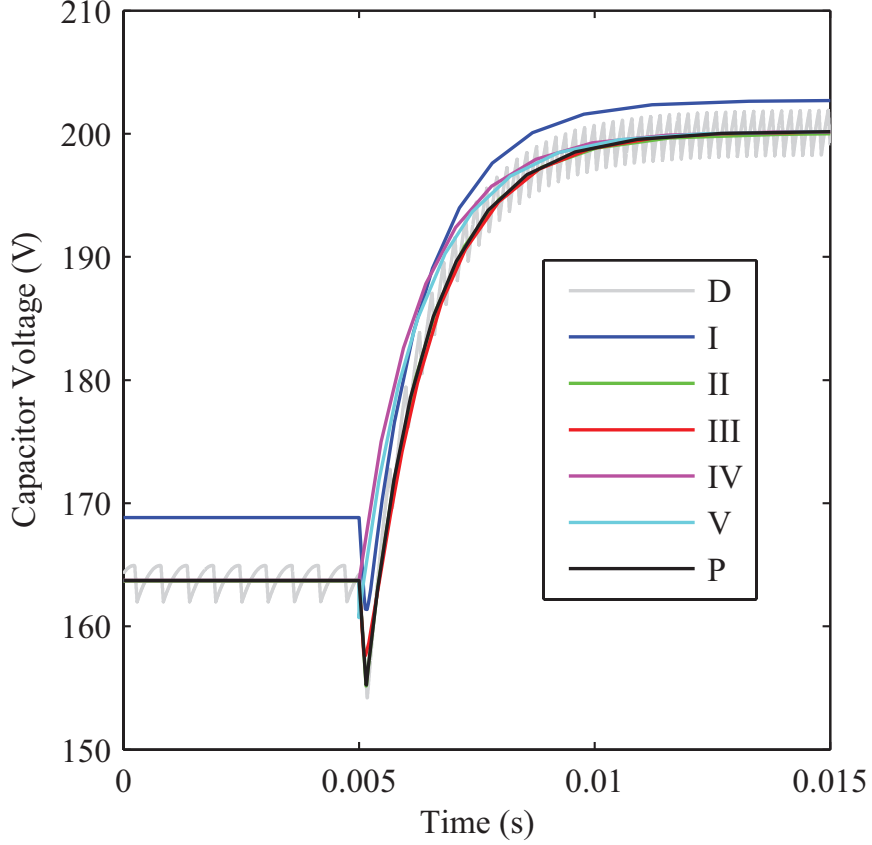


Figure 3.5: Capacitor voltage for Case I (i_L^* step). D signifies the detailed model. I–V signify Methods I–V. P signifies the proposed method.

does not model the inductor current very well; it exhibits noticeable steady-state error and also reacts to the step change in input voltage. The numbers of time steps, run times, and current and voltage errors are shown in Table 3.3. It is noted that the ODE solver solves Methods III–V and the proposed method nearly identically. Each of these methods requires nearly identical numbers of time steps and has the same current and voltage error. However, the proposed method required 36% less run time than Method III and 6.3% less run time than Methods IV and V. Compared with Method II, which exhibits visually obvious current error, the proposed method has 0.28% less current error and 1.8% less voltage error while requiring 30% fewer time steps and 15% less run time.

Figure 3.8 shows the inductor current and Figure 3.9 shows the capacitor voltage

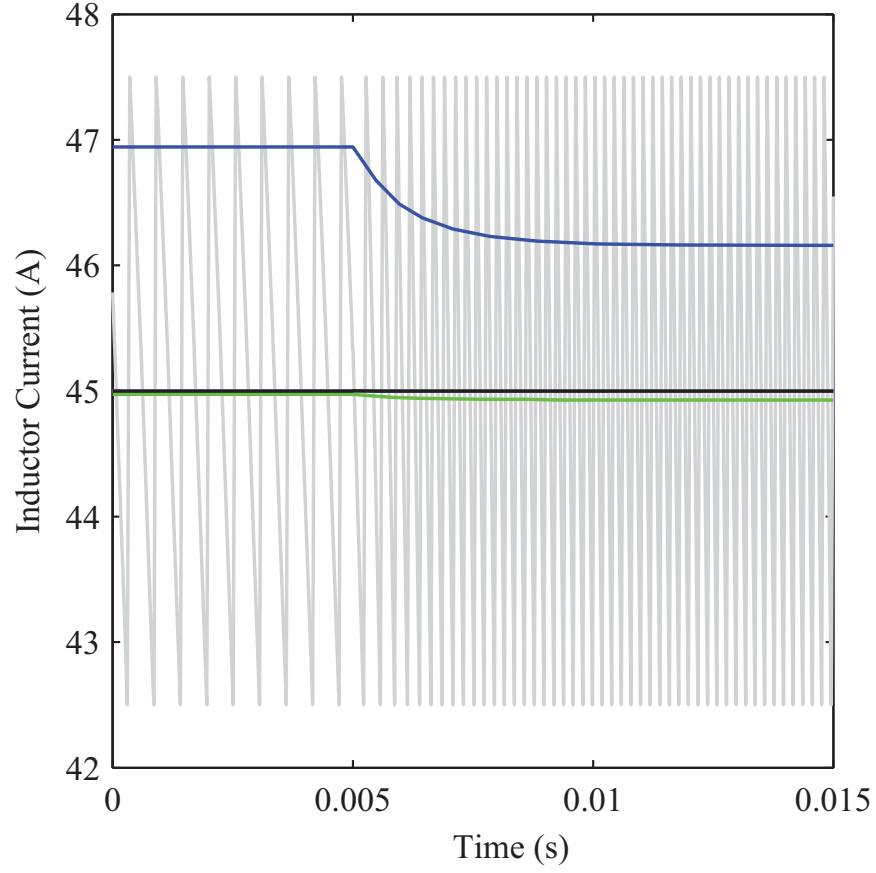


Figure 3.6: Inductor current for Case II (v_{in} step). D signifies the detailed model. I–V signify Methods I–V. P signifies the proposed method.

Table 3.3: Efficiency and Accuracy Comparison for Each Method for Case II (v_{in} step)

Method	Time Steps	Run Time (ms)	Current Error (A)	Voltage Error (V)
I	108	21.2	1.77	2.34
II	119	22.2	1.45	1.19
III	84	29.3	1.45	1.17
IV	82	20.0	1.45	1.17
V	82	20.0	1.45	1.17
Proposed	83	18.7	1.45	1.17

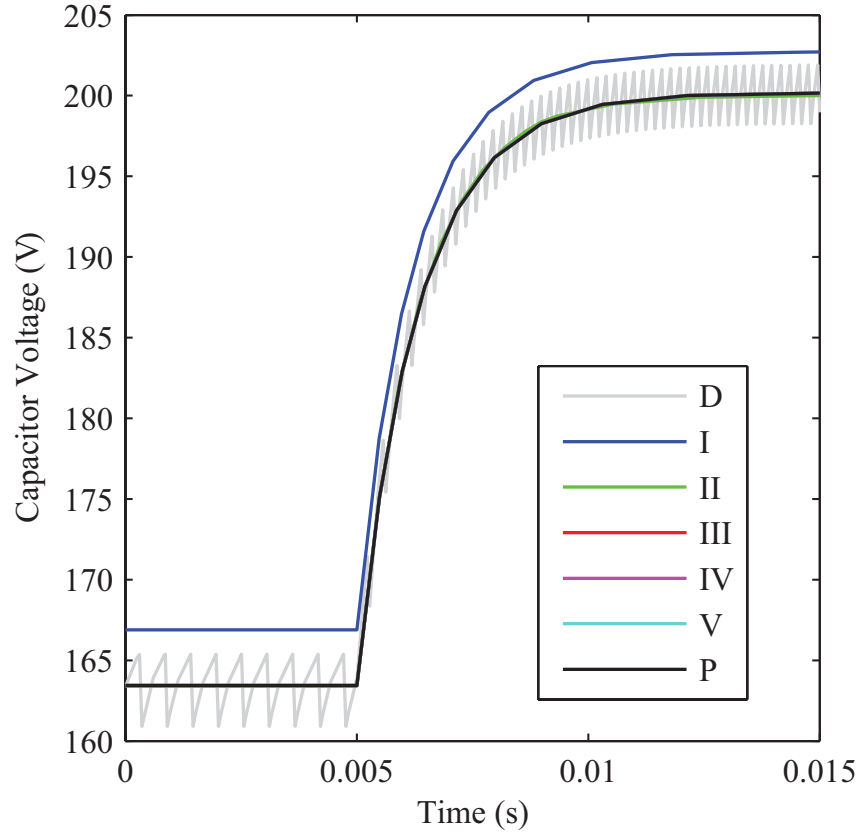


Figure 3.7: Capacitor voltage for Case II (v_{in} step). D signifies the detailed model. I–V signify Methods I–V. P signifies the proposed method.

simulation results of the detailed model and the methods for Case III, a step increase in load resistance. Once again, Method I exhibits a great deal of steady-state error in both variables and reacts to the step change in load resistance, a reaction that the detailed model does not predict. Method II does not model the inductor current very well after the step resistance change; it exhibits noticeable steady-state error and also reacts to the step change in load resistance. The numbers of time steps, run times, and current and voltage errors are shown in Table 3.4. As with Case II, the ODE solver solves Methods III–V and the proposed method nearly identical, with essentially equal numbers of time steps and equal current and voltage errors. Methods IV and V, the two reduced-order methods, required slightly less run time than the proposed method, 1.6% and 5.6%, respectively. The proposed method required 31% less run

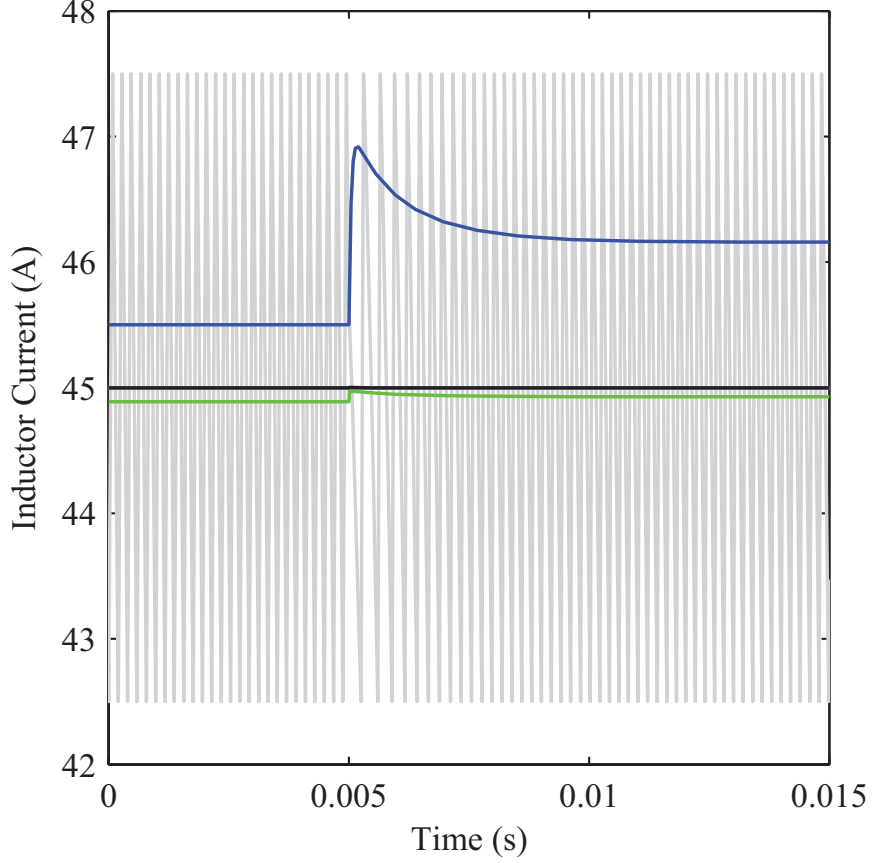


Figure 3.8: Inductor current for Case III (R step). D signifies the detailed model. I–V signify Methods I–V. P signifies the proposed method.

Table 3.4: Efficiency and Accuracy Comparison for Each Method for Case III (R step)

Method	Time Steps	Run Time (ms)	Current Error (A)	Voltage Error (V)
I	93	22.3	2.06	3.23
II	97	21.8	1.46	1.18
III	87	28.2	1.45	1.18
IV	86	19.2	1.45	1.18
V	86	18.4	1.45	1.18
Proposed	86	19.5	1.45	1.18

time than Method III. The proposed method has 0.18% less current error 0.39% less voltage error while requiring 11% fewer time steps and less run time than Method II, which exhibits visually obvious current error.

From these simulation results, it can be seen that the proposed slew-rate-limitation-

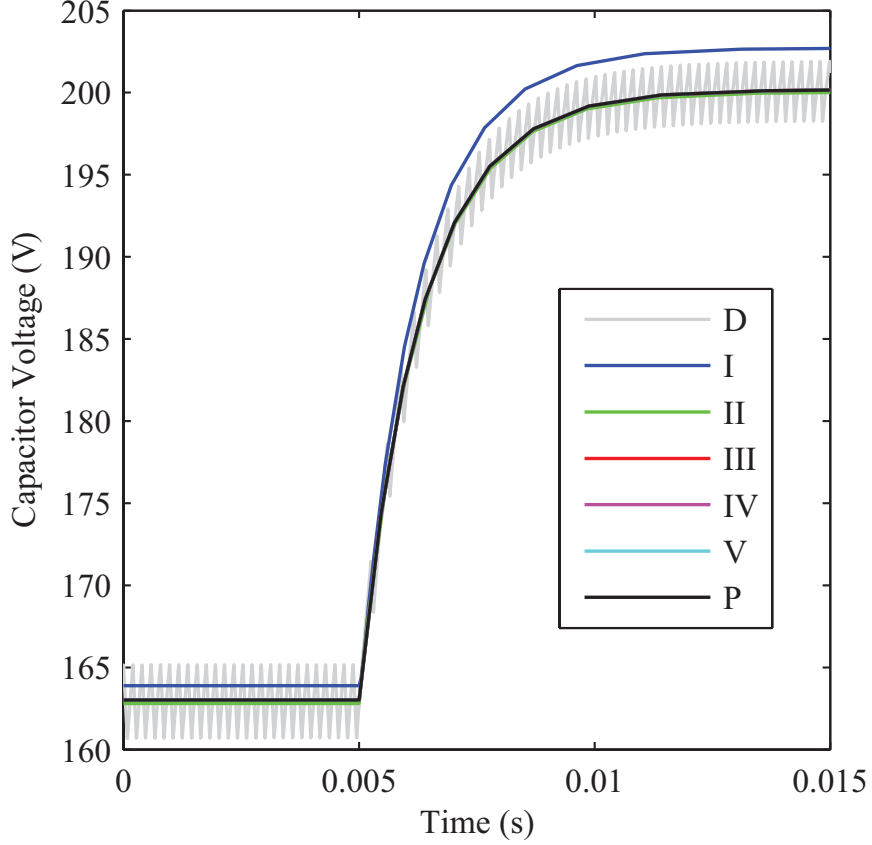


Figure 3.9: Capacitor voltage for Case III (R step). D signifies the detailed model. I–V signify Methods I–V. P signifies the proposed method.

based average-value model of the boost converter under hysteresis current control is best able to predict the performance of the converter over a wide range of transient conditions (as exemplified by the three cases studied above). Method I generally has much lower accuracy than the other methods. Method II is the only method with accuracy comparable to the proposed method for the inductor current command step, but at a higher computational cost. Method II also performs worse for other types of transients than the other methods. Methods III–V provide comparable accuracy for the input voltage and load resistance steps, but they are much less accurate for the inductor current command step. There may be applications in which the reduced-order Method IV may be appropriate because it generally requires less run time, but this method does not attempt to represent the current dynamics during transient

events, resulting in poor accuracy during such events. The proposed method offers great flexibility to adjust the tradeoff between accuracy and numerical efficiency by varying τ_s to meet the needs of the simulation, and the simulation results suggest that it offers the best combination of accuracy and numerical efficiency for transient simulation.

3.4 Frequency-Domain Comparison

The primary application of the proposed method is for accurate and numerically efficient time-domain simulation. However, it is important that the method has appropriate frequency-domain characteristics. In this section, the ability of the proposed model to predict the frequency-domain characteristics of the boost converter is examined and compared with existing average-value models. In particular, the open-loop control-to-output transfer function $\frac{v_C}{i_L^*}$ is studied to further demonstrate the properties of the proposed method. Inductor current command perturbations at frequencies ranging from 1 Hz to 1 kHz are injected into these models and the resulting effect on the capacitor voltage is recorded [154]. The initial conditions are the same as in Case I, and the perturbation magnitude is 0.4 A. This procedure is performed for the detailed model, the existing models, and the proposed model. The resulting magnitude and phase response are shown in Figure 3.10. It can be seen that Method I has a dc gain error of approximately 0.7 dB. The other methods have approximately equal dc gains and are consistent with the detailed model. Method IV exhibits significant phase error beginning at about 20 Hz, Method I exhibits significant phase error beginning at about 200 Hz, and the other methods approximate the behavior of the detailed model well through 1 kHz. This shows that the proposed model is capable of predicting the frequency-domain characteristics of the converter, making it suitable for use in control design and small-signal stability analysis.

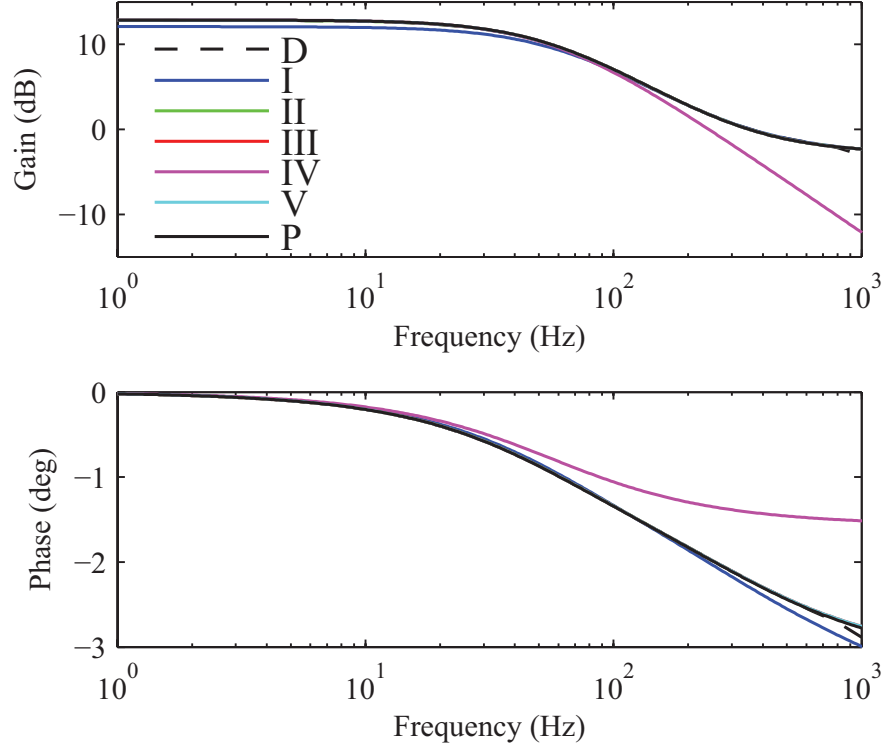


Figure 3.10: Transfer function analysis. I–V signify Methods I–V. P signifies the proposed method.

3.5 Experimental Validation

To validate the proposed slew-rate-limitation-based method of modeling hysteresis current control experimentally, a prototype boost converter shown in Figure 3.1 with parameters shown in Table 3.1 is studied in two experiments. In Experiment I, the inductor current commanded is initially equal to 45 A and is stepped to 30 A at approximately 10 ms. In Experiment II, the load resistance is initially approximately equal to $6.5 \, \Omega$ and is stepped to approximately $6 \, \Omega$ at approximately 2 ms. A TI F28335 150 MHz microcontroller is used. The hysteresis control is implemented by sampling the inductor current at 1 MHz and switching if the current falls outside the hysteresis bands. The current and voltage are measured using a sampling rate of 1 Msample/s, and the measured values have been low-pass filtered with a time

Table 3.5: Efficiency and Accuracy Comparison for Each Method for Experiment I (i_L^* step)

Method	Time Steps	Run Time (ms)	Current Error (A)	Voltage Error (V)
I	148	22.8	2.91	4.68
II	141	22.6	2.06	1.59
III	127	31.4	2.07	1.60
IV	70	21.8	2.26	2.82
V	196	22.8	2.26	2.64
Proposed	135	22.0	2.05	1.59

Table 3.6: Efficiency and Accuracy Comparison for Each Method for Experiment II (R step)

Method	Time Steps	Run Time (ms)	Current Error (A)	Voltage Error (V)
I	56	21.8	2.29	2.73
II	53	23.2	2.00	1.30
III	56	29.0	1.99	1.27
IV	55	21.2	1.99	1.27
V	55	22.3	1.99	1.27
Proposed	56	21.1	1.99	1.27

constant of 2 μ s to remove measurement noise while retaining switching ripple. The results of simulating these two situations compared with all the average-value models using the parameters described above are also shown in Figure 3.11, Figure 3.12, and Figure 3.13, Figure 3.14, respectively. The corresponding numbers of time steps, run times, and current and voltage errors are shown in Tables 3.5 and 3.6, respectively. It can be seen that the proposed method accurately predicts the average behavior of the measured waveforms. The relationships among the numbers of time steps and run times required by the methods are generally similar to those described above for the simulation results. The current and voltage error disparities are less pronounced in the experimental results because of the general difficulty of matching the experimental results associated with unmodeled parasitics, parameter errors, etc. Generally, the experimental studies show that the proposed method is capable of accurately predicting the experimental waveforms while retaining good numerical efficiency.

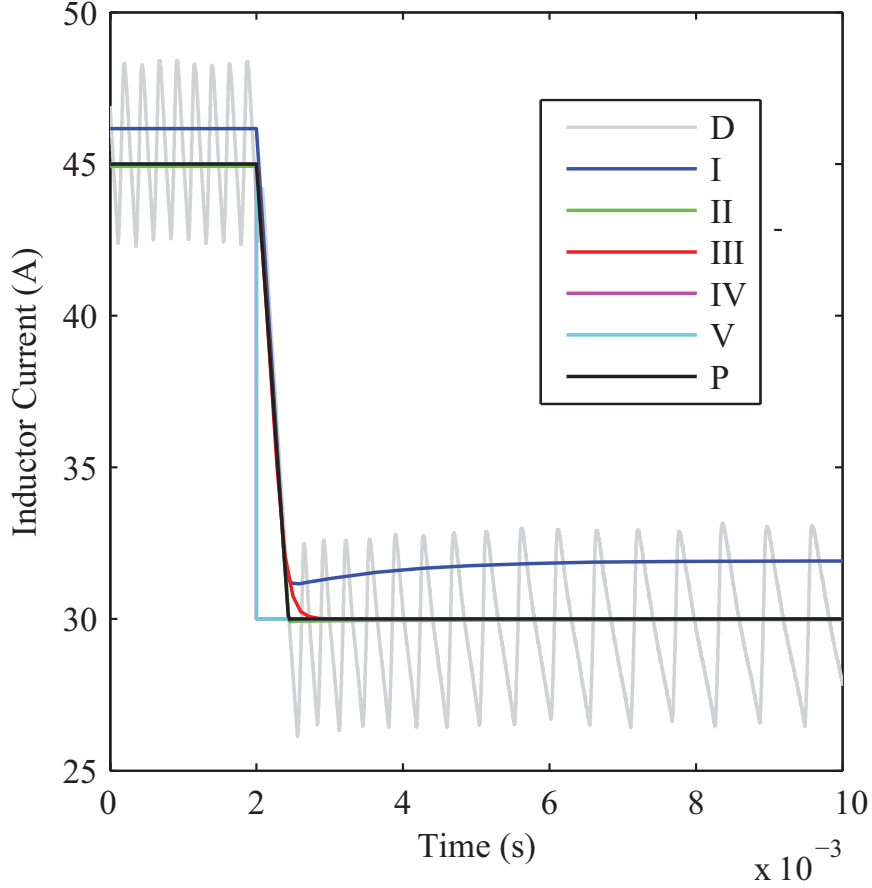


Figure 3.11: Experimentally measured and simulated inductor current for Experiment I (i_L^* step). D signifies the experimentally measure waveforms. I–V signify Methods I–V. P signifies the proposed method. The waveforms have been low-pass filtered with a time constant of 2 μ s to remove measurement noise.

3.6 Conclusion

Existing techniques for average-value modeling of boost converters subject to hysteresis current control are reviewed, and a new technique based on slew-rate limitation is proposed. The proposed model is compared with existing models in time-domain simulations of the converter in a variety of transient cases. This new simulation model is also validated with experimental measurements from a prototype boost converter. Overall, the proposed simulation method is found to be better in terms of both numerical efficiency and accuracy than existing average-value simulation methods. This new model of hysteresis current control can improve simulation applications such as

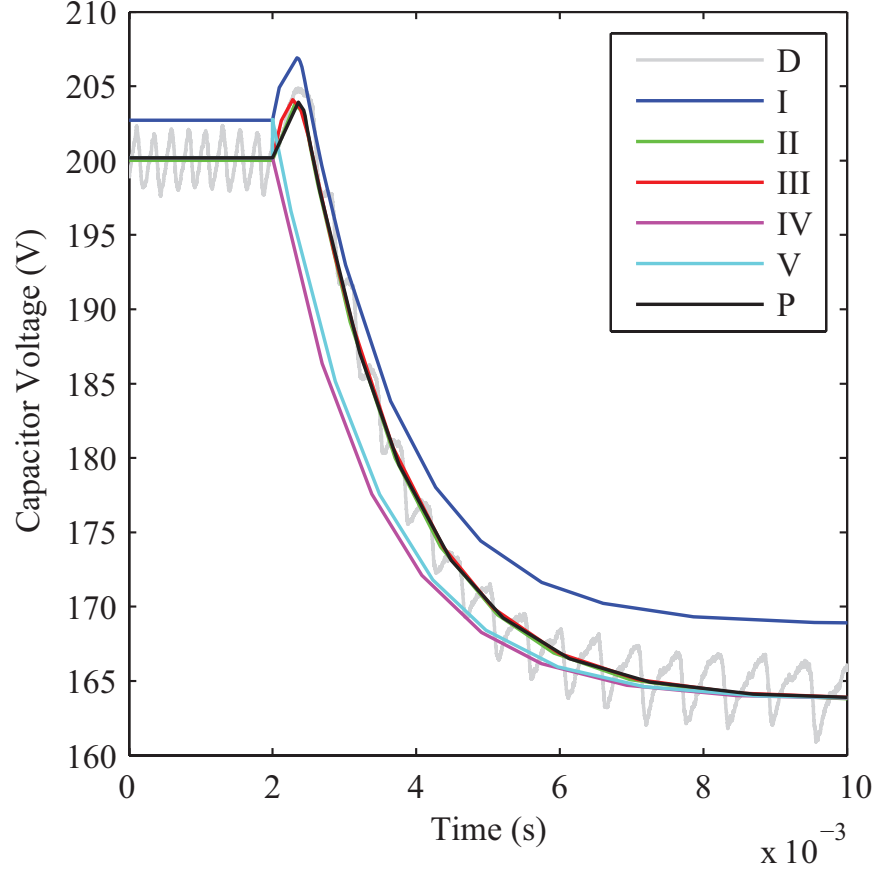


Figure 3.12: Experimentally measured and simulated capacitor voltage for Experiment I (i_L^* step). D signifies the experimentally measure waveforms. I–V signify Methods I–V. P signifies the proposed method. The waveforms have been low-pass filtered with a time constant of 2 μ s to remove measurement noise.

large multi-converter systems, dc power systems, and simulation-based design that require accurate and numerically efficient simulation. The proposed method can also potentially be extended to other converter topologies in which hysteresis current control is employed [155, 156].

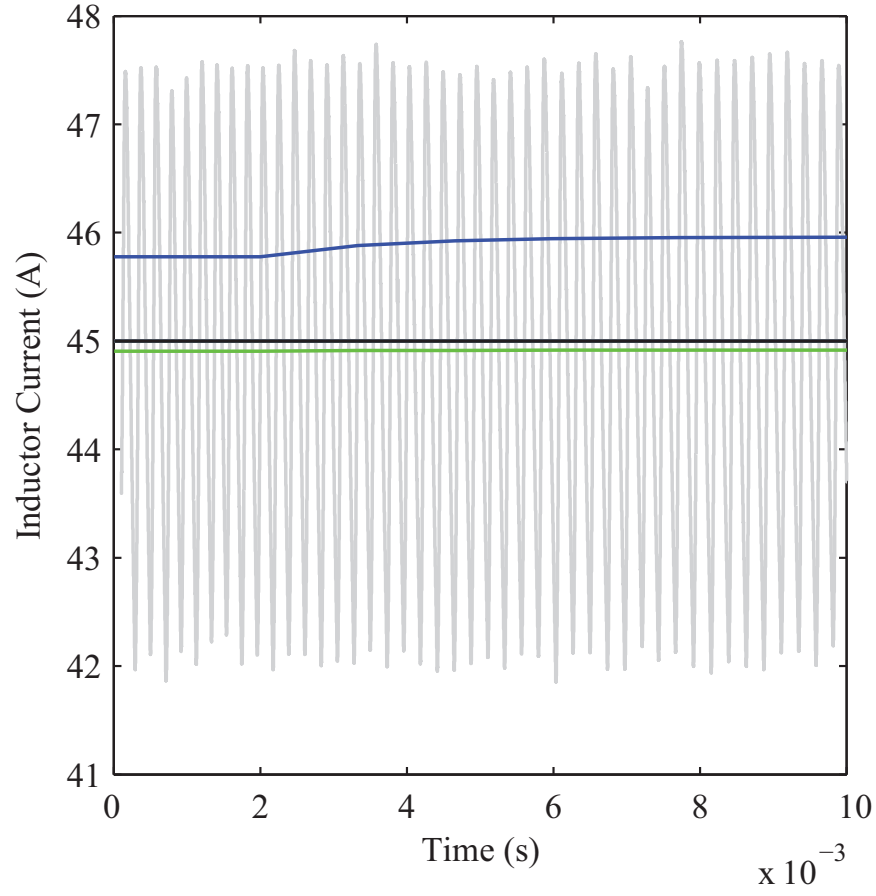


Figure 3.13: Experimentally measured and simulated inductor current for Experiment II (R step). D signifies the experimentally measure waveforms. I–V signify Methods I–V. P signifies the proposed method. The waveforms have been low-pass filtered with a time constant of $2 \mu\text{s}$ to remove measurement noise.

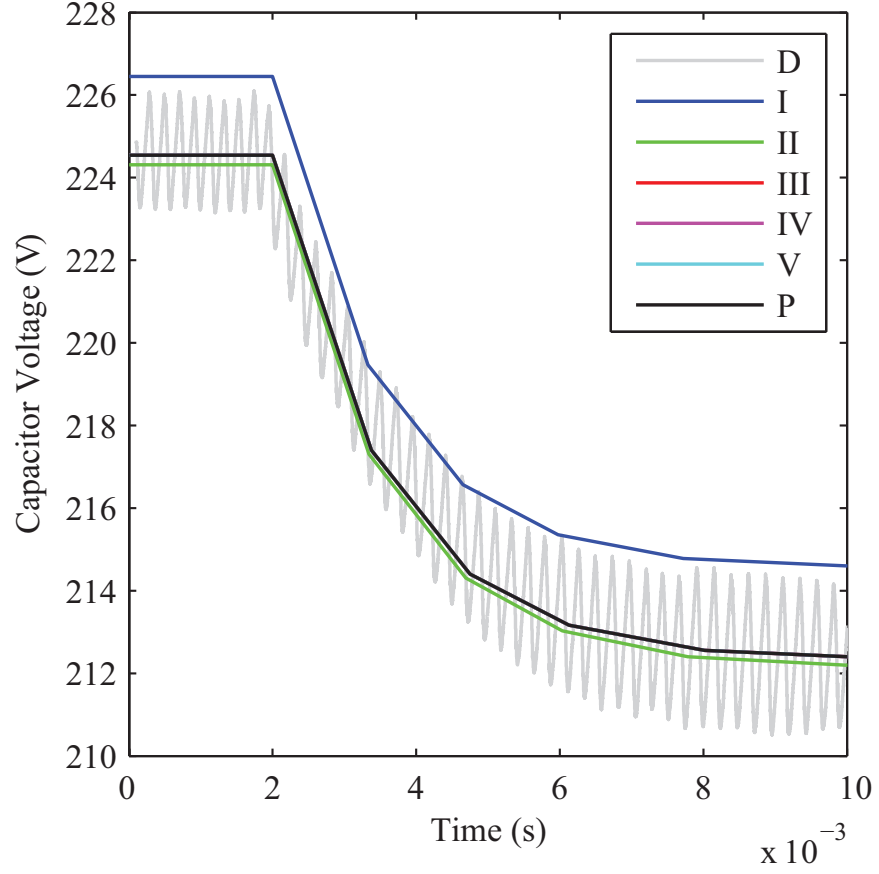


Figure 3.14: Experimentally measured and simulated capacitor voltage for Experiment II (R step). D signifies the experimentally measure waveforms. I–V signify Methods I–V. P signifies the proposed method. The waveforms have been low-pass filtered with a time constant of $2 \mu\text{s}$ to remove measurement noise.

Chapter 4 Average-Value Modeling of Hysteresis Current Control in Three-Phase Inverters

The primary existing methods for average-value modeling of hysteresis current controlled three-phase inverters do not accurately portray transient or overmodulation operation. This chapter presents the effective modulation index and uses it to propose two new methods for average-value modeling of hysteresis current controlled three-phase inverters: the effective voltage model and the slew-rate limitation model. These models are compared both in simulation and experimentally with the existing perfect hysteresis current control model in a variety of cases. It is shown that the proposed models are better able to predict the transient and overmodulation performance of the inverter than the existing method while retaining the computational efficiency advantages of average-value models.

Hysteresis current controlled three-phase inverters are widely used in active power filter [157–159], ac motor drive [105, 160, 161], uninterruptible power supply [162], and grid-connected renewable energy [163, 164] applications. It has advantages such as robust control, fast dynamic response, and overcurrent protection [98, 165]. However, hysteresis current control has the disadvantage of varying switching frequency. This variation can complicate filter design, but it can be addressed by adjusting the hysteresis band to stabilize the switching frequency [128, 166, 167]. The varying switching frequency can make average-value modeling difficult; average-value models based on averaging over a switching period cannot be used directly with hysteresis current controlled inverters. Average-value models are important tools in the design and analysis of power converters. In the modeling and simulation of large converter system (e.g. electric vehicles, ships, and aircraft) [136–138, 168], where the converter system needs to be simulated repeatedly for a wide variety of conditions, both accurate and numerically efficient average-value models are necessary. Perfect hysteresis current control

(PH) is typically assumed in existing average-value models of such inverters. This assumption results in models that cannot account for the inverter behavior during transient command current changes or during overmodulation.

Accurate dynamic modeling is important for stability analysis and power converter optimization over a wide range of operating conditions. Models that can predict transient behavior are useful in the controller design. Operating in the overmodulation region results in an increased fundamental voltage and better dc voltage utilization [169]. The disadvantage of operating in the overmodulation region is the harmonic components generated, but several control methods have been proposed to eliminate particular harmonics or minimize the total harmonic distortion [170]. An average-value model of a three-phase inverter subject to hysteresis current control is sought that accurately represents the inverter behavior in both the normal and overmodulation conditions during both transient and steady-state intervals.

Herein, the modulation index is presented and used to express the relationship between the commanded and the actual inverter voltage magnitudes. This relationship is employed to establish two average-value models of hysteresis current controlled three-phase inverters in the synchronous reference frame. The proposed methods have better accuracy than the primary existing model based on PH during both transient intervals and overmodulation operation and retain the fast simulation run times associated with average-value models. The contributions of this chapter are 1) the presentation of the modulation index, 2) the use of the modulation index to establish the effective voltage and slew-rate limitation models of three-phase inverters subject to hysteresis current control, and 3) the demonstration of the numerical efficiency and accuracy of these models using time-domain simulations and experiments.

The remainder of this chapter is organized as follows. In Section 4.1, relevant notation is presented, and the three-phase inverter system is reviewed in Section 4.2. In Section 4.3, the existing PH model is summarized. In Section 4.4, the modulation

index is defined, and two average-value models – the effective voltage (EV) model and the slew-rate limitation (SRL) model – are proposed. The existing method and the two proposed methods are compared in simulation and experimentally in Section 4.5.

4.1 Notation

Three-phase variables (e.g., voltages and currents) in phase variables $\mathbf{f}_{abc} = [f_{as} \ f_{bs} \ f_{cs}]^T$ can be transformed into an arbitrary reference frame positioned at θ and rotating at ω [75]:

$$\mathbf{f}_{qd0s} = \mathbf{K}_s \mathbf{f}_{abc}, \quad (4.1)$$

where $\mathbf{f}_{qd0s} = [f_{qs} \ f_{ds} \ f_{0s}]^T$ is the three-phase variable in the arbitrary reference frame and the transformation matrix is

$$\mathbf{K}_s = \frac{2}{3} \begin{bmatrix} \cos \theta & \cos(\theta - \frac{2\pi}{3}) & \cos(\theta + \frac{2\pi}{3}) \\ \sin \theta & \sin(\theta - \frac{2\pi}{3}) & \sin(\theta + \frac{2\pi}{3}) \\ \frac{1}{2} & \frac{1}{2} & \frac{1}{2} \end{bmatrix}. \quad (4.2)$$

In a balanced three-phase circuit, the abc variables sum to zero, thus making the 0-sequence value zero. Herein, only the q - and d -axis values are considered:

$$\mathbf{f}_{qds}^e = [f_{qs}^e \ f_{ds}^e]^T, \quad (4.3)$$

where the superscript e denotes transformation to the synchronously rotating reference frame rotating at ω_e . If the inverter is connected to a passive load, the electrical reference is chosen as the position of the synchronous reference frame; if the inverter is connected to the grid, the position of the synchronous reference frame is chosen to align with the grid voltage.

4.2 Three-Phase Inverter System

A basic three-phase inverter with an LC filter is shown in Figure 4.1. As can be seen,

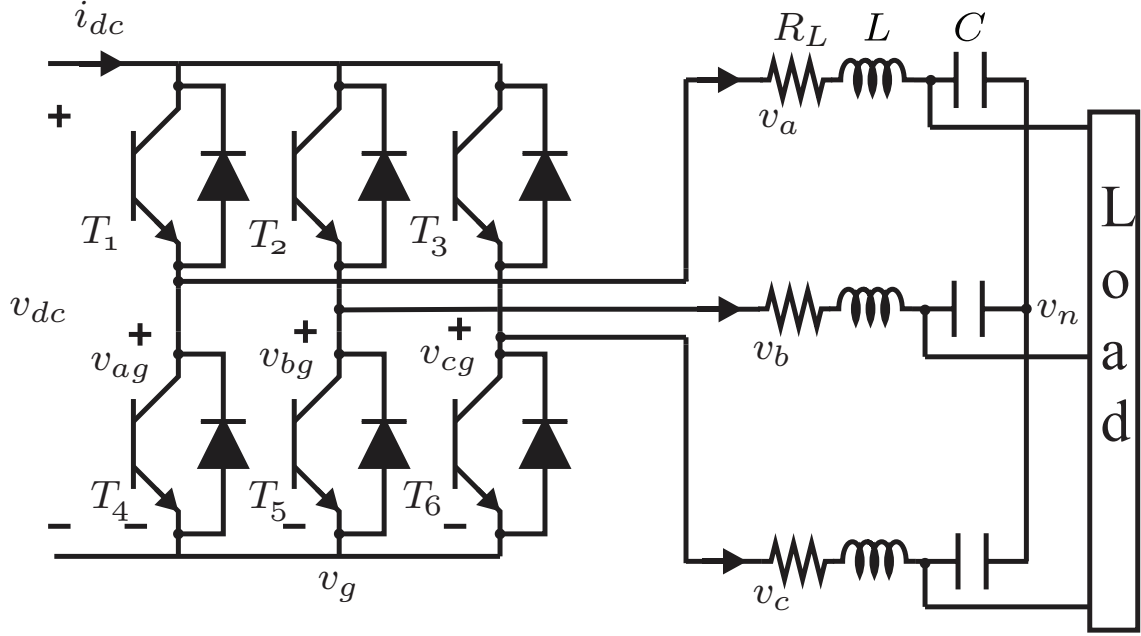


Figure 4.1: Three-phase inverter with output filter system

it consists of six switches and freewheeling diodes which form the three-phase legs. The switches in each phase leg are switched in a complementary manner. In hysteresis current control, the current in each phase leg is compared with the reference current for that phase. If it exceeds the reference current by a specified hysteresis band h , the lower switch is closed. If it falls short of the reference current by h , the upper switch is closed. The three-phase current and voltage in phase variables can be transformed into synchronous reference variables using the reference frame transformation shown in the previous section.

The LC output filter of a three-phase inverter in the synchronously rotating reference frame is shown in Figure 4.2. In this configuration, it is assumed that the inverter is feeding a passive load for which no synchronization is required. In this case, the inverter produces its own reference angle and this angle is chosen as the position of the synchronous reference frame. The differential equations describing

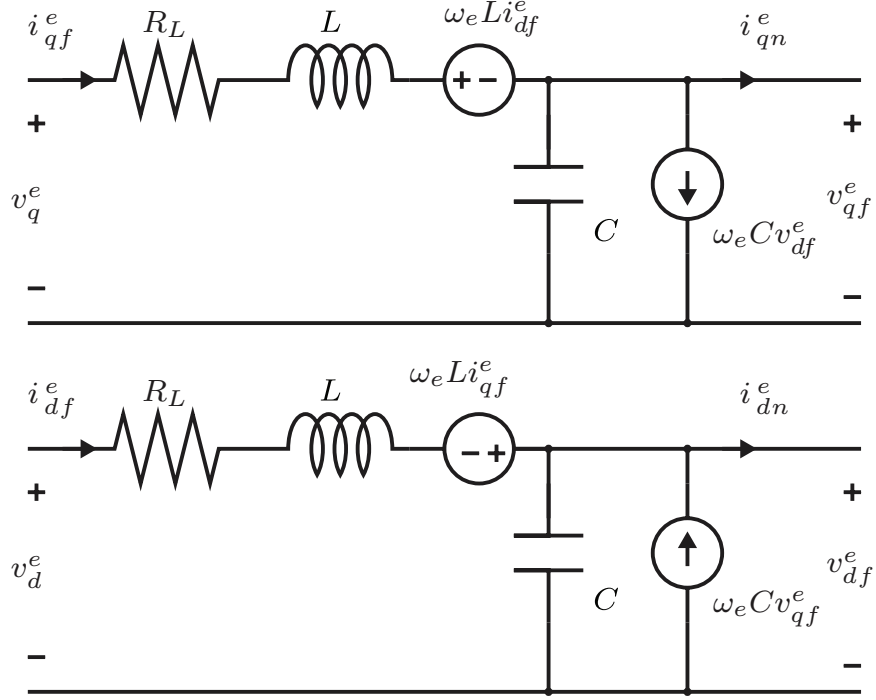


Figure 4.2: Output filter of a three-phase inverter in synchronous reference frame

the behavior of the filter are

$$L \frac{d\mathbf{i}_{qd}^e}{dt} = \mathbf{v}_{qd}^e - R_L \mathbf{i}_{qd}^e - \mathbf{v}_{qdo}^e - \omega_e L \begin{bmatrix} 0 & 1 \\ -1 & 0 \end{bmatrix} \mathbf{i}_{qd}^e, \quad (4.4)$$

$$C \frac{d\mathbf{v}_{qdo}^e}{dt} = \mathbf{i}_{qd}^e - \mathbf{i}_{qdo}^e - \omega_e C \begin{bmatrix} 0 & 1 \\ -1 & 0 \end{bmatrix} \mathbf{v}_{qdo}^e, \quad (4.5)$$

where C is the filter capacitance, L is the filter inductance, R_L is the series resistance associated with the inductance, ω_e is the electrical frequency, and \mathbf{v}_{qd}^e , \mathbf{i}_{qd}^e , \mathbf{v}_{qdo}^e , and \mathbf{i}_{qdo}^e are synchronous reference frame vector representations of the inverter voltage and current and output voltage and current, respectively.

If the inverter is connected to the grid instead of a passive load, synchronization with the grid voltage is necessary. While many methods of synchronization are possible, it is assumed that the synchronous reference frame is aligned with the grid voltage. The output filter in the synchronous reference frame is shown in Figure 4.3.

The output current can be described using

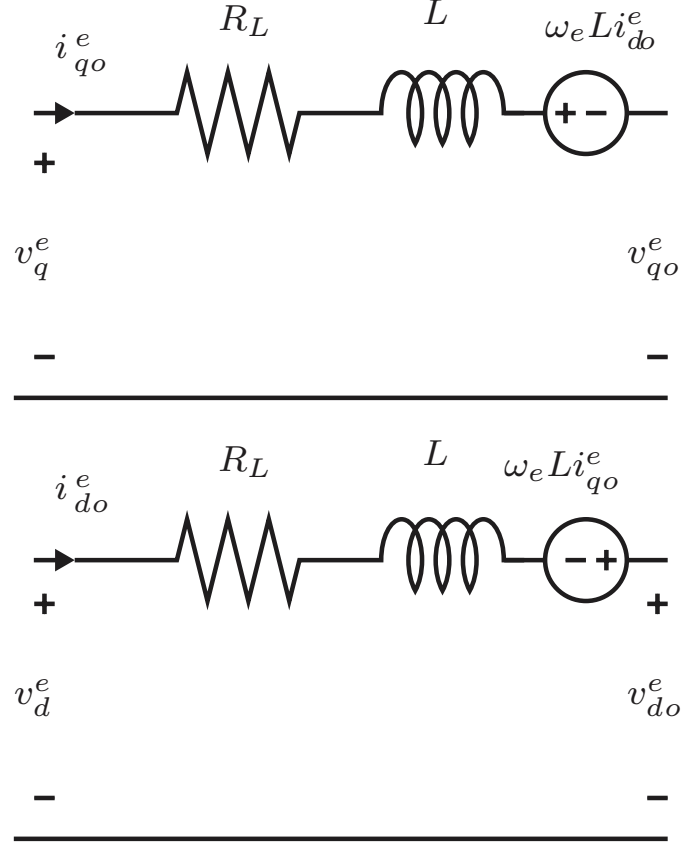


Figure 4.3: Grid-connected three-phase inverter in synchronous reference frame

$$L \frac{d\mathbf{i}_{qdo}^e}{dt} = \mathbf{v}_{qd}^e - R_L \mathbf{i}_{qdo}^e - \mathbf{v}_{qdo}^e - \omega_e L \begin{bmatrix} 0 & 1 \\ -1 & 0 \end{bmatrix} \mathbf{i}_{qdo}^e, \quad (4.6)$$

where L is the inductance of the output filter, R_L is the resistance of the output filter inductor, and \mathbf{v}_{qdo}^e is the grid voltage.

4.3 Perfect Hysteresis Current Control Model

The PH method [75, 146, 171] is the primary existing method of average-value modeling of three-phase inverters. It models the average value of the inductor current in the synchronous reference frame \mathbf{i}_{qdf}^e as equal to the commanded current \mathbf{i}_{qdf}^{e*} :

$$\mathbf{i}_{qdf}^e = \mathbf{i}_{qdf}^{e*}. \quad (4.7)$$

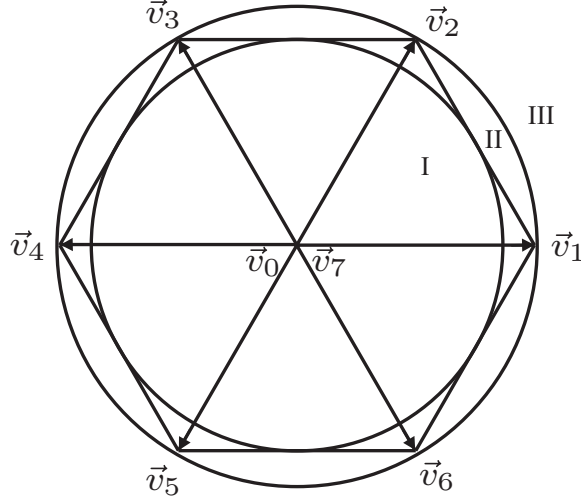


Figure 4.4: Three regions of inverter voltage capability

This reduced-order model neglects the dynamics associated with inductor currents. It has the advantages of reduced run time and model simplicity. However, this method cannot model transient events such as step changes in commanded current accurately. Also, this model does not account for the achievable current given a commanded current. The output voltage of a three-phase inverter is limited by its dc input voltage. This also limits the maximum steady-state currents for given commanded currents. If the commanded current is beyond the limit of achievable current (i.e. in the case of overmodulation), the PH model will have large errors.

4.4 Proposed Average-Value Models

Effective Voltage Limitation

The output voltage of three-phase inverters is limited by the input dc voltage. If the inverter is being controlled in such a way that the inverter voltage should be \mathbf{v}_{qd}^{e*} , this voltage may or may not be available, depending on the dc voltage v_{dc} . An effective voltage \mathbf{v}_{qd}^e will be produced by the inverter instead. The relationship between \mathbf{v}_{qd}^{e*} and \mathbf{v}_{qd}^e is presented and used in the following subsections to construct average-value models of hysteresis current control. In the stationary reference frame, the required

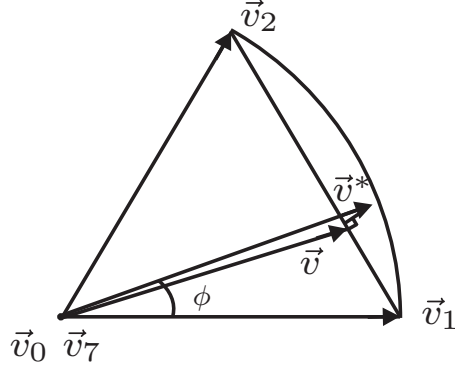


Figure 4.5: Commanded voltage and effective voltage

voltage can be expressed as a space phasor that rotates at ω_e :

$$\vec{v}^* = (v_q^{e*} - jv_d^{e*})e^{j\theta_e}, \quad (4.8)$$

where θ_e is the position of the synchronous reference frame. The effective voltage \vec{v} is a function of the magnitude and the angle of the commanded voltage \vec{v}^* . The six switches in a three-phase inverter have a total of eight switching states. These eight states produce instantaneous inverter voltages in the stationary reference frame that are represented by a regular hexagon with side length equal to $2/3v_{dc}$ as shown in Figure 4.4. If \vec{v}^* lies within the hexagon, the required voltage can be achieved, and the effective voltage will equal the required voltage: $\vec{v} = \vec{v}^*$. If \vec{v}^* falls outside of the hexagon, this voltage cannot be achieved. An effective voltage vector \vec{v} , which will be the closest point on the perimeter of the hexagon as shown in Figure 4.5, will be produced. The average effective voltage produced by the inverter in the synchronously rotating reference frame can be expressed as

$$v_q^e - jv_d^e = \frac{1}{2\pi} \int_0^{2\pi} \vec{v} e^{-j\phi} d\phi, \quad (4.9)$$

where ϕ is the angle of \vec{v}^* . This relationship is symmetric within each sector and is periodic across all six sectors. Therefore, this integral may be computed over $\pi/6$ rad. There are three potential regions of operation based on the dc input voltage v_{dc} .

Region I ($\|\vec{v}^*\| \leq v_{dc}/\sqrt{3}$)

If $\|\vec{v}^*\|$ does not exceed the radius of the inscribed circle, then the effective voltage will be equal to the required voltages for all ϕ :

$$\vec{v} = \vec{v}^*. \quad (4.10)$$

Region II ($v_{dc}/\sqrt{3} < \|\vec{v}^*\| \leq 2v_{dc}/3$)

If $\|\vec{v}^*\|$ does not exceed the radius of the circumscribed circle but is greater than the radius of the inscribed circle, \vec{v} is equal to \vec{v}^* for some ϕ and is a combination of two adjacent voltage vectors for other ϕ . The boundary angle ϕ_1 for the required voltage to cross the hexagon perimeter, as shown in Figure 4.6, can be calculated as

$$\phi_1 = \frac{\pi}{6} - \cos^{-1} \left(\frac{v_{dc}}{\sqrt{3}\|\vec{v}^*\|} \right). \quad (4.11)$$

For values of ϕ in $[0, \phi_1]$, \vec{v} is equal to \vec{v}^* .

From Figure 4.4, a point \vec{v} on the perimeter of the hexagon can be expressed as a convex combination of the two adjacent voltage vectors:

$$\vec{v} = \alpha \vec{v}_1 + (1 - \alpha) \vec{v}_2, \quad (4.12)$$

where $\alpha \in [0, 1]$ and where

$$\vec{v}_1 = \frac{2}{3}v_{dc}, \quad (4.13)$$

$$\vec{v}_2 = \frac{1}{3}v_{dc} + j\frac{1}{\sqrt{3}}v_{dc}. \quad (4.14)$$

The distance between the required voltage vector and the effective voltage on the perimeter of the hexagon should be minimized. The distance can be expressed as

$$\|\vec{v} - \vec{v}^*\|^2 = \left((1 + \alpha)\frac{1}{3}v_{dc} - \|\vec{v}^*\| \cos \phi \right)^2 + \left((1 - \alpha)\frac{1}{\sqrt{3}}v_{dc} - \|\vec{v}^*\| \sin \phi \right)^2. \quad (4.15)$$

The solution that minimizes (4.15) is

$$\alpha = \frac{v_{dc} - 3\|\vec{v}^*\| \sin(\phi - \frac{\pi}{6})}{2v_{dc}}, \quad (4.16)$$

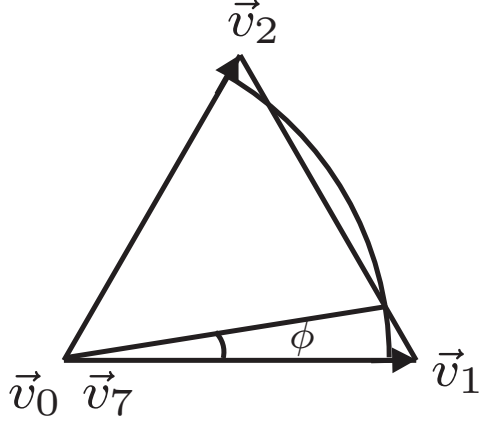


Figure 4.6: Region II

and the effective voltage is given by (5.12). Then, the average effective voltage can be calculated:

$$v_q^e - jv_d^e = \frac{6}{\pi} \left(\int_0^{\phi_1} \vec{v}^* e^{-j\phi} d\phi + \int_{\phi_1}^{\frac{\pi}{6}} \vec{v} e^{-j\phi} d\phi \right). \quad (4.17)$$

Region III ($\|\vec{v}^*\| > 2v_{dc}/3$)

If $\|\vec{v}^*\|$ is greater than the radius of the circumscribed circle, the effective voltage is \vec{v}_1 for some ϕ and is a combination of \vec{v}_1 and \vec{v}_2 as in (5.12) for some other ϕ . By setting α equal to 1 in (5.16), the boundary angle for which the effective voltage remains equal to \vec{v}_1 can be calculated:

$$\phi_2 = \frac{\pi}{6} - \sin^{-1} \left(\frac{v_{dc}}{3\|\vec{v}^*\|} \right). \quad (4.18)$$

Then, the average effective voltage can be calculated:

$$v_q^e - jv_d^e = \frac{6}{\pi} \left(\int_0^{\phi_2} \vec{v}_1 e^{-j\phi} d\phi + \int_{\phi_2}^{\frac{\pi}{6}} \vec{v} e^{-j\phi} d\phi \right). \quad (4.19)$$

If the required modulation index is defined as

$$m^* = \frac{\|\mathbf{v}_{qd}^{e*}\|}{v_{dc}}, \quad (4.20)$$

it can be shown from (4.10), (4.17), and (4.19) that

$$\mathbf{v}_{qd}^e = \frac{m}{m^*} \mathbf{v}_{qd}^{e*}, \quad (4.21)$$

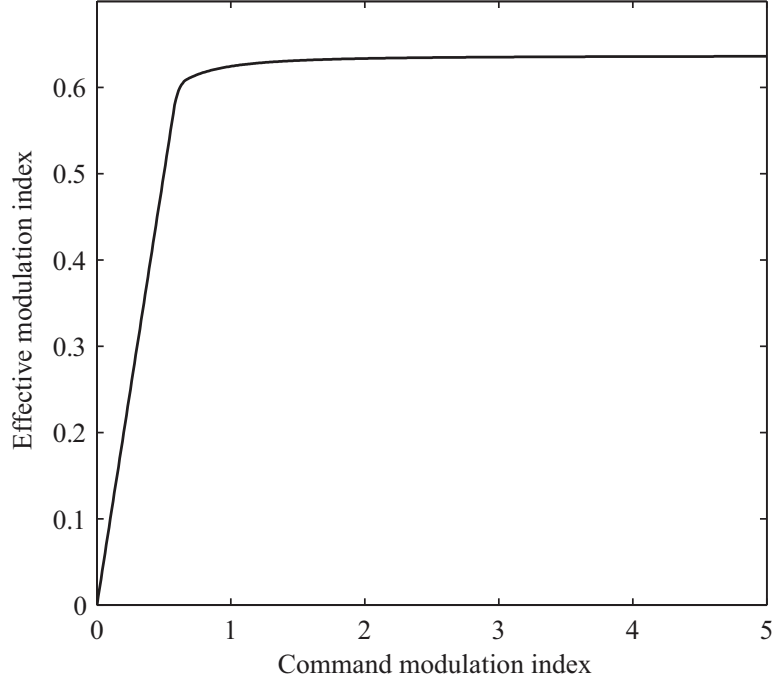


Figure 4.7: Relationship between required and effective modulation index

where the effective modulation index is given by

$$m = \begin{cases} m^*, & m^* \leq \frac{1}{\sqrt{3}} \\ m^* - \frac{3}{\pi} m^* \arccos \frac{1}{\sqrt{3}m^*} + \frac{\sqrt{3}}{\pi} \sqrt{1 - \frac{1}{3m^{*2}}}, & \frac{1}{\sqrt{3}} < m^* \leq \frac{2}{3} \\ \frac{1}{\pi} \left(3m^* \arcsin \left(\frac{1}{3m^*} \right) + \sqrt{1 - \frac{1}{9m^{*2}}} \right), & m^* > \frac{2}{3}. \end{cases} \quad (4.22)$$

The three cases in (4.22) represent the three regions in Figure 4.4. Figure 4.7 shows the relationship between m^* and m . As can be seen, the effective modulation index and the required modulation index have a linear relationship when the required modulation does not exceed $1/\sqrt{3}$. Overmodulation occurs when the required modulation index exceeds $1/\sqrt{3}$, meaning the required voltage cannot be achieved. The effective modulation index approaches $2/\pi$ asymptotically.

Effective Voltage Model

Hysteresis current control can be modeled by using the relationship between required voltage and effective voltage. In this EV model, the three-phase inverter is modeled as if it were voltage regulated. The required voltage is constructed based on the error between the commanded and simulated inductor currents:

$$\mathbf{v}_{qd}^{e*} = kv_{dc}(\mathbf{i}_{qdf}^{e*} - \mathbf{i}_{qdf}^e), \quad (4.23)$$

where $k > 0$ is a modeling gain, \mathbf{i}_{qdf}^{e*} is the commanded current in the synchronous reference frame, and \mathbf{i}_{qdf}^e is the simulated current in the synchronous reference frame. Similar approaches have been described in [132, 143] to model dc-dc converters. This required voltage will be limited by the relationship in the previous subsection, and the effective voltage can be expressed by (4.21). The effective voltage together with the inverter model in Section 4.2 can be used to model the inverter system. A steady-state error between \mathbf{i}_{qdf}^{e*} and \mathbf{i}_{qdf}^e must exist to produce nonzero inverter voltages. Larger values of k can reduce the required steady-state current error, but they will increase stiffness and the resulting simulation run times.

Slew-Rate Limitation Model

Another method to model the hysteresis current control of three-phase inverters is the SRL model. A conceptually similar approach was described in [172] to model hysteresis current control of boost converters. It is based on the observation that the average value of the inductor current would ideally follow the commanded current, but it is subject to rate constraints. That is, the inductor currents will approach the commanded inductor currents at a rate that is limited by the available voltage. The desired inductor current derivatives are expressed as

$$\frac{d\mathbf{i}_{qdf}^e}{dt} = \frac{\mathbf{i}_{qdf}^{e*} - \mathbf{i}_{qdf}^e}{\tau_s}, \quad (4.24)$$

where τ_s is a time constant associated with slew-rate limitation. These desired inductor current derivatives are substituted into (4.4), which is solved for \mathbf{v}_{qd}^e , the value of which is taken as the required voltage \mathbf{v}_{qd}^{e*} . The effective voltage \mathbf{v}_{qd}^e can be found from (4.21), and this value can be used with the inverter model in Section 3 to model the inverter system. This method, unlike the previous method, does not require a steady-state error to exist. There is a tradeoff between accuracy and simulation run time associated with the choice of τ_s . Small values of τ_s can increase accuracy, but they will increase model stiffness and resulting simulation run time.

4.5 Results

To validate the average-value models of hysteresis current control experimentally, a three-phase inverter with output filter is considered. The controller is implemented in a TI F28335 150 MHz microcontroller. The hysteresis control is implemented by sampling the inductor current at 1 MHz and switching if the current falls outside the hysteresis bands. Each average-value model is simulated using MATLAB R2014a Simulink's ode23tb integration algorithm with a relative tolerance of 10^{-3} . The simulations are performed on an Intel Core i7 3.6-GHz processor with 8 GB of memory. Three cases have been studied herein under both transient and steady-state conditions. In Case I and Case II, the three-phase inverter with LC output filter shown in Figure 4.1 is used to supply ac to a three-phase, wye-connected, $2\ \Omega$ resistive load. The inductance L is 0.276 mH, the series resistance R_L associated with the inductor is $0.01\ \Omega$, and the capacitance is $24\ \mu\text{F}$. For these two cases, the hysteresis band is set to 4 A. The q - and d - axis current commands are initially equal to 15 A and -15 A, respectively, and are stepped to -30 A and 30 A, respectively. The input voltage v_{dc} is 200 V in Case I to illustrate the 'normal' operating condition. The total transient time is 4 ms, and the command step change occurs at 2 ms. In Case II, the input voltage is reduced to 100 V to illustrate the overmodulation condition. The total

transient time is 10 ms, and the command step change occurs at 5 ms. In Case III, the three-phase inverter is connected to the grid through a filter inductance. The inductance L is 0.676 mH and the series resistance R_L associated with the inductor is 0.01 Ω . The input voltage v_{dc} is 200 V and the grid voltage is 120 V line to line. For this case, the hysteresis band is set to 1.5 A. The total transient time is 4 ms, and a step current command change from $i_{qds}^{e*} = [50 \ 0]^T$ A to $i_{qds}^{e*} = [25 \ 43.3]^T$ A is applied at 2 ms. All the methods are compared on the basis of numerical efficiency and accuracy. For all the cases, 100 ms of time before and after the transient event is included to evaluate the steady-state behavior of each model. Both the number of time steps required by the ordinary differential equation (ODE) solver and run time (averaged over 100 simulations) are used as measures of efficiency. Accuracy is measured by comparing the inductor current and capacitor voltage waveforms predicted by each average-value model with the simulated detailed waveforms. The rms errors associated with these waveforms are calculated. The total errors are calculated as follows:

$$i_{RMSerror} = \sqrt{\frac{i_{qRMSerror}^2 + i_{dRMSerror}^2}{2}} \quad (4.25)$$

$$v_{RMSerror} = \sqrt{\frac{v_{qRMSerror}^2 + v_{dRMSerror}^2}{2}}. \quad (4.26)$$

These errors are calculated both during the transient interval and during steady-state (the final 50 ms of each simulation). Accuracy is also assessed qualitatively by comparison with the experimentally measured waveforms. The measured values have been sampled at a rate of 5 Msample/s and low-pass filtered with a time constant of 2 μ s to remove measurement noise while retaining switching ripple. The EV model and SRL model each have parameters that may be varied to adjust the tradeoff between numerical efficiency and accuracy. Herein, the values $k = 0.29 \text{ A}^{-1}$ and $\tau = 4.8 \text{ } \mu$ s are used to ensure that the two models have approximately equivalent bandwidth.

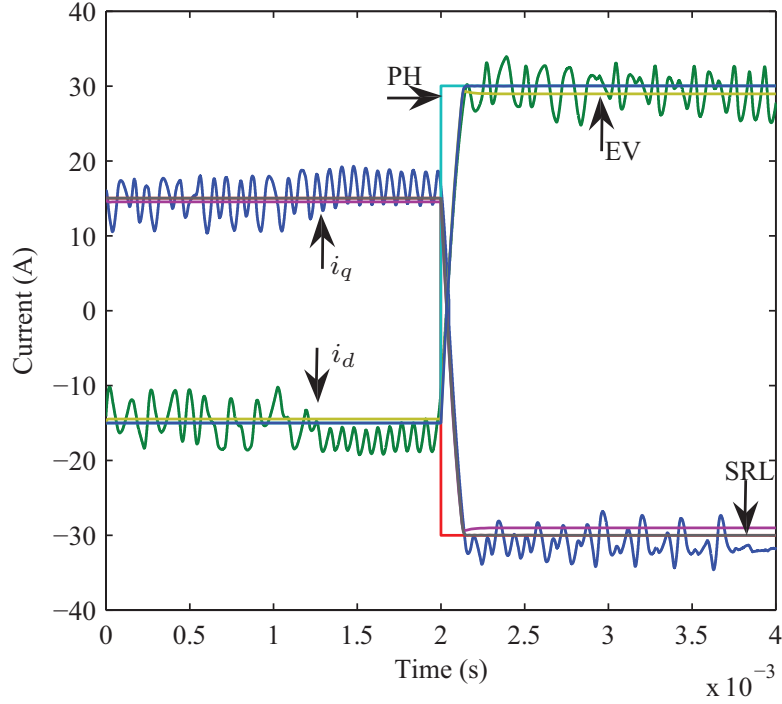


Figure 4.8: Experimental Case I inductor current.

Figure 4.8 and Figure 4.9 show the Case I inductor current and capacitor voltage transient results for the average-value models compared with hardware measurements. It can be seen that the PH model does not follow the transient during the current command step change. The EV model has steady-state errors, which can be reduced by selecting a larger k . The numbers of time steps, run times, and current and voltage rms errors are shown in Table 4.1. The rms errors are calculated during the transient interval and during the final 50 ms to assess the transient and steady-state accuracy, respectively. From the table, the SRL model has better numerical efficiency than the EV model. The PH model takes less time because it is a reduced-order model. Compared with the detailed model, both the proposed models have the advantage of short simulation time. The SRL model is the most accurate method in this case.

Figure 4.10 and Figure 4.11 show the Case II inductor current and capacitor voltage transient results for the average-value models compared with hardware mea-

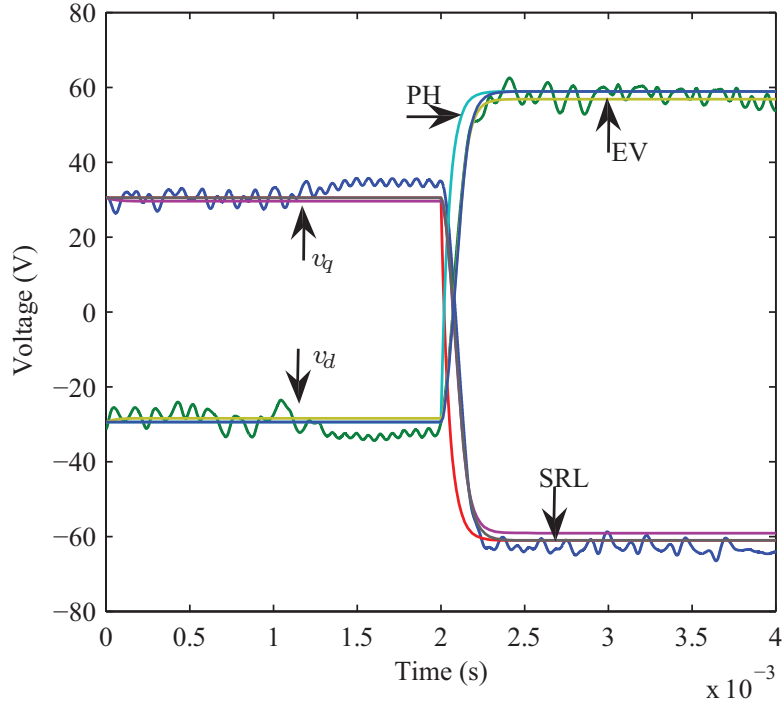


Figure 4.9: Experimental Case I capacitor voltage.

Table 4.1: Simulation Results for Case I

			Transient		Steady state	
Method	Time steps	Run time (ms)	Current error (A)	Voltage error (V)	Current error (A)	Voltage error (V)
Detailed	139173	269.6	—	—	—	—
PH	328	22.2	5.27	7.28	2.30	1.50
EV	460	57.8	2.48	2.23	2.43	2.18
SRL	409	45.2	2.42	2.01	2.30	1.50

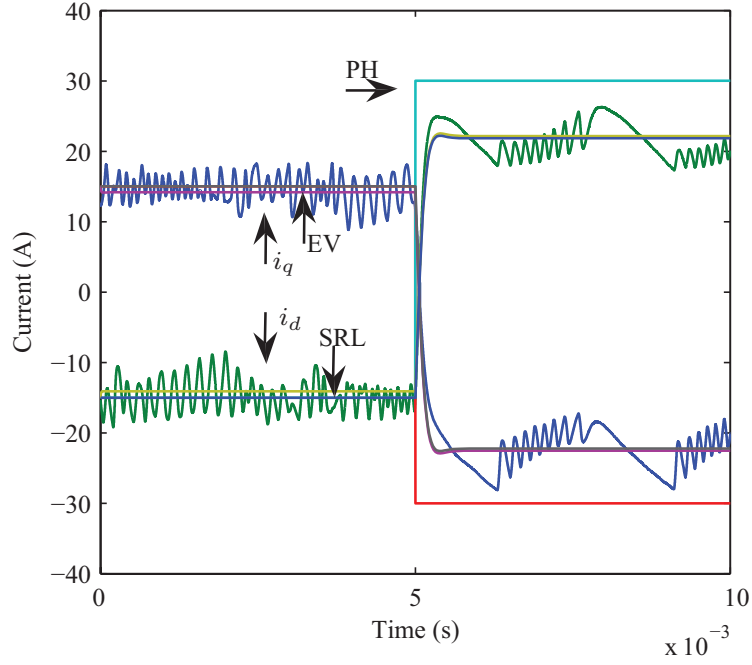


Figure 4.10: Experimental Case II inductor current.

measurements. It can be seen that PH model can model neither the transient event nor the overmodulation region accurately. Both the EV model and the SRL model have better accuracy compared to the PH model. Again, the EV model has steady-state errors. The numbers of time steps, run times, and current and voltage rms errors are shown in Table 4.2. Unlike in Case I, the PH model has significant steady-state error in the overmodulation region. While the SRL model retains its slight accuracy advantage over the EV model in the transient interval, it is seen that the EV model does not have the same steady-state accuracy disadvantage in the overmodulation region; it has slightly less steady-state error than the SRL model. The SRL model remains faster than the EV model. As expected, both are somewhat slower than the reduced-order PH model and much faster than the detailed model.

Figure 4.12 shows the Case III grid injection current transient results for the average-value models compared with hardware measurements. Again, PH model

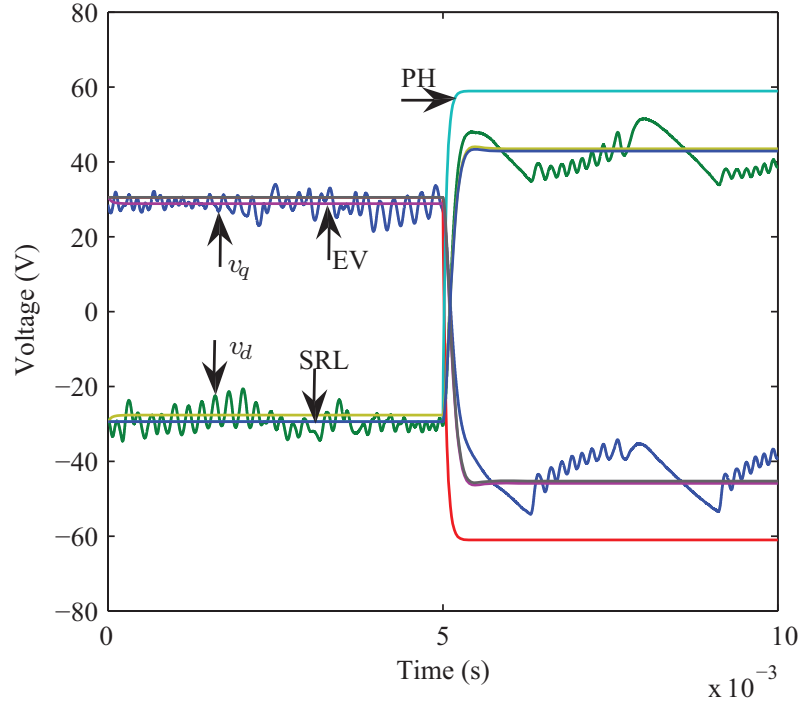


Figure 4.11: Experimental Case II capacitor voltage.

Table 4.2: Simulation Results for Case II

			Transient		Steady state	
Method	Time steps	Run time (ms)	Current error (A)	Voltage error (V)	Current error (A)	Voltage error (V)
Detailed	73714	163.4	—	—	—	—
PH	322	21.8	7.22	13.44	8.58	17.00
EV	445	56.2	2.70	4.25	2.80	5.07
SRL	366	42.7	2.66	4.13	2.81	5.08

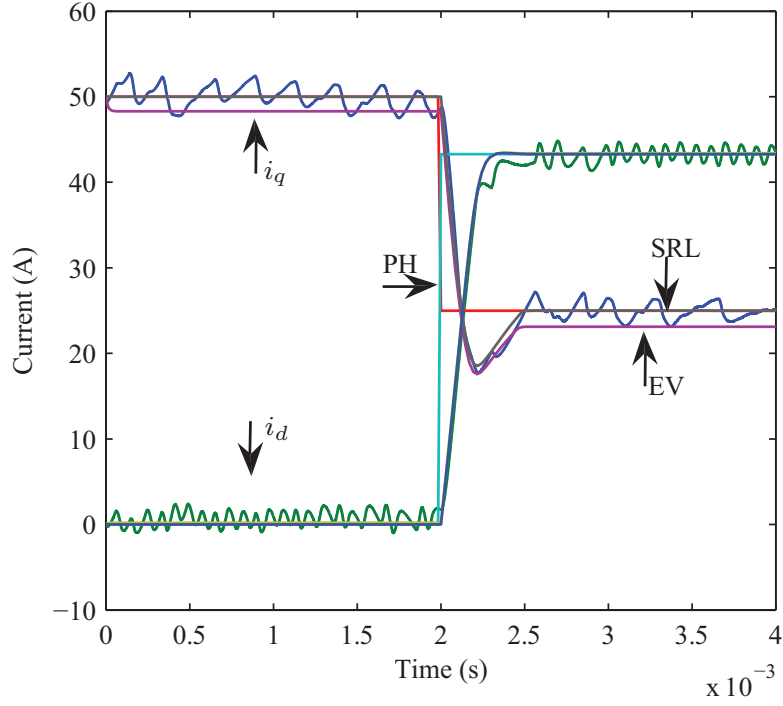


Figure 4.12: Experimental Case III grid current.

Table 4.3: Simulation Results for Case III

			Transient	Steady state
Method	Time steps	Run time (ms)	Current error (A)	Current error (A)
Detailed	97571	241.9	—	—
PH	109	22.5	4.61	0.91
EV	508	62.7	1.39	1.41
SRL	363	43.8	0.96	0.91

cannot model the transient accurately; the EV model has some steady-state error. The numbers of time steps, run times, and current rms errors are shown in Table 4.3. SRL model is the most accurate model and it is faster than the EV model.

4.6 Conclusion

The primary existing method of average-value modeling hysteresis current controlled three-phase inverter is the PH model. This model has reduced order and results in fast simulation run times. However, it cannot accurately model either the system transient behavior or the overmodulation condition. This chapter presents the relationship between required voltage and effective voltage and uses this relationship to formulate two average-value models of hysteresis current controlled three-phase inverters: the EV model and the SRL model. The average-value models are compared both in simulation and experimentally with different scenarios. The proposed average-value models have better accuracy in both transient and overmodulation conditions than the existing PH model while maintaining the advantage of fast simulation for average-value models.

Chapter 5 Average-Value Modeling of Hysteresis Current Controlled Brushless DC Motor Drives

Current-regulated brushless dc motors have been widely used in electric vehicles. It is important to have accurate and numerically efficient models for system analysis and design. Hysteresis current control has significant advantages, such as fast dynamic response and robustness. This chapter presents two new average-value models of motor drives for brushless dc machines under hysteresis current control. The new models are compared with a detailed model in terms of simulation run time and rms error under a variety scenarios. The proposed average-value models accurately represent the behavior of the drive and can be used in modeling and design.

Brushless dc motors are widely used in electric vehicles [37–39] with the advantages of high efficiency and torque density [46–48]. Among different control methods, hysteresis current control offers benefits such as robust control, fast dynamic response, and overcurrent protection, which are valuable in electric vehicle applications [98]. One perceived disadvantage of hysteresis current control is varying switching frequency, but this has been addressed by advanced techniques that adjust the hysteresis band to stabilize the switching frequency [125–127]. The uncertain switching frequency and the general dissimilarity of hysteresis current control with voltage-regulated inverter control methods has posed modeling difficulty. In particular, an average-value model cannot be directly obtained. Average-value models are beneficial for control design and for simulation of larger scale systems (e.g., the multiconverter system found in an electric vehicle [133, 173, 174]). For this reason, it has been argued in [139] that hysteresis current control has been understudied in the literature. The primary existing method of average-value modeling of hysteresis current controlled inverters is to assume perfect hysteresis current control [75, 146]. If perfect hysteresis current control is obtained, the machine exhibits reduced-order

dynamics and high-bandwidth control of torque is possible. However, this method does not account for transient current changes or the effects of overmodulation on achievable currents. This chapter presents the relationship between commanded voltage magnitude and effective voltage magnitude and uses this relationship to establish two average-value models of hysteresis current controlled motor drives in the rotor reference frame. Simulation results of average-value model compared with detailed model demonstrate each model's accuracy and numerical efficiency.

5.1 Brushless DC Machine

An inverter-fed brushless dc motor is shown in Figure 5.1. The voltage equations in the rotor reference frame are [75]

$$v_{qs}^r = r_s i_{qs}^r + \omega_r L_d i_{ds}^r + \omega_r \lambda_m + L_q p i_{qs}^r \quad (5.1)$$

$$v_{ds}^r = r_s i_{ds}^r - \omega_r L_q i_{qs}^r + L_d p i_{ds}^r, \quad (5.2)$$

where p is an operator signifying differentiation with respect to time, v_{qs}^r and v_{ds}^r are the q - and d -axis voltages, respectively, i_{qs}^r and i_{ds}^r are the q - and d -axis currents, respectively, r_s is the stator resistance, L_q and L_d are the q - and d -axis inductances, respectively, λ_m is the flux linkage due to the permanent magnet, ω_{rm} is the mechanical rotor speed, P is the number of poles, and ω_{rm} is the electrical rotor speed. The electromagnetic torque is given by

$$T_e = \left(\frac{3}{2}\right) \left(\frac{P}{2}\right) [\lambda_m i_{qs}^r + (L_d - L_q) i_{qs}^r i_{ds}^r]. \quad (5.3)$$

The input current can be expressed as

$$i_{dc} = \frac{3}{2} \frac{v_{qs}^r i_{qs}^r + v_{ds}^r i_{ds}^r}{v_{dc}}, \quad (5.4)$$

where v_{dc} is the inverter dc voltage. In general, values of a three-phase quantity (i.e., voltage or current) can be expressed in vector form as

$$\mathbf{f}_{qds}^r = [f_{qs}^r \ f_{ds}^r]^T. \quad (5.5)$$

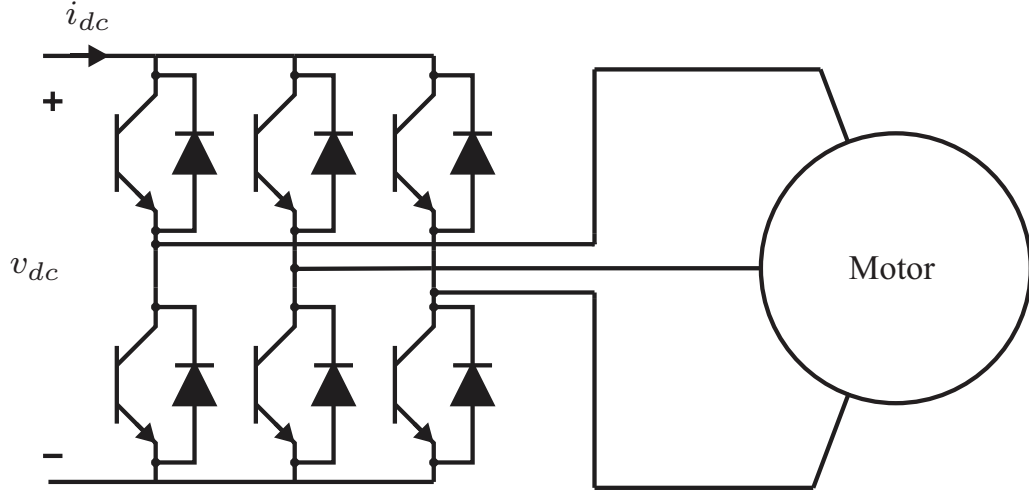


Figure 5.1: Brushless dc motor drive system

5.2 Perfect Hysteresis Model

The primary existing method of average-value modeling of hysteresis current control, discussed in [75], assumes perfect hysteresis control, i.e., the average value of the stator current in the rotor reference frame is always equal to the commanded current. The modeling for a three-phase inverter is as follows

$$\mathbf{i}_{qds}^r = \mathbf{i}_{qds}^{r*}. \quad (5.6)$$

where \mathbf{i}_{qds}^{r*} is the three-phase commanded current in q - and d -axis. The voltages can be modeled from (5.1) and (5.2) with the time derivatives of the currents neglected. This model is a reduced-order method in which the dynamics associated with the stator currents are neglected. This is advantageous in terms of run time and model simplicity, but it leads to inaccuracy during transient events such as step changes in required torque.

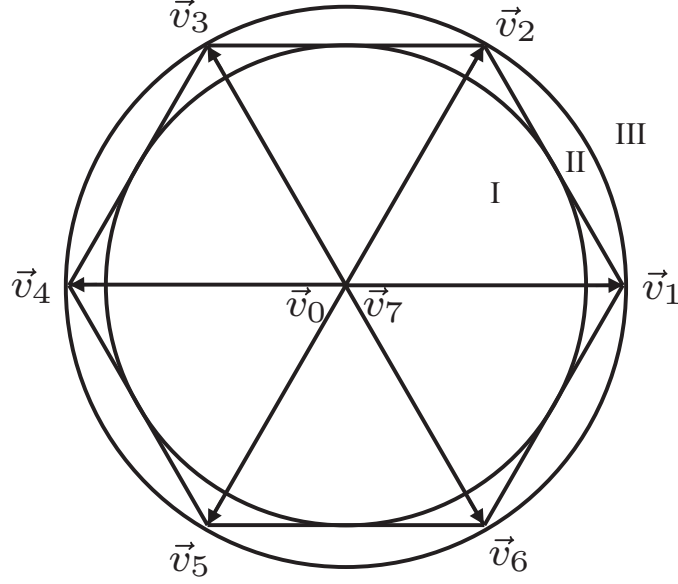


Figure 5.2: Inverter voltage capability in stationary reference frame

5.3 Proposed Average-Value Models

Effective Voltage Limitation

In three-phase inverters, the voltage that can be applied to the stator windings of the machine is limited by the dc voltage. This limits the rate at which the machine currents can change and the range of steady-state currents that are achievable for a given machine speed. If a voltage of \mathbf{v}_{qds}^{r*} is commanded from the inverter, this voltage may or may not be available. Instead, an effective voltage \mathbf{v}_{qds}^r will be applied to the machine. The relationship between \mathbf{v}_{qds}^{r*} and \mathbf{v}_{qds}^r is used in the following subsections to construct average-value models of hysteresis current control.

The commanded voltage can be expressed as a space phasor that rotates at ω_r in the stationary reference frame:

$$\vec{v}^* = (v_{qs}^{r*} - jv_{ds}^{r*})e^{j\theta_r}, \quad (5.7)$$

where θ_r is the electrical rotor position. The actual voltage that can be produced by the inverter can be expressed as \vec{v} . The relationship between \vec{v}^* and \vec{v} is a function of the magnitude and angle of \vec{v}^* . The six switches in an inverter system form a hexagon

with sides equal to $2v_{dc}/3$ [75], as shown in Figure 5.2. If \vec{v}^* lies within the hexagon, $\vec{v} = \vec{v}^*$. If \vec{v}^* falls outside the hexagon, \vec{v} is the closest point on the perimeter of the hexagon, which may be one of the vertices or some point on one of the edges. The average effective voltage produced by the inverter in the rotor reference frame can be expressed as

$$v_{qs}^r - jv_{ds}^r = \frac{1}{2\pi} \int_0^{2\pi} \vec{v} e^{-j\theta_r} d\theta_r. \quad (5.8)$$

There are three regions of potential operation.

Region I ($\|\vec{v}^*\| \leq v_{dc}/\sqrt{3}$)

If the commanded voltage \vec{v}^* falls inside the inscribed circle of the hexagon, then the actual voltage will be equal to the commanded voltage:

$$\vec{v} = \vec{v}^* \quad (5.9)$$

Region II ($v_{dc}/\sqrt{3} < \|\vec{v}^*\| < 2v_{dc}/3$)

If the commanded voltage \vec{v}^* falls between the inscribed circle and the circumscribed circle of the hexagon, part of the time \vec{v} is equal to \vec{v}^* . The boundary angle where the commanded voltage crosses the hexagon, as shown in Figure 5.3, can be calculated as

$$\phi_1 = \frac{\pi}{6} - \cos^{-1} \left(\frac{v_{dc}}{\sqrt{3}\|\vec{v}^*\|} \right). \quad (5.10)$$

From 0 to ϕ_1 , \vec{v} is equal to \vec{v}^* .

From Figure 5.2, \vec{v} can be expressed as the weighted sum of two adjacent voltage vectors and the zero voltage vector:

$$\vec{v} = \alpha_1 \vec{v}_1 + \alpha_2 \vec{v}_2 + \alpha_3 \vec{v}_{0,7}, \quad (5.11)$$

where α_1 , α_2 , and α_3 are weights associated with each voltage vector. The zero voltage vectors will be used when the commanded voltage falls inside the hexagon. Only the

non-zero voltage vectors will be used when the commanded voltage is outside of the hexagon. The weights associated with each voltage vector should minimize the distance between the commanded voltage vector and the effective voltage on the perimeter of the hexagon. When the commanded voltage is outside of the hexagon, $\alpha_1 = \alpha$ and $\alpha_2 = 1 - \alpha$ for some α . The effective voltage can be written as

$$\vec{v} = \alpha \vec{v}_1 + (1 - \alpha) \vec{v}_2, \quad (5.12)$$

where

$$\vec{v}_1 = \frac{2}{3} v_{dc} \quad (5.13)$$

and

$$\vec{v}_2 = \frac{1}{3} v_{dc} + j \frac{1}{\sqrt{3}} v_{dc}. \quad (5.14)$$

By substitution of (5.13) and (5.14), the distance can be expressed as

$$\|\vec{v} - \vec{v}^*\|^2 = \left((1 + \alpha) \frac{1}{3} v_{dc} - \|\vec{v}^*\| \cos \theta_r \right)^2 + \left((1 - \alpha) \frac{1}{\sqrt{3}} v_{dc} - \|\vec{v}^*\| \sin \theta_r \right)^2, \quad (5.15)$$

which should be minimized. The solution can be expressed as

$$\alpha = \frac{v_{dc} - 3\|\vec{v}^*\| \sin(\theta_r - \frac{\pi}{6})}{2v_{dc}}, \quad (5.16)$$

and the effective voltage can be expressed using (5.12). Then, the average effective voltage can be calculated by integration over half of one sector.

$$v_{qs}^r - jv_{ds}^r = \frac{6}{\pi} \left(\int_0^{\phi_1} \vec{v}^* e^{-j\theta_r} d\theta_r + \int_{\phi_1}^{\frac{\pi}{6}} \vec{v} e^{-j\theta_r} d\theta_r \right) \quad (5.17)$$

Region III ($\|\vec{v}^*\| > 2v_{dc}/3$)

When the commanded voltage lies in region III, the effective voltage will be \vec{v}_1 for some time, it will be a combination of \vec{v}_1 and \vec{v}_2 as in (5.12) for some time, and it will be \vec{v}_2 for some time. The boundary angle the voltage stays at \vec{v}_1 can be calculated from (5.16) by setting α equal to 1,

$$\phi_2 = \frac{\pi}{6} - \sin^{-1} \left(\frac{v_{dc}}{3\|\vec{v}^*\|} \right). \quad (5.18)$$

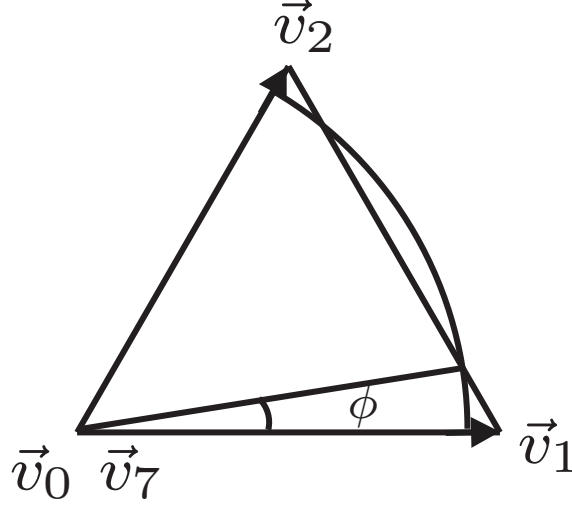


Figure 5.3: Region II

Then, the average effective voltage can be calculated by integration over half of one sector.

$$v_{qs}^r - jv_{ds}^r = \frac{6}{\pi} \left(\int_0^{\phi_2} \vec{v}_1 e^{-j\theta_r} d\theta_r + \int_{\phi_2}^{\frac{\pi}{6}} \vec{v} e^{-j\theta_r} d\theta_r \right) \quad (5.19)$$

It can be shown that if the commanded modulation index is defined as

$$m^* = \frac{\|\mathbf{v}_{qds}^{r*}\|}{v_{dc}}, \quad (5.20)$$

then

$$\mathbf{v}_{qds}^r = \frac{m}{m^*} \mathbf{v}_{qds}^{r*}, \quad (5.21)$$

where the effective modulation index is given by (5.22)

$$m = \begin{cases} m^*, & m^* \leq \frac{1}{\sqrt{3}} \\ m^* - \frac{3}{\pi} m^* \arccos \frac{1}{\sqrt{3}m^*} + \frac{\sqrt{3}}{\pi} \sqrt{1 - \frac{1}{3m^{*2}}}, & \frac{1}{\sqrt{3}} < m^* \leq \frac{2}{3} \\ \frac{1}{\pi} \left(3m^* \arcsin \left(\frac{1}{3m^*} \right) + \sqrt{1 - \frac{1}{9m^{*2}}} \right), & m^* > \frac{2}{3}. \end{cases} \quad (5.22)$$

The three cases in (5.22) correspond to the three regions labeled in Figure 5.2. The relationship between m^* and m is shown in Figure 5.4. It can be seen that the effective modulation index equals the commanded modulation index when it is less than or equal to $1/\sqrt{3}$. When the commanded modulation index exceeds $1/\sqrt{3}$, the

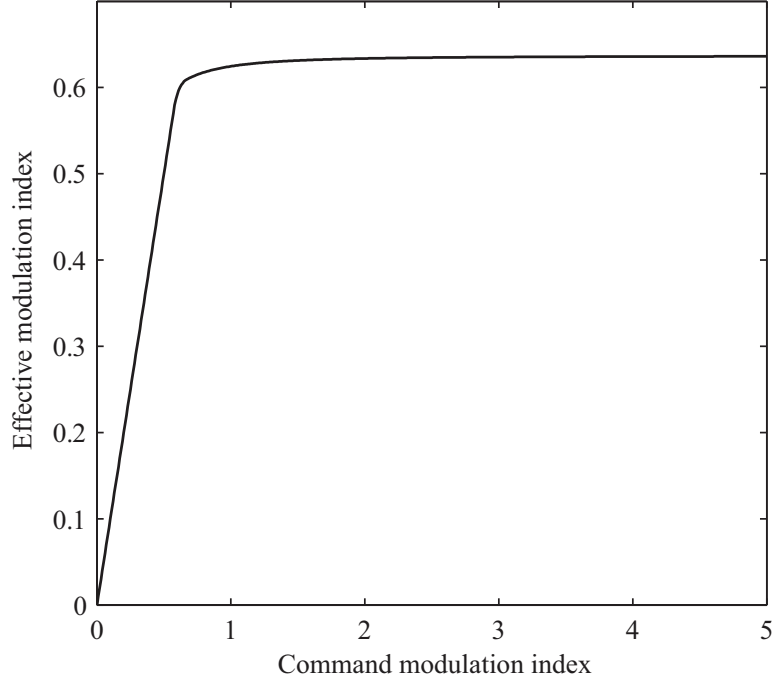


Figure 5.4: Relationship between commanded and effective modulation index

commanded voltage cannot be satisfied, and the effective modulation index asymptotically approaches $2/\pi$.

Effective Voltage Model

Having established the relationship between commanded voltage and effective voltage, it is possible to set forth average-value models of hysteresis current control. In the first, the drive system is modeled as if it were a voltage-regulated drive and a voltage command is constructed based on the error between the commanded and actual current. In particular, the commanded voltage is proportional to the current error:

$$\mathbf{v}_{qds}^{r*} = kv_{dc}(\mathbf{i}_{qds}^{r*} - \mathbf{i}_{qds}^r), \quad (5.23)$$

where \mathbf{i}_{qds}^{r*} is the commanded current in the rotor reference frame and k is a constant. In this way, the current error is used to define a commanded voltage as if the drive was a voltage regulated drive. Similar approaches have been used to model dc-dc

converters [132, 143]. Having established a commanded voltage, the relationship in the previous subsection can be used to express the effective voltage. This voltage can be used with the machine model in Section 5.1 to model the drive system. This model requires a steady-state error between \mathbf{i}_{qds}^{r*} and \mathbf{i}_{qds}^r in order to produce voltage. By increasing the value of k , this steady-state current error can be reduced, but this will also increase simulation run time.

Slew-Rate Limitation Model

An alternative method to modeling the hysteresis current control of brushless dc motor drives is based on natural slew-rate limits that are inherent to the stator currents. A similar approach has been described in [172] to model boost converters. In particular, the stator currents will approach the commanded stator currents at a rate that is limited by the available voltage. If the desired stator current derivatives are expressed as

$$p\mathbf{i}_{qds}^r = \frac{\mathbf{i}_{qds}^{r*} - \mathbf{i}_{qds}^r}{\tau_s} \quad (5.24)$$

where τ_s is a time constant and these desired stator current derivatives are substituted into (5.1) and (5.2), then the commanded voltages can be determined. The relationship between the commanded voltage and the effective voltage can be used to express \mathbf{v}_{qds}^r and this can be used with the machine model in Section 5.1 to complete the model. Unlike the previous method, this method does not require a steady-state error. The accuracy of this model can be improved by choosing small values of τ_s , but this increases run time.

5.4 Simulation Results

A motor with the parameters shown in Table 5.1 is simulated using a detailed model and the above three average models. Each method is simulated using MATLAB R2013a Simulink's ode23tb integration algorithm with a relative tolerance of 10^{-4} .

A detailed model of the motor drive and each of the methods described above are simulated for two cases. In Case I, the q -axis current command follows a square wave in which the current command is stepping between 0 A and $2\sqrt{2}$ A. The current command is stepped at rotor angles ranging from 0 and $\pi/6$. The simulated q - and d -axis currents and torque are shown in Figure 5.6 and Figure 5.7, respectively. It can be seen that the perfect hysteresis current method does not model the transient well. Both effective voltage and slew-rate-limitation methods model the transient well. The steady-state error associate with effective voltage method is reduced by choosing a large enough k . Also, the number of simulation time steps and the rms errors associated with the currents, voltages, and torque with respect to the detailed model are given in Table 5.2. In Case II, the PI controller shown in Fig. 5.5 is used to regulate the speed of the motor. The commanded currents are calculated from the commanded torque using (5.3). A step change in load torque from 0.5 N·m to 1.5 N·m is applied at 0.05 s. The simulated q - and d -axis currents and torque are shown in Figure 5.8 and Figure 5.9, respectively. The large plots show the current and torque over the length of the simulation. The small plots show these variables in closer proximity to the step increase in load torque command. It can be seen that the perfect hysteresis method does not model the transient accurately. Also, the number of simulation time steps and the rms errors associated with the currents, voltages, and torque with respect to the detailed model are given in Table 5.3. From the simulation results, it can be seen that the proposed methods can be simulated considerably faster than the detailed model. They require significantly more time than the perfect hysteresis method but provide considerably more accuracy in applications in which transient behavior is of interest. Furthermore, both proposed methods have similar accuracy, but the effective voltage method runs more quickly than the slew-rate-limitation method.

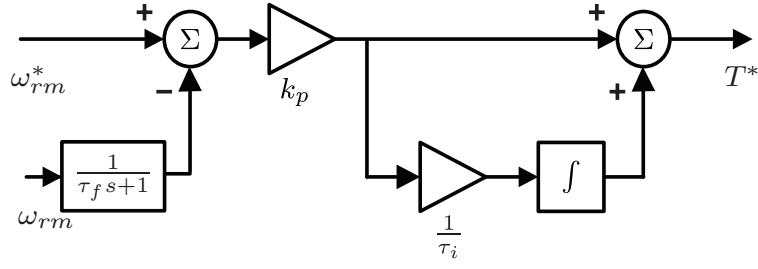


Figure 5.5: Closed-loop controller for motor drive

Table 5.1: Motor Parameters

Parameter	Value
V_{dc}	120 V
r_s	2.98 Ω
L_q	11.4 mH
L_d	11.4 mH
λ_m	0.156 V·s
J	10^{-4} kg·m ²
ω_r	120π rad/s
h	0.1 A
P	4
τ_s	1 μ s
k	9 A ⁻¹
τ_f	159.15 μ s
τ_i	3.33 ms
k_p	0.2 N·m/(rad/s)

Table 5.2: Number of Output Calls and RMS Error for Each Method

Method	Time Steps	i_{qs} (A)	i_{ds} (A)	T (N·m)
Detailed	28359	—	—	—
PH	211	0.6684	0.1500	0.3128
EV	2765	0.1309	0.1615	0.0613
SRL	5129	0.1384	0.1608	0.0648

PH is perfect hysteresis, EV is effective voltage,
and SRL is slow-rate limitation.

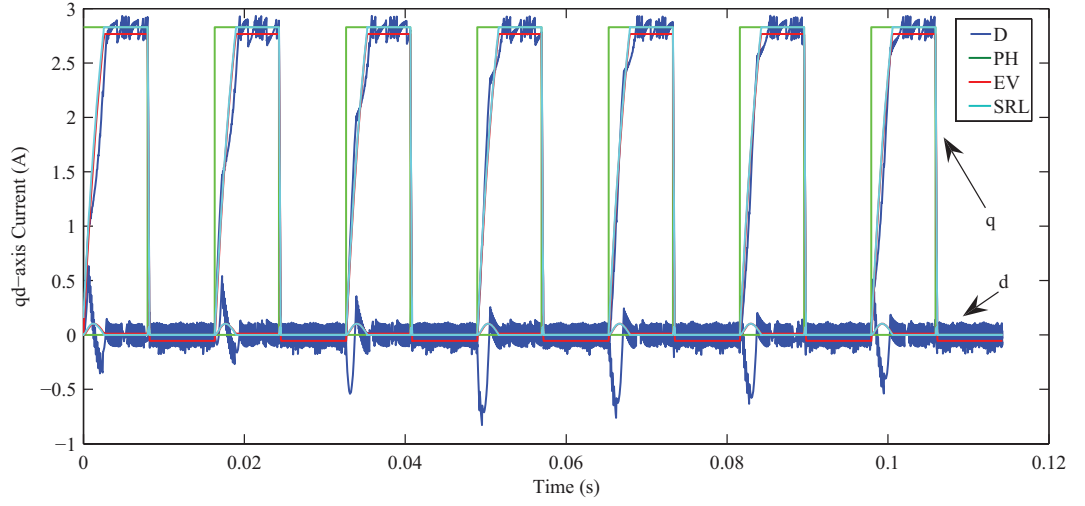


Figure 5.6: Simulated q - and d -axis currents. D signifies the detailed model. PH signifies perfect hysteresis. EV signifies the effective voltage, SRL signifies slew-rate-limitation. d signifies d -axis currents, q signifies q -axis currents.

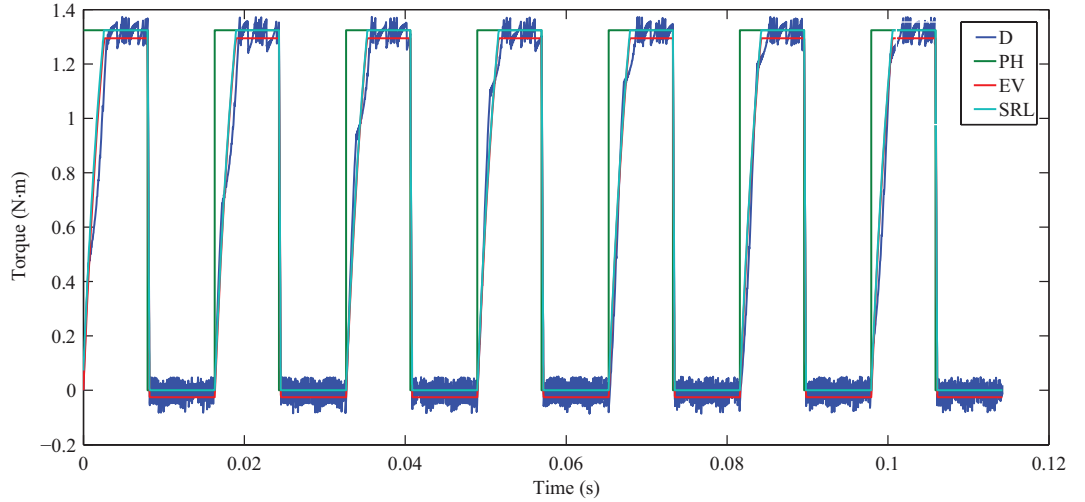


Figure 5.7: Simulated torque. D signifies the detailed model. PH signifies perfect hysteresis. EV signifies the effective voltage, SRL signifies slew-rate-limitation.

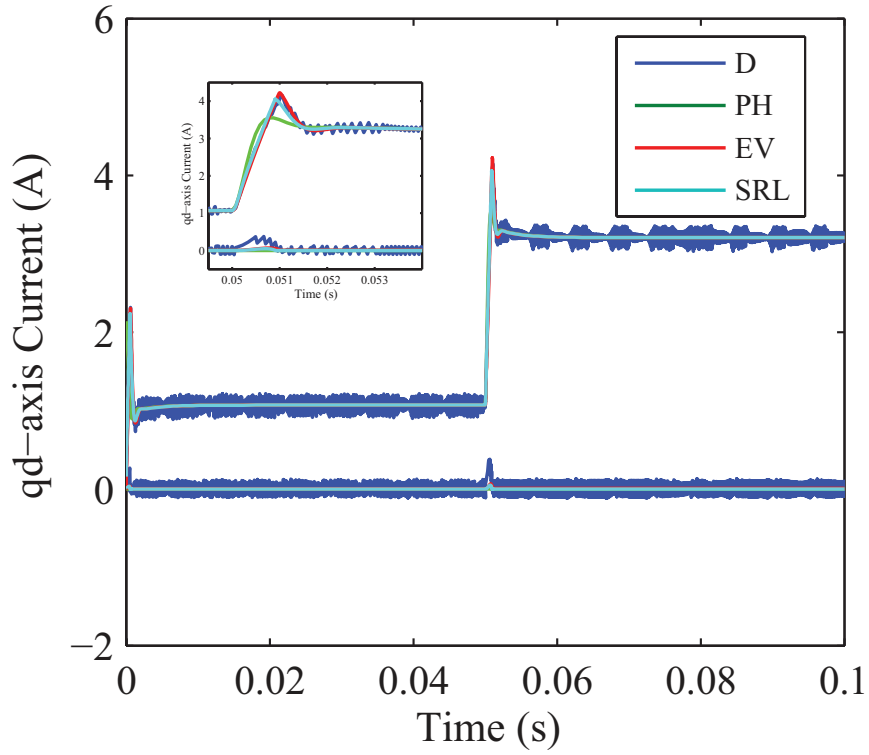


Figure 5.8: Simulated q - and d -axis currents. D signifies the detailed model. PH signifies perfect hysteresis. EV signifies the effective voltage, SRL signifies slew-rate-limitation.

Table 5.3: Number of Output Calls and RMS Error for Each Method

Method	Time Steps	i_{qs} (A)	i_{ds} (A)	T (N·m)
Detailed	40638	—	—	—
PH	477	0.1289	0.0747	0.0603
EV	1028	0.0737	0.0735	0.0345
SRL	1402	0.0743	0.0737	0.0348

PH is perfect hysteresis, EV is effective voltage,
and SRL is slew-rate limitation.

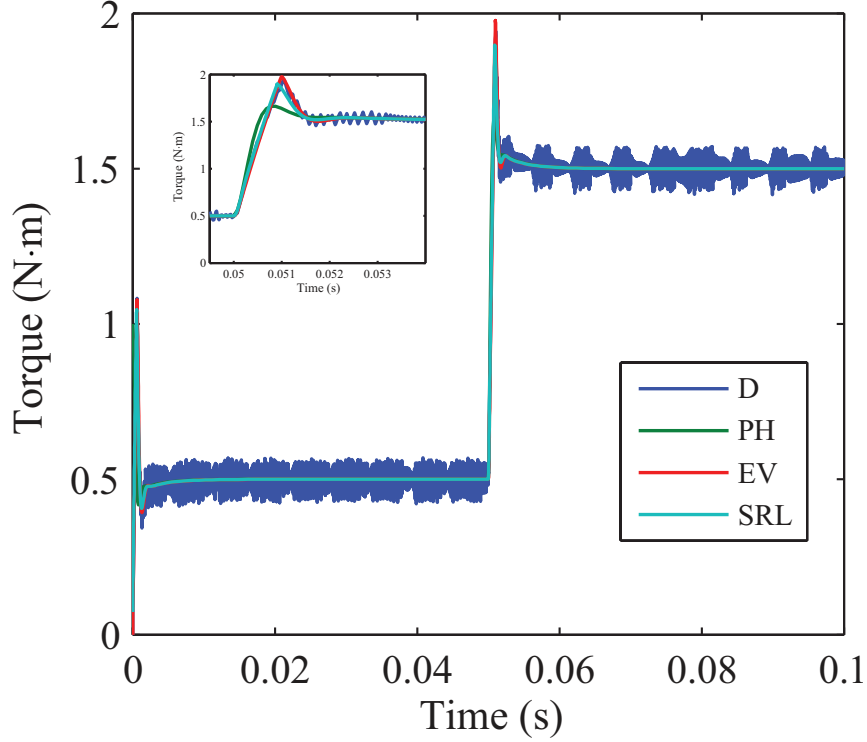


Figure 5.9: Simulated q - and d -axis torque. D signifies the detailed model. PH signifies perfect hysteresis. EV signifies the effective voltage, SRL signifies slew-rate-limitation.

5.5 Experimental Validation

To validate the proposed methods of average-value modeling of hysteresis current control experimentally, a permanent magnetic brushless dc motor with parameters shown in Table 5.4 is studied. The controller is implemented in a TI F28335 150 MHz microcontroller. The hysteresis current control is implemented by sampling the motor current at 1 MHz and switching if the current falls outside the hysteresis band. The current are measured using a sample rate of 5 Msample/s, and the measured values have been low-pass filtered with a time constant of 2 μ s to remove measurement noise while retaining switching ripple. Each average-value model is simulated using MATLAB R2014a Simulink's ode23tb integration algorithm with a relative tolerance of 10^{-4} . The simulations are performed on an Intel Core i7 3.6-GHz processor with 8 GB of memory. A step current command change from $i_{qds}^r = [25; 0]^T$ A to $i_{qds}^r =$

$[15; 0]^T$ A is applied at 0.25 s and the total simulation time is 0.5 s. Figure 5.10 shows the motor current simulation results zoomed in for the transient. The number of simulation time steps, time, and the rms errors associated with the currents with respect to the detailed model are given in Table 5.5. The rms errors are calculated during the 3 ms transient period. Figure 5.11 shows the motor current results for the average-value models compared with hardware measurements. It can be seen that the PH model does not follow the transient during the current command step change. Both the proposed effective voltage model and slew-rate limitation model have better accuracy compared with the existing perfect hysteresis current model.

Table 5.4: Motor Parameters

Parameter	Value
V_{dc}	250 V
r_s	0.1 Ω
L_q	1.297 mH
L_d	1.316 mH
λ_m	0.277 V·s
ω_r	120 π rad/s
P	4
h	2.5 A
k	100 A ⁻¹
τ_s	1 μ s

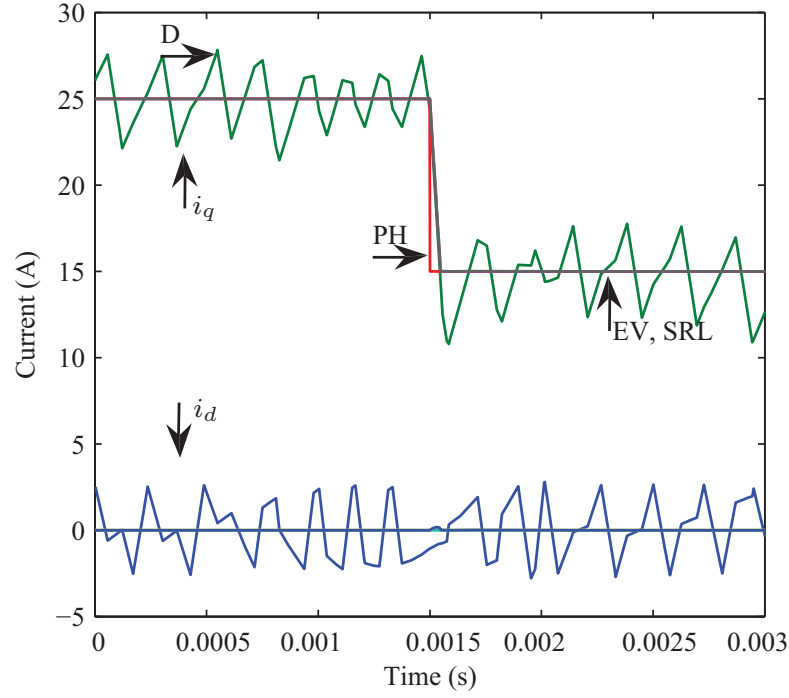


Figure 5.10: Simulation comparison

Table 5.5: Number of Output Calls and RMS Error for Each Method

Method	Time Steps	Time (ms)	i_{qs} (A)	i_{ds} (A)
Detailed	303832	729.4	—	—
PH	103	20.6	2.01	1.74
EV	452	42.7	1.85	1.73
SRL	567	48.9	1.82	1.74

PH is perfect hysteresis, EV is effective voltage,
and SRL is slow-rate limitation.

5.6 Conclusion

This chapter presents two average-value models of hysteresis current control for brushless dc motor drives. The relationship between commanded and effective voltage is established and used to implement an effective voltage model and a slow-rate-limitation model. The proposed models predict the average dynamic behavior of the motor drive

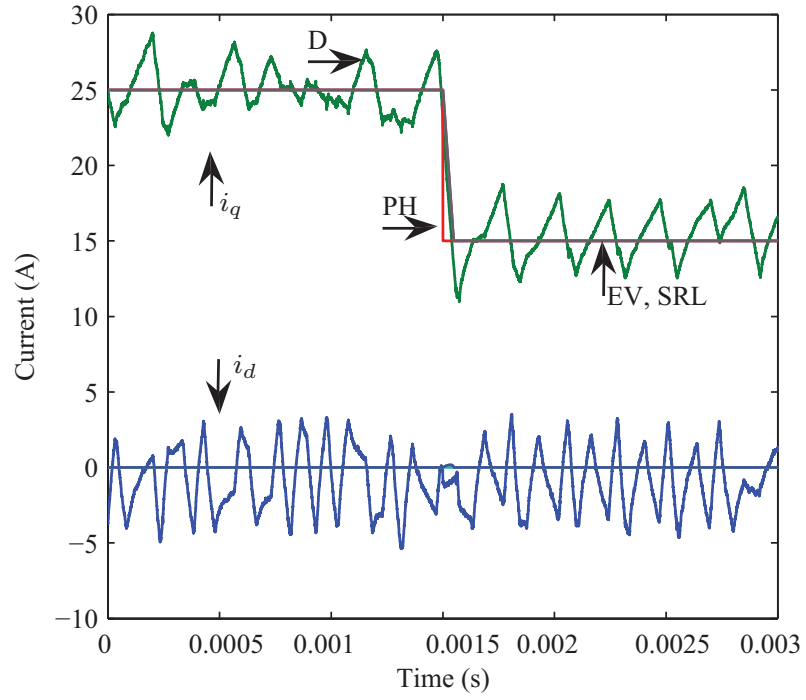


Figure 5.11: Hardware validation

accurately and efficiently. The new models of hysteresis current control can improve applications of average-value modeling of torque, speed control in which hysteresis current control is employed [175–177].

Chapter 6 Conclusion and Future Work

With the prevalence of power electronics, the modeling and simulation of power converter systems has become more and more important. Especially in large systems such as electrical vehicles, electric ships, and aircraft, where multiple power converter systems exist. The design and optimization of those large systems require accurate and fast average-value models. Also, those power converters need to be designed to operate in a wide range of operating conditions to meet energy and performance demand. Compared to the commonly used PWM control, hysteresis current control is a simple and direct control method which does not depend on the system parameters. However, average-value modeling of hysteresis current control in power converters is understudied. The basic method is to model it as perfect hysteresis current control. This method will introduce large current and voltage errors during transient events such as command current step change or fail to model the actual system in the case of a three-phase inverter operating in the overmodulation region. Several other methods for average-value modeling hysteresis current control in dc-dc converter exist. Those models will either have steady-state errors or take more time steps to simulate.

The contribution of this work is the proposal of slew-rate-limitation method of average-value modeling of hysteresis current control. It is based on the rate limit which the inductor current can change. The slew-rate limitation model is first applied to a boost converter. A wide variety of scenarios have been simulated, such as step current command, step input voltage, and step output resistance. Compared with five existing methods, the proposed method is as accurate but faster. It is found out that the proposed method has a tradeoff between accuracy and simulation run time which offers modeling flexibility. Frequency-domain analysis is also provided. It is shown that the proposed model is capable of predicting the frequency-domain characteristics

of the converter, making it suitable for use in control design and small-signal stability analysis as well. The proposed model is validated experimentally with a step current command and a step output resistance.

Then, average-value modeling of hysteresis current control in three-phase inverters is proposed. Three-phase inverters are transformed into the synchronous reference frame by using reference frame theory. The perfect hysteresis current control model is the primary existing method of average-value modeling of hysteresis current control in three-phase inverters. However, this method cannot accurately model either the transient event or the overmodulation region. Another contribution of this work is the modeling of three-phase inverters in the overmodulation region. This paper defines the overmodulation index as the ratio of required output voltage to the input dc voltage and formulates a mathematical equation for its three operating regions. Two new methods are proposed for the average-value modeling of hysteresis current controlled three-phase inverters: an effective voltage model and a slew-rate limitation model. Both simulation results and hardware validation are shown for a step current command in both the normal operating region and in the overmodulation region when the inverter is connected to a passive load through an LC filter and a step current command when the inverter is connected to the grid through an L filter. It is shown that the proposed models accurately predict the transient events and also have the advantage of fast simulation from average-value models.

Finally, methods for average-value modeling of hysteresis current controlled motor drives are proposed. The permanent magnet brushless dc motor drive system is transformed into the rotor reference frame. The proposed effective voltage model and slew-rate limitation model for three-phase inverters can also apply to motor drives. Simulation results for pulse train current command and step torque command are shown. Compared with existing perfect hysteresis model, the proposed methods have better accuracy during transient events. The proposed models are validated

experimentally with open loop current command.

During the research, several interesting topics arise which can be extended to potential future work. These topics are described in more detail below.

It has been found out that during the experiment, the system suffers from the noise issue. Switching induced noise interfering with cables results in inaccurate and false microcontroller inputs. This can be improved by changing the cable routing. Future work could include optimal design and packaging power converters to reduce electromagnetic interference (EMI), both in the control circuit and in the high voltage circuit. EMI can be reduced by optimal design the circuit layout and cable routing.

This work includes mathematical modeling of the capacitor and inductor parasitic resistance in boost converters. In order to improve the model accuracy further, nonideal switches, IGBT parasitic resistance and capacitance could also be included in future work. In this work, only a resistive load is studied. Future work could be extended to analyze the system with different types of load, such as constant current, constant power, and constant impedance load.

Frequency-domain study is important for the control design and stability analysis. This work focuses mainly on the time-domain simulations of power converters. Frequency response simulation of the average-value models of boost converter compared with the detailed model is shown. Future work could be extended to the study of frequency response of the proposed models in three-phase inverters and motor drives.

It is noted that the proposed average-value models of hysteresis current control in this work could be applied to other converter as well, such as buck, rectifier, and induction motor drives. The proposed slew-rate limitation model for boost converters, three-phase inverters and brushless dc motor drives and the proposed effective-voltage model for three-phase inverters and brushless dc motor drives in this work make the modeling and simulation of hysteresis current controlled power converters highly accurate (compared to existing models) and highly numerically efficient (compared

to detailed models). They can be used in the simulation and optimization of large power converter systems such as electric vesicles, electric ships, and electric aircraft, where multiple converter systems need to be simulated repeatedly. The proposed modulation index in this work also improves the modeling accuracy of three-phase circuits in the overmodulation region.

Chapter A Appendix

This appendix gives the design details of a bidirectional dc-dc converter used for hardware validation in the lab. Input voltage, output voltage, power, operating frequency, and ripple requirements are specified for the design. The inductance and capacitance are calculated based on the input, output, and ripple requirements. The voltage and current ratings for the inductor and capacitor are specified. The switching device, dual insulated gate bipolar transistor (IGBT) module, is selected based on operating voltage and frequency. Heat sink design is based on the worst case scenario heat generated by the switching losses and conducting losses of the IGBT module. Pictures of the lab equipments are also shown.

A.1 Bidirectional DC-DC Converter Design

Bidirectional dc-dc converters are widely used in energy storage and conversion systems, such as in an electric vehicle or solar energy storage. It has the ability to control the power flow in either direction.

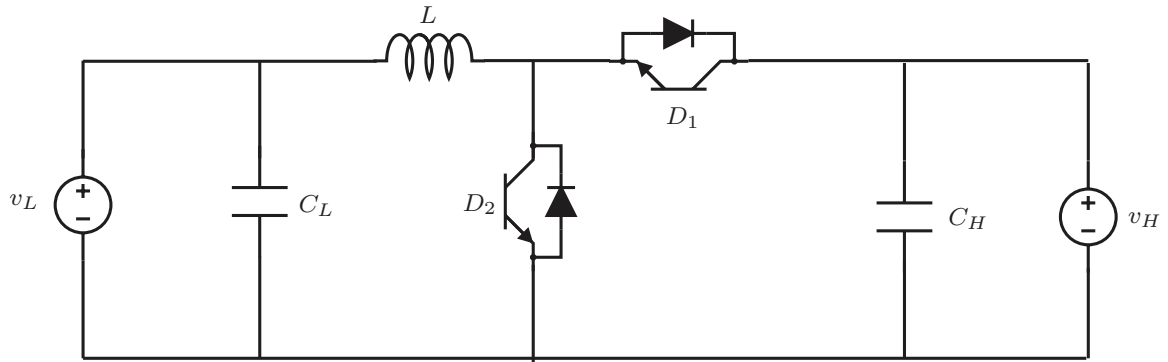


Figure A.1: Bidirectional dc-dc converter

Inductance and Capacitance Calculation

A bidirectional dc-dc converter shown in Figure A.1 is built in the lab for hardware validation. It works as a boost converter if a voltage source is connected to the left and a load is connected to the right, and it works as a buck converter if a voltage source is connected to the right and a load is connected to the left. The switches should be able to carry current in both directions. This is realized by paralleling an IGBT with a diode. The left side is referred to as the low voltage side and the right side is referred to as the high voltage side. The high voltage side and low voltage side have voltage and current relationships:

$$V_H = \frac{1}{1-d}V_L. \quad (\text{A.1})$$

$$i_H = (1-d)i_L, \quad (\text{A.2})$$

where the subscript H denotes the high voltage side, L denotes the low voltage side, and d is the boost converter duty cycle. From (A.1)

$$V_L = (1-d)V_H. \quad (\text{A.3})$$

On the low voltage side, the current and voltage has relationship

$$L \frac{\Delta i}{\Delta t} = V_L, \quad (\text{A.4})$$

where Δt is dT , the time when switch D_1 is on in one period T , and Δi is specified by the ripple requirements.

The converter is designed to have a low side voltage of 150 V, a high side voltage of 300 V, a nominal inductor current of 50 A, and a steady-state switching frequency of 10 kHz. The ripple requirements are 10% for the inductor current and 1% for the capacitor voltage. The inductance can be calculated by substituting (A.3) into (A.4),

$$L = \frac{(1-d)V_H dT}{\Delta i_L}. \quad (\text{A.5})$$

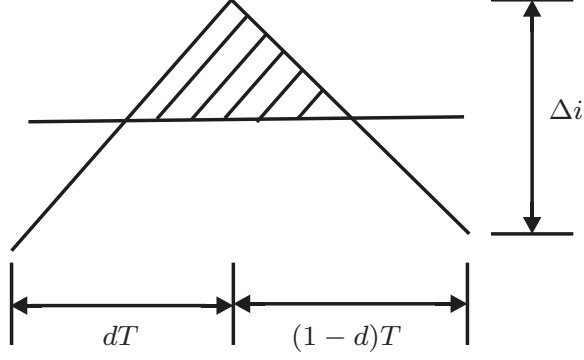


Figure A.2: Low voltage side capacitor current in one cycle

When d is equal to 0.5, the above equation has the maximum value of 1.5 mH. So the inductance should be larger than or equal to 1.5 mH.

The inductor current changes linearly in one switching period and can be approximate by a triangular wave. Figure A.2 shows the current waveform on the low voltage side capacitor. The triangle waveform is centered at the load current with a peak to peak value specified by the ripple requirement. The low voltage side capacitor has voltage and current relationship

$$C_L \frac{dV_L}{dt} = i_L. \quad (\text{A.6})$$

Take integral on both sides of the above equation

$$\int C_L dV_L = \int i_L dt. \quad (\text{A.7})$$

The right hand side has the geometric meaning of the shaded area of the triangle in Figure A.2. So the low voltage side capacitance can be calculated

$$C_L = \frac{1}{8} T \frac{\Delta i_L}{\Delta V_L}, \quad (\text{A.8})$$

where ΔV_L is specified by the ripple requirement. Substitute Δi_L from (A.5) and ΔV_L from the ripple requirement (A.3), (A.8) can be simplified into

$$C_L = \frac{1}{8L} dT^2 V_L. \quad (\text{A.9})$$

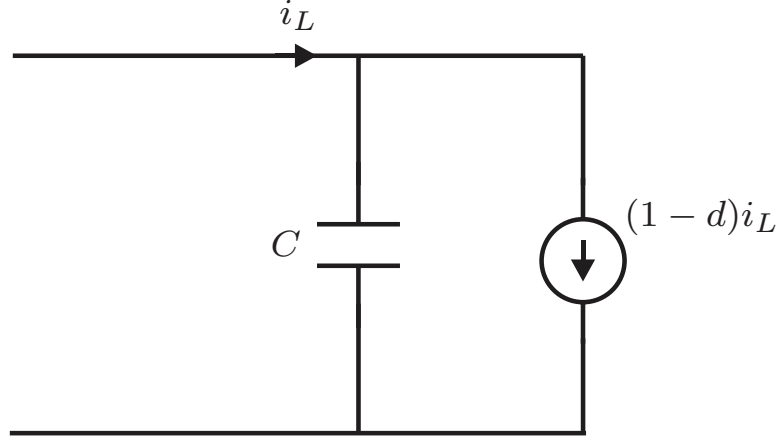


Figure A.3: High voltage side circuit

The above equation has a maximum value of $83.4 \mu\text{F}$ when d is 1. So the low voltage side capacitance should be larger than or equal to $83.4 \mu\text{F}$ to maintain the ripple requirement.

The high voltage side circuit can be simplified as Figure A.3. The capacitor should maintain the output current in one cycle. The voltage and current relationship can be expressed as

$$C_H \frac{\Delta V_H}{\Delta t} = i_L - (1 - d)i_L, \quad (\text{A.10})$$

where Δt is equal to $(1 - d)T$ and ΔV_H is specified by the ripple requirement. Substitute those values into the above equation and simplify it, the high voltage side capacitance can be calculated

$$C_H = \frac{(1 - d)dTi_L}{\Delta V_H}. \quad (\text{A.11})$$

The above equation has a maximum value of $417 \mu\text{F}$ when d is 0.5. So the high voltage side capacitance should be larger than or equal to $417 \mu\text{F}$.

Voltage and Current Ratings

After calculating circuit parameters based on the design requirements, current and voltage ratings should also be specified. Although the converter is designed to have

voltage ratings of 150 V and 300 V, for safety consideration the values are doubled when choosing the capacitors. So the capacitors should have voltage ratings of 300 V and 600 V for low voltage side and high voltage side, respectively. Current rating calculations are shown as follows.

For the low voltage side capacitor, the current waveform is shown in Figure A.2. The current in one cycle can be expressed as

$$i_C = \begin{cases} \frac{(1-d)V_H}{L}t - \frac{1}{2}\frac{(1-d)V_H}{L}dT, & t \leq dT \\ -\frac{dV_H}{L}(t-dT) + \frac{1}{2}\frac{(1-d)V_H}{L}dT, & t > dT \end{cases} \quad (\text{A.12})$$

The rms value can be calculated

$$i_{Crms} = \sqrt{\frac{1}{T} \left(\int_0^{dT} \left(\frac{(1-d)V_H}{L}t - \frac{1}{2}\frac{(1-d)V_H}{L}dT \right)^2 dt + \int_0^{(1-d)T} \left(-\frac{dV_H}{L}(t-dT) + \frac{1}{2}\frac{(1-d)V_H}{L}dT \right)^2 dt \right)}, \quad (\text{A.13})$$

which can be simplified as

$$i_{Crms} = \frac{1}{2\sqrt{3}} \frac{(1-d)V_H dT}{L}. \quad (\text{A.14})$$

The above equation has a maximum value of 1.45 A when d is 0.5. So the current rating for the low side capacitor when doubled is 2.9 A.

For the high voltage side capacitor, the current waveform is shown in Figure A.4. The rms value of the current can be expressed as

$$i_{Crms} = \sqrt{\frac{1}{T} \left(\int_0^{(1-d)T} (di_L)^2 dt + \int_0^{dT} ((d-1)i_L)^2 dt \right)}, \quad (\text{A.15})$$

which can be simplified as

$$i_{Crms} = \sqrt{d(1-d)} i_L. \quad (\text{A.16})$$

The above equation has a maximum value of 25 A when d is 0.5. So the current rating for the high side capacitor when doubled is 50 A.

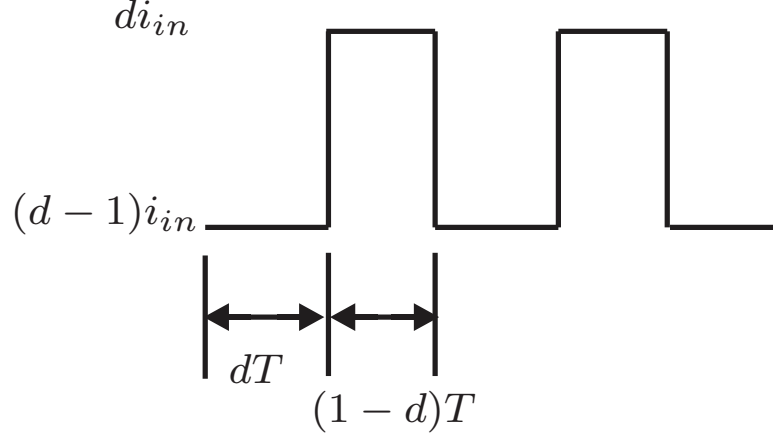


Figure A.4: High voltage side capacitor current in one cycle

Heatsink Design

One IGBT dual module CM150DY-24A is used to implement the two switches in Figure A.1. The IGBT heat sink design procedure is as follows.

In order to design for the worst case scenario, two cases are taken into consideration. The first case is when the current is 100 A, which is twice the designed value. In this case, the junction temperature is assumed to be as high as the maximum value, which is 150 °C. The second case is when the current is 50 A, which is the designed value. In this case, the junction temperature is assumed to be the middle point of room temperature 25 °C and the maximum junction temperature 150 °C, which is 87.5 °C. The thermal equivalent circuit is shown in Figure A.5. All the values used in the calculation are listed in Table A.1 from the datasheet. The analogy between a thermal circuit and an electrical circuit is as follows: power dissipation in a thermal circuit is like current, temperature is like voltage, and thermal resistance is like resistance. The total loss is the sum of conduction loss and switching loss. The power dissipation in the transistor and the diode can be expressed as [178]

$$T = \frac{1}{2}VI + (E_{on} + E_{off})f, \quad (\text{A.17})$$

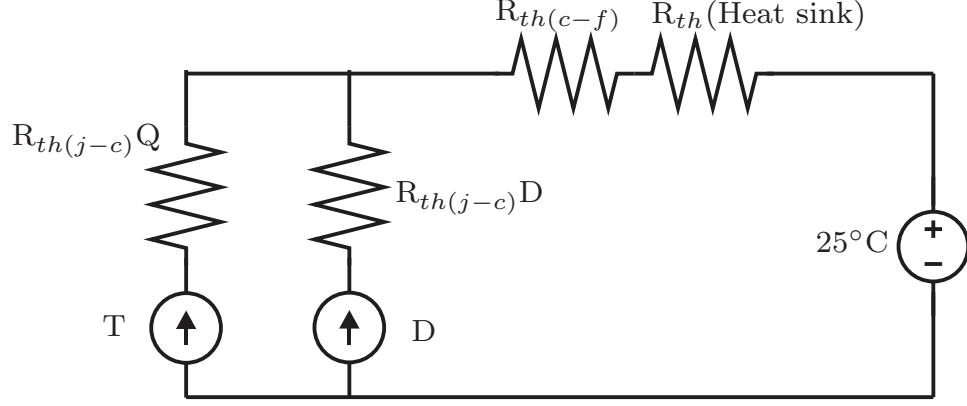


Figure A.5: Equivalent thermal circuit

Table A.1: Values used in thermal calculation

Conditions		100A 150 °C	50A 87.5 °C
Switching losses	Transistor	$E_{on}=6\text{mJ/pulse}$	$E_{on}=3.5\text{mJ/pulse}$
		$E_{off}=15\text{mJ/pulse}$	$E_{off}=8\text{mJ/pulse}$
	Diode	$E_{rr}=8\text{mJ/pulse}$	$E_{rr}=5\text{mJ/pulse}$
Conduction losses	Transistor	$V=2.4\text{V}$	$V=1.5\text{V}$
	Diode	$V=2\text{V}$	$V=1.8\text{V}$

$$D = \frac{1}{2}VI + E_{rr}f, \quad (\text{A.18})$$

where T represent transistor, D represent diode, f is the switching frequency. In the above equations, $\frac{1}{2}$ means that the device is on for half of the time in one period. Solving the thermal equivalent circuit in Figure A.5 for the two cases, the heat sink thermal resistance should be smaller than or equal to $0.14 \text{ Km}^2/\text{W}$ for the worst case scenario design.

Sensors and Microcontroller

Three current sensors are required to measure the low side current, high side current, and inductor current, respectively. In this lab, HASS 50-S are being used. The current measuring range is $-150 \text{ A} - 150 \text{ A}$. Two voltage sensors are required to

measure the low side capacitor voltage and high side capacitor voltage, respectively. In this lab, LV 25-P/SP2 are being used. The voltage measuring range is 10 V – 1500 V. The control is implemented by a TI F28335 32-Bit 150 MHz microcontroller with built-in PWM and analog-to-digital conversion (ADC) capabilities.

A.2 Lab Pictures

The bidirectional dc-dc converter is shown in Figure A.6. The high side capacitance is 470 μF and the low side capacitance is 167 μF . The inductance is 1.5 mH at 10 kHz.

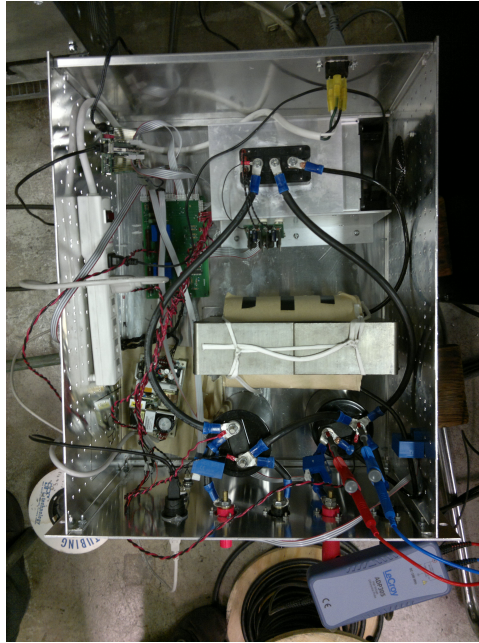


Figure A.6: Bi-directional dc-dc converter

The load bank is shown in Figure A.7. It consists of three identical sets of resistors. Each set has nine resistors in parallel: three 10 Ω , two 50 Ω , and four 25 Ω . The three sets can be connected in series to serve as a single-phase load, or wye-connected as a three-phase load.

The three-phase inverter and its output LC filter are shown in Figure A.8 and Figure A.9, respectively. The dc link capacitance is 680 μF . The filter inductance is

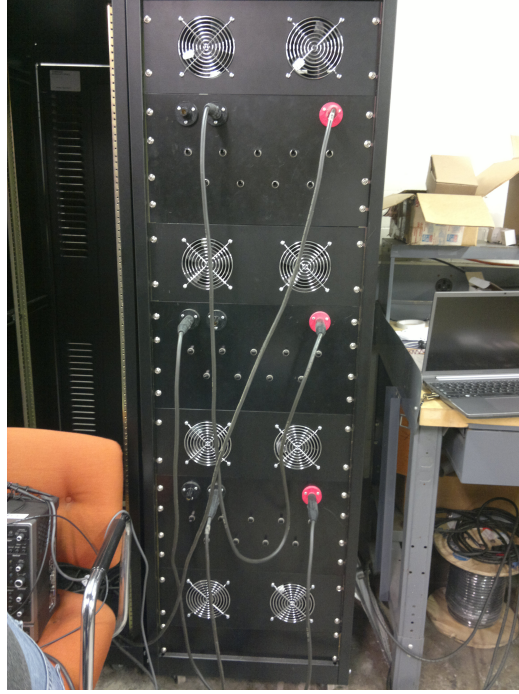


Figure A.7: Load bank

0.276 mH and the line-to-line capacitance is $8\ \mu\text{F}$.

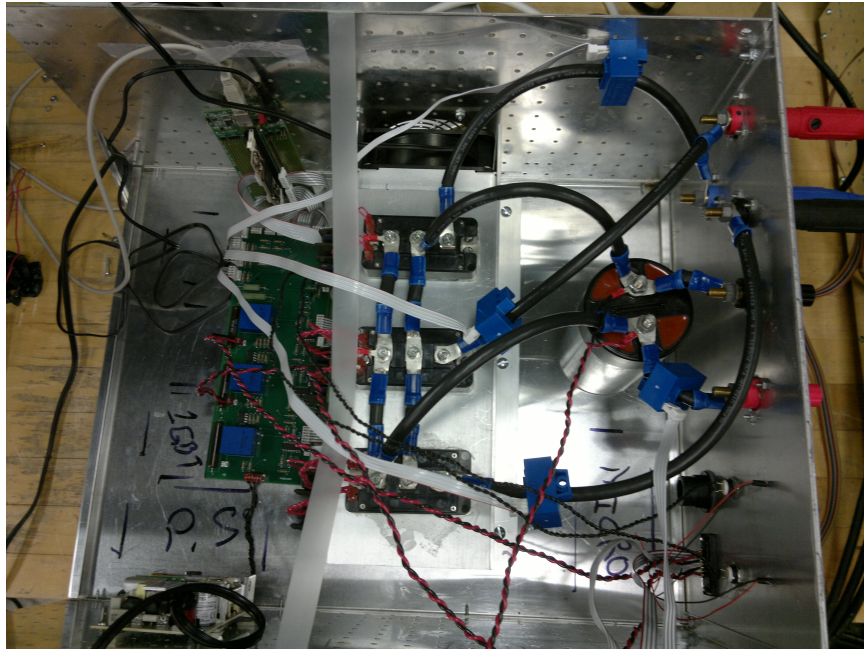


Figure A.8: Three-phase inverter

The grid connected transformer is shown in Figure A.10. The line-to-line voltage



Figure A.9: Three-phase inverter output LC filter

is 120 V.

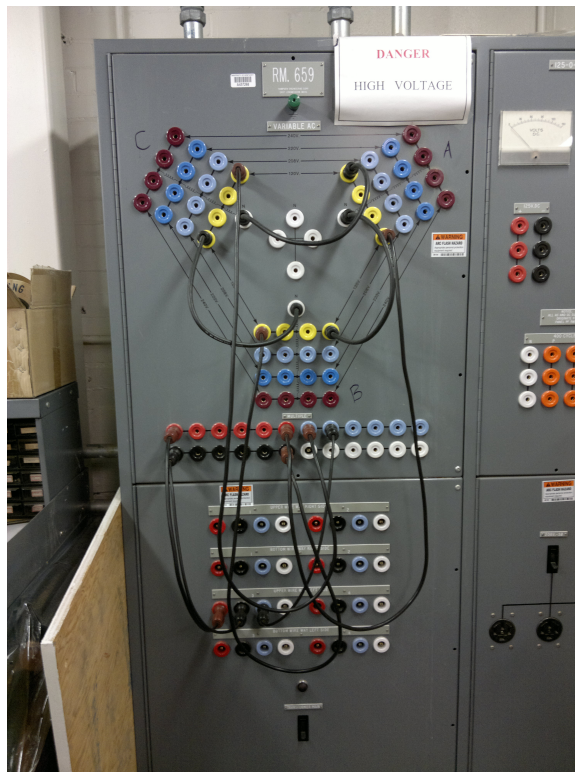


Figure A.10: Grid connected transformer

The permanent magnet brushless dc motor is shown in Figure A.11. It is a six pole 8 HP machine.

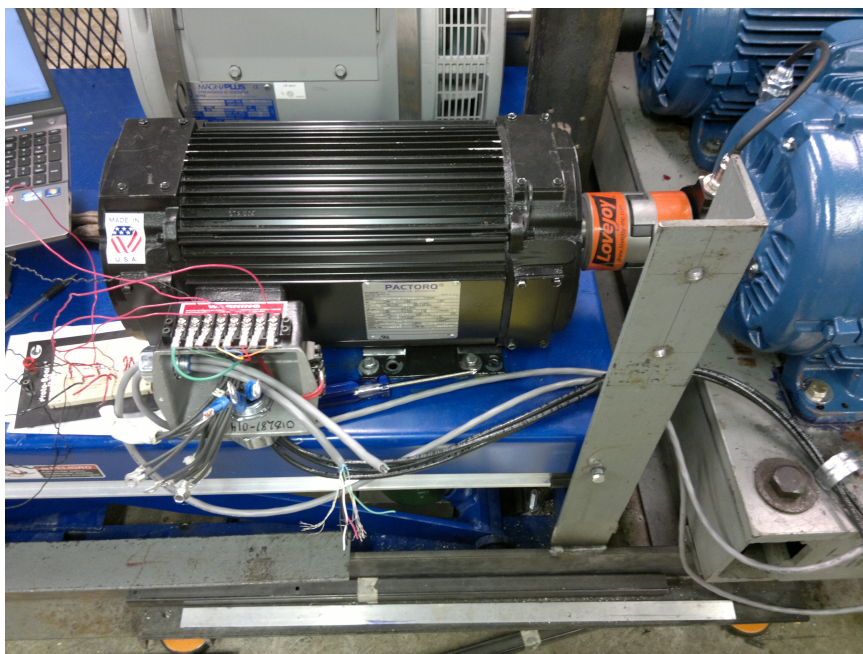


Figure A.11: Brushless dc permanent magnet motor

Bibliography

- [1] M. V. Chary, N. Sreenivasulu, K. N. Rao, and D. Saibabu, "Energy saving through vfds for fan drives in tobacco threshing plants," in *Proc. of IEEE Int. Conf. on Industrial Technology*, 2000, pp. 606–608.
- [2] M. Teitel, A. Levi, Y. Zhao, M. Barak, E. Bar-lev, and D. Shmuel, "Energy saving in agricultural buildings through fan motor control by variable frequency drives," *Energy and Buildings*, vol. 40, no. 6, pp. 953–960, 2008.
- [3] M. Lnnberg, "Variable speed drives for energy savings in hospitals," *World Pumps*, vol. 2007, no. 494, pp. 20–24, 2007.
- [4] A. Emadi, S. Williamson, and A. Khaligh, "Power electronics intensive solutions for advanced electric, hybrid electric, and fuel cell vehicular power systems," *IEEE Trans. Power Electron.*, vol. 21, no. 3, pp. 567–577, 2006.
- [5] G. M. Vosters, T. J. Hassell, W. W. Weaver, and J. Wolffe, "Optimal control of power electronic converters for traction applications," in *Vehicle Power and Propulsion Conf.*, 2011, pp. 1–5.
- [6] A. Emadi, L. Young Joo, and K. Rajashekara, "Power electronics and motor drives in electric, hybrid electric, and plug-in hybrid electric vehicles," *IEEE Trans. Ind. Electron.*, vol. 55, no. 6, pp. 2237–2245, 2008.
- [7] J. A. P. Lopes, F. J. Soares, P. M. R. Almeida, P. C. Baptista, C. M. Silva, and T. L. Farias, "Quantification of technical impacts and environmental benefits of electric vehicles integration on electricity grids," in *8th Advanced Electromechanical Motion Systems & Electric Drives Joint Symposium*, 2009, pp. 1–6.
- [8] R. Sioshansi and P. Denholm, "Emissions impacts and benefits of plug-in hybrid electric vehicles and vehicle-to-grid services," *Environmental Science & Technology*, vol. 43, no. 4, pp. 1199–1204, 2009.
- [9] T. Kerekes, M. Liserre, R. Teodorescu, C. Klumpner, and M. Sumner, "Evaluation of three-phase transformerless photovoltaic inverter topologies," *IEEE Trans. Power Electron.*, vol. 24, no. 9, pp. 2202–2211, 2009.
- [10] N. A. Rahim, J. Selvaraj, and Krismadinata, "Hysteresis current control and sensorless mppt for grid-connected photovoltaic systems," in *Int. Symp. on Industrial Electronics*, Jun. 2007, pp. 572–577.
- [11] F. Blaabjerg, M. Liserre, and K. Ma, "Power electronics converters for wind turbine systems," in *Energy Conversion Congr. and Expo.*, Sept. 2011, pp. 281–290.

- [12] M. Zhao, Y. Ruan, Y. Shen, B. Te, and Q. Zhong, "Comparative study of vector control with direct power control for grid side converter of dfig wind power generation system," in *2011 Int. Conf. on Electrical and Control Engineering*, Sept. 2011, pp. 3398–3402.
- [13] M. Elbuluk and N. R. N. Idris, "The role power electronics in future energy systems and green industrialization," in *2nd Int. Power and Energy Conf.*, Dec. 2008, pp. 1–6.
- [14] C. C. Davidson, "Power transmission with power electronics," in *14th European Conf. on Power Electronics and Applications*, Aug. 2011, pp. 1–10.
- [15] S. Mehraeen, S. Jagannathan, and M. L. Crow, "Novel dynamic representation and control of power systems with facts devices," *IEEE Trans. Power Syst.*, vol. 25, no. 3, pp. 1542–1554, 2010.
- [16] T. Jimichi, H. Fujita, and H. Akagi, "A dynamic voltage restorer equipped with a high-frequency isolated dc-dc converter," in *Energy Conversion Congress and Expo.*, Sept. 2009, pp. 1459–1465.
- [17] V. F. Corasaniti, M. B. Barbieri, P. L. Arnera, and M. I. Valla, "Hybrid active filter for reactive and harmonics compensation in a distribution network," *IEEE Trans. Ind. Electron.*, vol. 56, no. 3, pp. 670–677, 2009.
- [18] M. M. Adibi, N. Martins, and E. H. Watanabe, "The impacts of facts and other new technologies on power system restoration dynamics," in *Power and Energy Society General Meeting*, Jul. 2010, pp. 1–6.
- [19] P. K. Steimer, "Enabled by high power electronics - energy efficiency, renewables and smart grids," in *Int. Power Electronics Conf.*, Jun. 2010, pp. 11–15.
- [20] J. A. Momoh, "Smart grid design for efficient and flexible power networks operation and control," in *Power Systems Conf. and Expo.*, Mar. 2009, pp. 1–8.
- [21] F. Z. Peng, L. Hui, S. Gui-Jia, and J. S. Lawler, "A new ZVS bidirectional dc-dc converter for fuel cell and battery application," *IEEE Trans. Power Electronics*, vol. 19, no. 1, pp. 54–65, 2004.
- [22] A. Kirubakaran, S. Jain, and R. K. Nema, "Simulation and performance evaluation of 10 kw two stage power electronic interface for fuel cell based power supply system," in *Int. Conf. on Power Systems*, 2009, pp. 1–6.
- [23] W. Lei, W. Zhan, and L. Hui, "Asymmetrical duty cycle control and decoupled power flow design of a three-port bidirectional dc-dc converter for fuel cell vehicle application," *IEEE Trans. Power Electronics*, vol. 27, no. 2, pp. 891–904, 2012.
- [24] A. W. N. Husna, S. F. Siraj, and M. Z. Ab Muin, "Modeling of dc-dc converter for solar energy system applications," in *Symp. on Computers & Informatics*, 2012, pp. 125–129.

- [25] K. H. Mohamed, N. C. Sahoo, and T. B. Ibrahim, "Design of converters for wave energy conversion system," in *4th Int. Conf. on Intelligent and Advanced Systems*, vol. 1, 2012, pp. 491–496.
- [26] Y. Zhou, D. E. Macpherson, W. Blewitt, and D. Jovicic, "Comparison of dc-dc converter topologies for offshore wind-farm application," in *6th IET Int. Conf. on Power Electronics, Machines and Drives*, 2012, pp. 1–6.
- [27] B. M. Shagar, S. Vinod, and S. Lakshmi, "Design of dc - dc converter for hybrid wind solar energy system," in *Int. Conf. on Computing, Electronics and Electrical Technologies*, 2012, pp. 429–435.
- [28] N. Phillip, O. Maganga, K. J. Burnham, J. Dunn, C. Rouaud, M. A. Ellis, and S. Robinson, "Modelling and simulation of a thermoelectric generator for waste heat energy recovery in low carbon vehicles," in *2nd Int. Symp. on Environment Friendly Energies and Applications*, 2012, pp. 94–99.
- [29] B. Ren, D. Wang, C. Mao, J. Qiu, and J. Zhao, "Analysis of full bridge dc-dc converter in power system," in *4th Int. Conf. on Electric Utility Deregulation and Restructuring and Power Technologies*, 2011, pp. 1242–1245.
- [30] M. Suetomi, D. Imamichi, S. Matsumoto, D. Ueda, Y. Jong-Ruey, Y. Ishizuka, L. Wengzong, and H. Matsuo, "A novel bidirectional dc-dc converter with high power efficiency for isolation in high voltage dc power feeding systems," in *33rd Int. Telecommunications Energy Conf.*, 2011, pp. 1–4.
- [31] M. Castilla, J. Miret, A. Camacho, J. Matas, and L. de Vicuna, "Reduction of current harmonic distortion in three-phase grid-connected photovoltaic inverters via resonant current control," *IEEE Trans. Ind. Electron.*, vol. 60, no. 4, pp. 1464–1472, Apr. 2013.
- [32] M. Huang, F. Blaabjerg, Y. Yang, and W. Wu, "Step by step design of a high order power filter for three-phase three-wire grid-connected inverter in renewable energy system," in *4th Int. Symp. Power Electronics for Distributed Generation Systems (PEDG)*, Jul. 2013, pp. 1–8.
- [33] G. Han, Y. Xia, and W. Min, "Study on the three-phase PV grid-connected inverter based on deadbeat control," in *IEEE Power Engineering and Automation Conf. (PEAM)*, Sept. 2012, pp. 1–4.
- [34] L. Li, K. Smedley, and T. Jin, "New three-phase inverter for UPS application," in *41st Annu. Industry Applications Conf.*, vol. 4, Oct. 2006, pp. 1679–1685.
- [35] S. Jiang, D. Cao, Y. Li, J. Liu, and F. Z. Peng, "Low-THD, fast-transient, and cost-effective synchronous-frame repetitive controller for three-phase UPS inverters," *IEEE Trans. Power Electron.*, vol. 27, no. 6, pp. 2994–3005, Jun. 2012.

- [36] J. S. Lim, C. Park, J. Han, and Y. I. Lee, "Robust tracking control of a three-phase dc - ac inverter for UPS applications," *IEEE Trans. Ind. Electron.*, vol. 61, no. 8, pp. 4142–4151, Aug. 2014.
- [37] B. Varaticeanu, P. Minciunescu, S. Marinescu, and V. Racicovschi, "A novel brushless motor/generator for electric vehicles," in *8th International Symp.on Advanced Topics in Electrical Engineering (ATEE)*, 2013, pp. 1–4.
- [38] Z. Zhu and D. Howe, "Electrical machines and drives for electric, hybrid, and fuel cell vehicles," *Proceedings of the IEEE*, vol. 95, no. 4, pp. 746–765, 2007.
- [39] M. Zeraoulia, M. Benbouzid, and D. Diallo, "Electric motor drive selection issues for HEV propulsion systems: A comparative study," *Veh. Technol.*, vol. 55, no. 6, pp. 1756–1764, 2006.
- [40] X. Huang, K. Bradley, A. Goodman, C. Gerada, P. Wheeler, J. Clare, and C. Whitley, "Fault-tolerant brushless dc motor drive for electro-hydrostatic actuation system in aerospace application," in *41th Industry Applications Conf.*, vol. 1, Oct. 2006, pp. 473–480.
- [41] X. Huang, A. Goodman, C. Gerada, Y. Fang, and Q. Lu, "A single sided matrix converter drive for a brushless dc motor in aerospace applications," *IEEE Trans. Ind. Electron.*, vol. 59, no. 9, pp. 3542–3552, Sept 2012.
- [42] V. Veena and R. Praveen, "Mathematical modeling of advanced PMBLDC motor drive for aerospace application," in *Annu. Int. Conf. on Emerging Research Areas: Magnetism, Machines and Drives (AICERA/iCMMD)*, Jul. 2014, pp. 1–5.
- [43] S. Pal, "Direct drive high energy permanent magnet brush and brushless dc motors for robotic applications," in *IEE Colloquium on Robot Actuators*, Oct. 1991, pp. 12/1–12/4.
- [44] N. Hemati, J. Thorp, and M. C. Leu, "Robust nonlinear control of brushless dc motors for direct-drive robotic applications," *IEEE Trans. Ind. Electron.*, vol. 37, no. 6, pp. 460–468, Dec. 1990.
- [45] J. J. Carroll and D. Dawson, "Robust tracking control of a brushless dc motor with application to direct-drive robotics," in *IEEE Int. Conf. on Robotics and Automation*, vol. 1, May 1993, pp. 94–99.
- [46] C. Chan, "An overview of electric vehicle technology," *Proc. of the IEEE*, vol. 81, no. 9, pp. 1202–1213, 1993.
- [47] K. Chau, C. Chan, and C. Liu, "Overview of permanent-magnet brushless drives for electric and hybrid electric vehicles," *IEEE Trans. Ind. Electron.*, vol. 55, no. 6, pp. 2246–2257, 2008.

- [48] A. Azam, A. Jidin, N. Ngatiman, M. Jopri, M. Manap, A. Herlino, and N. Alias, "Current control of BLDC drives for EV application," in *7th. Int. Power Engineering and Optimization Conf.(PEOCO)*, 2013, pp. 411–416.
- [49] J. Mahdavi, A. Emadi, and H. A. Toliyat, "Application of state space averaging method to sliding mode control of PWM dc/dc converters," in *32nd IAS Annu. Meeting Industry Applications Conf.*, vol. 2, 1997, pp. 820–827.
- [50] V. S. C. Raviraj and P. C. Sen, "Comparative study of proportional-integral, sliding mode and fuzzy logic controllers for power converters," in *13th Industry Applications Conf.*, vol. 2, 1995, pp. 1651–1655.
- [51] T.-T. Song and H. S.-H. Chung, "Boundary control of boost converters using state-energy plane," *IEEE Trans. Power Electron.*, vol. 23, no. 2, pp. 551–563, 2008.
- [52] M. P. Kazmierkowski and L. Malesani, "Current control techniques for three-phase voltage-source PWM converters: a survey," *IEEE Trans. Ind. Electron.*, vol. 45, no. 5, pp. 691–703, 1998.
- [53] S. Buso, L. Malesani, and P. Mattavelli, "Comparison of current control techniques for active filter applications," *IEEE Trans. Ind. Electron.*, vol. 45, no. 5, pp. 722–729, 1998.
- [54] D. M. Brod and D. W. Novotny, "Current control of VSI-PWM inverters," *IEEE Trans. Ind. Appl.*, vol. IA-21, no. 3, pp. 562–570, 1985.
- [55] R. W. Erickson and D. Maksimovic, *Fundamentals of power electronics*, 1st ed. Norwell, Mass.: Kluwer Academic, 2001.
- [56] J. Wang, L. Liu, F. Zhang, C. Gong, and Y. Ma, "Modeling and analysis of hysteretic current mode control inverter," in *24th Annu. Applied Power Electronics Conf. and Expo.*, Feb. 2009, pp. 1338–1343.
- [57] Q. Yao and D. G. Holmes, "A simple, novel method for variable-hysteresis-band current control of a three phase inverter with constant switching frequency," in *Industry Applications Society Annu. Meeting*, Oct. 1993, pp. 1122–1129 vol.2.
- [58] P. Mattavelli, L. Rossetto, G. Spiazzi, and P. Tenti, "General-purpose sliding-mode controller for dc/dc converter applications," in *24th Annu. Power Electronics Specialists Conf.*, Jun. 1993, pp. 609–615.
- [59] L. J. Borle and C. V. Nayar, "Zero average current error controlled power flow for ac-dc power converters," *IEEE Trans. Power Electron.*, vol. 10, no. 6, pp. 725–732, 1995.
- [60] A. Shukla, A. Ghosh, and A. Joshi, "Hysteresis modulation of multilevel inverters," *IEEE Trans. Power Electron.*, vol. 26, no. 5, pp. 1396–1409, 2011.

- [61] M. Mohseni, S. M. Islam, and M. A. Masoum, "Enhanced hysteresis-based current regulators in vector control of dfig wind turbines," *IEEE Trans. Power Electron.*, vol. 26, no. 1, pp. 223–234, 2011.
- [62] K. Lee, F. C. Lee, and M. Xu, "A hysteretic control method for multiphase voltage regulator," *IEEE Trans. Power Electron.*, vol. 24, no. 12, pp. 2726–2734, 2009.
- [63] N. Prabhakar and M. K. Mishra, "Dynamic hysteresis current control to minimize switching for three-phase four-leg vsi topology to compensate nonlinear load," *IEEE Trans. Power Electron.*, vol. 25, no. 8, pp. 1935–1942, 2010.
- [64] M. Mohseni and S. M. Islam, "A new vector-based hysteresis current control scheme for three-phase PWM voltage-source inverters," *IEEE Trans. Power Electron.*, vol. 25, no. 9, pp. 2299–2309, 2010.
- [65] A. Schild, J. Lunze, J. Krupar, and W. Schwarz, "Design of generalized hysteresis controllers for dc-dc switching power converters," *IEEE Trans. Power Electron.*, vol. 24, no. 1, pp. 138–146, 2009.
- [66] S. Anshuman, G. Arindam, and J. Avinash, "Hysteresis current control operation of flying capacitor multilevel inverter and its application in shunt compensation of distribution systems," *IEEE Trans. Power Del.*, vol. 22, no. 1, pp. 396–405, 2007.
- [67] A. Shukla, A. Ghosh, and A. Joshi, "Improved multilevel hysteresis current regulation and capacitor voltage balancing schemes for flying capacitor multilevel inverter," *IEEE Trans. Power Electron.*, vol. 23, no. 2, pp. 518–529, 2008.
- [68] G. H. Bode and D. G. Holmes, "Implementation of three level hysteresis current control for a single phase voltage source inverter," in *31st Annual Power Electronics Specialists Conf.*, vol. 1, 2000, pp. 33–38.
- [69] P. Qian and Y. Zhang, "Study on hysteresis current control and its applications in power electronics," in *Electronics and Signal Processing*, ser. Lecture Notes in Electrical Engineering, W. Hu, Ed. Springer Berlin Heidelberg, 2011, vol. 97, pp. 889–895.
- [70] R. D. Middlebrook and S. Cuk, "A general unified approach to modeling switching-converter power stages," in *Proc. IEEE PESC Rec.*, 1976, pp. 18–34.
- [71] S.-C. Tan, Y. Lai, and C. Tse, "A family of PWM based sliding mode voltage controllers for basic DC-DC converters," in *IEEE Int. Symp. on Circuits and Systems*, May 2006, pp. 257–260.
- [72] D. G. Holmes, B. P. McGrath, and S. G. Parker, "A comparative evaluation of high performance current regulation strategies for vector controlled induction motor drives," in *Int. Symp. on Industrial Electronics*, Jul. 2010, pp. 3707–3714.

- [73] S. Gautam and R. Gupta, "Three-level inverter based shunt active power filter using generalized hysteresis current control method," in *Int. Conf. Power, Control and Embedded Systems*, 2010, pp. 1–6.
- [74] A. Shukla, A. Ghosh, and A. Joshi, "Hysteresis current control operation of flying capacitor multilevel inverter and its application in shunt compensation of distribution systems," *IEEE Trans. Power Del.*, vol. 22, no. 1, pp. 396–405, 2007.
- [75] P. C. Krause, O. Wasynczuk, and S. D. Sudhoff, *Analysis of electric machinery and drive systems*, 3rd ed. New York: Wiley-IEEE Press, 2013.
- [76] R. H. Ahmad, "Overmodulation control and performance factor evaluation for space vector modulation methods," pp. 277–277, 1998.
- [77] J. Sun and H. Grotstollen, "Optimized space vector modulation and regular-sampled PWM: a reexamination," in *31st IEEE Industry Applications Conference*, vol. 2, Oct. 1996, pp. 956–963.
- [78] S. Bowes and Y.-S. Lai, "The relationship between space-vector modulation and regular-sampled PWM," *IEEE Trans. Ind. Electron.*, vol. 44, no. 5, pp. 670–679, Oct. 1997.
- [79] K. Zhou and D. Wang, "Relationship between space-vector modulation and three-phase carrier-based pwm: a comprehensive analysis [three-phase inverters]," *IEEE Transactions on Ind. Electron.*, vol. 49, no. 1, pp. 186–196, Feb. 2002.
- [80] A. Kwasinski, P. Krein, and P. Chapman, "Time domain comparison of pulse-width modulation schemes," *IEEE Power Electronics Letters*, vol. 1, no. 3, pp. 64–68, Sept. 2003.
- [81] M. Ahmad, N. Idris, and A. Yatim, "Overmodulation and field weakening in direct torque control of induction motor drives," in *IEEE Int. Electric Machines Drives Conf.*, vol. 1, May 2007, pp. 398–402.
- [82] A. Jidin, M. Ahmad, N. Idris, and A. Yatim, "A simple overmodulation strategy in direct torque control of induction machines," in *5th Student Conf. on Research and Development*, Dec. 2007, pp. 1–5.
- [83] Y. Maeda, Y. Inoue, S. Morimoto, and M. Sanada, "Output power maximization of IPMSM using overmodulation region of direct torque control system," in *15th Int. Conf. on Electrical Machines and Systems (ICEMS)*, Oct. 2012, pp. 1–6.
- [84] N. Olarescu, S. Musuroi, C. Sorandaru, M. Weinmann, and S. Zeh, "Optimum current control for wide speed range operation of PMSM drive without regenerative unit utilizing PWM-VSI overmodulation," in *13th Int. Conf. on*

Optimization of Electrical and Electronic Equipment (OPTIM), May 2012, pp. 612–617.

- [85] J.-K. Seok and S.-K. Sul, “A new overmodulation strategy for induction motor drive using space vector PWM,” in *10th annu. Applied Power Electronics Conference and Exposition*, vol. 1, no. 0, Mar. 1995, pp. 211–216.
- [86] G. Dong and O. Ojo, “A generalized over-modulation methodology for current regulated three-phase voltage source converters,” in *39th Industry Applications Conf.*, vol. 4, Oct 2004, pp. 2216–2223.
- [87] R. Park, “Two-reaction theory of synchronous machines generalized method of analysis-part i,” *Transactions of the American Institute of Electrical Engineers*, vol. 48, no. 3, pp. 716–727, Jul. 1929.
- [88] S. Charles and C. Vivekanandant, “Modelling and power quality enhancement of induction motor with soft starter using synchronous reference frame theory,” in *Int. Conf. on Sustainable Energy and Intelligent Systems (SEISCON)*, Jul. 2011, pp. 47–51.
- [89] J. Poza, E. Oyarbide, D. Roye, and M. Rodriguez, “Unified reference frame dq model of the brushless doubly fed machine,” *IEE Proc. Electric Power Applications*, vol. 153, no. 5, pp. 726–734, Sep. 2006.
- [90] A. Guha and G. Narayanan, “Average modeling of a voltage source inverter with dead-time in a synchronous reference frame,” in *IEEE Innovative Smart Grid Technologies - Asia (ISGT Asia)*, Nov. 2013, pp. 1–6.
- [91] A. Lorduy, A. Lazaro, A. Barrado, C. Fernandez, I. Quesada, and C. Lucena, “Simplified synchronous reference frame control of the three phase grid connected inverter,” in *Twenty-Fifth Annu. IEEE Applied Power Electronics Conference and Exposition (APEC)*, Feb. 2010, pp. 1026–1033.
- [92] J. Vasquez, J. Guerrero, M. Savaghebi, J. Eloy-Garcia, and R. Teodorescu, “Modeling, analysis, and design of stationary-reference-frame droop-controlled parallel three-phase voltage source inverters,” *IEEE Trans. Ind. Electron.*, vol. 60, no. 4, pp. 1271–1280, Apr. 2013.
- [93] Z. Qin, D. Sha, and X. Liao, “A three-phase boost-type grid-connected inverter based on synchronous reference frame control,” in *Twenty-Seventh Annu. IEEE Applied Power Electronics Conference and Exposition (APEC)*, Feb. 2012, pp. 384–388.
- [94] M. Lin, S. Tomioka, T. Nabeshima, T. Sato, and K. Nishijima, “A novel PWM control method for dc-dc converter with fast transient response,” in *IEEE 10th Int. Conf. on Power Electronics and Drive Systems (PEDS)*, 2013, pp. 663–667.

- [95] H. Shao, X. Li, C.-Y. Tsui, and W.-H. Ki, "A novel single-inductor dual-input dual-output dc-dc converter with PWM control for solar energy harvesting system," *IEEE Trans. Very Large Scale Integr. (VLSI) Syst.*, vol. 22, no. 8, pp. 1693–1704, Aug 2014.
- [96] S.-W. Wang, G.-H. Cho, and G.-H. Cho, "A high-stability emulated absolute current hysteretic control single-inductor 5-output switching dc-dc converter with energy sharing and balancing," in *IEEE Int. Solid-State Circuits Conf. Digest of Technical Papers (ISSCC)*, 2012, pp. 276–278.
- [97] A. Borrell, M. Castilla, J. Miret, J. Matas, and L. de Vicuna, "Simple low-cost hysteretic controller for multiphase synchronous buck converters," *IEEE Trans. Ind. Electron.*, vol. 58, no. 6, pp. 2355–2365, Jun. 2011.
- [98] Y. Xiaobo, L. Xiao, and G. Yong, "Sensor-less brushless dc motor control system design for electric vehicle," in *2011 Int. Conf. on Electronics, Communications and Control (ICECC)*, Sept. 2011, pp. 2829–2833.
- [99] S. Maity, "Dynamics and stability issues of a discretized sliding-mode controlled dc-dc buck converter governed by fixed-event-time switching," *IEEE Trans. Circuits Syst. I, Reg. Papers*, vol. 60, no. 6, pp. 1657–1669, Jun. 2013.
- [100] P. Bhatnagar and R. Nema, "Control techniques analysis of dc-dc converter for photovoltaic application using SIMSCAPE," in *5th India Int. Conf. on Power Electronics*, Dec. 2012.
- [101] J.-D. Park and Z. Ren, "Hysteresis-controller-based energy harvesting scheme for microbial fuel cells with parallel operation capability," *IEEE Trans. Energy Convers.*, vol. 27, no. 3, pp. 715–724, 2012.
- [102] D. Trevisan, S. Saggini, and P. Mattavelli, "Hysteresis-based mixed-signal voltage-mode control for dc-dc converters," in *Power Electronics Specialists Conf.*, 2007, pp. 2664–2670.
- [103] R. G. Palaniappan and J. Vithayathil, "A control strategy for reference wave adaptive current generation," *IEEE Trans. Ind. Electron. and Control Instrum.*, vol. IECI-27, no. 2, pp. 92–96, 1980.
- [104] H. Lin, T. Lipo, B.-I. Kwon, and S. Cheon, "Three-level hysteresis current control for a three-phase permanent magnet synchronous motor drive," in *7th Int. Power Electronics and Motion Control Conf. (IPEMC)*, vol. 2, Jun. 2012, pp. 1004–1008.
- [105] M. Prasad Reddy, T. Reddy, and B. Brahmaiah, "Vector based hysteresis current control scheme for vector controlled induction motor drives," in *15th Int. Conf. Advanced Computing Technologies (ICACT)*, Sept. 2013, pp. 1–7.

- [106] Y. Kobayashi and H. Funato, "Current control method based on hysteresis control suitable for single phase active filter with lc output filter," in *13th Power Electronics and Motion Control Conf.*, 2008, pp. 479–484.
- [107] D. Xu, J. Gu, H. Liu, and M. Gong, "Improved hysteresis current control for active power filter," in *2003 Int. Symp. on Industrial Electronics*, vol. 2, 2003, pp. 836–840.
- [108] Y. Suresh, A. Panda, and M. Suresh, "Real-time implementation of adaptive fuzzy hysteresis-band current control technique for shunt active power filter," *Power Electronics, IET*, vol. 5, no. 7, pp. 1188–1195, Aug. 2012.
- [109] C.-S. Lam, M.-C. Wong, and Y.-D. Han, "Hysteresis current control of hybrid active power filters," *Power Electronics, IET*, vol. 5, no. 7, pp. 1175–1187, Aug. 2012.
- [110] C. Chiarelli, L. Malesani, S. Pirondini, and P. Tomasin, "Single-phase, three-level, constant frequency current hysteresis control for UPS applications," in *5th European Conf. on Power Electronics and Applications*, vol. 4, Sept. 1993, pp. 180–185.
- [111] Y. Qin and S. Du, "A novel adaptive hysteresis band current control using a DSP for a power factor corrected on-line UPS," in *23rd Int. Conf. on Industrial Electronics, Control and Instrumentation*, vol. 1, Nov. 1997, pp. 208–212.
- [112] H. T. Mokui, M. Mohseni, and M. A. S. Masoum, "Implementation of space vector based hysteresis current control for full converter wind generation system," in *Innovative Smart Grid Technologies Asia*, 2011, pp. 1–7.
- [113] J. Suul, K. Ljokelsoy, T. Midtsund, and T. Undeland, "Synchronous reference frame hysteresis current control for grid converter applications," *IEEE Trans. Ind. Appl.*, vol. 47, no. 5, pp. 2183–2194, Sept. 2011.
- [114] M. A. Elsayharty, M. S. Hamad, and H. A. Ashour, "Digital hysteresis current control for grid-connected converters with LCL filter," in *37th Annu. Industrial Electronics Society Conf.*, 2011, pp. 4685–4690.
- [115] H. Diab, H. El-Helw, and H. Talaat, "Intelligent maximum power tracking and inverter hysteresis current control of grid-connected PV systems," in *Int. Conf. on Advances in Power Conversion and Energy Technologies (APCET)*, Aug. 2012, pp. 1–5.
- [116] Y. Fong-Cheng, C. Chih-Chiang, C. Jiann-Jong, H. Yuh-Shyan, and L. Wen-Ta, "Hysteresis-current-controlled buck converter suitable for li-ion battery charger," in *Int. Conf. on Communications, Circuits and Systems Proc.*, vol. 4, 2006, pp. 2723–2726.
- [117] P. Krein, *Geometric control for power converters*, 1st ed. New York, NY: Oxfors Univ. Press, 1998, ch. 17, pp. 663–695.

- [118] S. Huerta, P. Alou, J. Oliver, O. Garcia, J. Cobos, and A. Abou-Alfotouh, "Nonlinear control for dc-dc converters based on hysteresis of the c_{OUT} current with a frequency loop to operate at constant frequency," *IEEE Trans. Ind. Electron.*, vol. 58, no. 3, pp. 1036–1043, 2011.
- [119] W. Lu, X. Wu, M. Zhao, and M. Chen, "Self-adaptive window control technique for hysteretic buck converter with constant frequency," in *IEEE Int. Conf. on Electron Devices and Solid State Circuit (EDSSC)*, 2012, pp. 1–2.
- [120] H. Vahedi, E. Pashajavid, and K. Al-Haddad, "Fixed-band fixed-frequency hysteresis current control used in APFs," in *38th Ann. Conf. on IEEE Industrial Electronics Society*, 2012, pp. 5944–5948.
- [121] G. Vazquez, P. Rodriguez, R. Ordonez, T. Kerekes, and R. Teodorescu, "Adaptive hysteresis band current control for transformerless single-phase pv inverters," in *35th Annu. Conf. of Industrial Electronics*, 2009, pp. 173–177.
- [122] B. Bose, "An adaptive hysteresis-band current control technique of a voltage-fed PWM inverter for machine drive system," *IEEE Trans. Ind. Electron.*, vol. 37, no. 5, pp. 402–408, 1990.
- [123] A. S. Lock and E. R. da Silva, "Improved hysteresis current control of a single phase, three level, double pfc converter," in *Power Electronics Specialists Conf.*, 2007, pp. 1326–1330.
- [124] V. M. Nguyen and C. Q. Lee, "Tracking control of buck converter using sliding-mode with adaptive hysteresis," in *26th Annu. Power Electronics Specialists Conf.*, vol. 2, 1995, pp. 1086–1093.
- [125] K. B. Mohanty, "A direct torque controlled induction motor with variable hysteresis band," in *11th Int. Conf. on Computer Modeling and Simulation*, Mar. 2009, pp. 405–410.
- [126] A. Naik, B. Chitti Babu, and A. Panda, "Improved performance of adaptive hysteresis current controller based vector control of PMSM drive system," in *IEEE Students' Technology Symposium (TechSym)*, Jan. 2011, pp. 303–309.
- [127] L. Jun and W. Dazhi, "Study and simulation of a novel hysteresis current control strategy," in *2nd Int. Conf. on Intelligent Computation Technology and Automation*, vol. 2, Oct. 2009, pp. 306–309.
- [128] D. Holmes, R. Davoodnezhad, and B. McGrath, "An improved three-phase variable-band hysteresis current regulator," *IEEE Trans. Power Electron.*, vol. 28, no. 1, pp. 441–450, Jan. 2013.
- [129] P. Ghani, A. A. Chiane, and H. Kojabadi, "An adaptive hysteresis band current controller for inverter base DG with reactive power compensation," in *1st Power Electronic Drive Systems Technologies Conf. (PEDSTC)*, Feb. 2010, pp. 429–434.

- [130] L. Corradini, A. Bjeletic, R. Zane, and D. Maksimovic, "Fully digital hysteretic modulator for dc-dc switching converters," *IEEE Trans. Power Electron.*, vol. 26, no. 10, pp. 2969–2979, 2011.
- [131] S. Maity and Y. Suraj, "Analysis and modeling of an FFHC-controlled dc-dc buck converter suitable for wide range of operating conditions," *IEEE Trans. Power Electron.*, vol. 27, no. 12, pp. 4914–4924, 2012.
- [132] R. R. Chan, Y. Lee, S. Sudhoff, and E. Zivi, "Evolutionary optimization of power electronics based power systems," *IEEE Trans. Power Electron.*, vol. 23, no. 4, pp. 1907–1917, 2008.
- [133] P. Zhang, X. Wen, and J. Liu, "Feed-forward control for stability improvement in cascaded system," in *Int. Conf. on Electrical and Control Engineering (ICECE)*, Jun. 2010, pp. 3746–3749.
- [134] A. Emadi, "Modeling and analysis of multiconverter dc power electronic systems using the generalized state-space averaging method," *IEEE Trans. Ind. Electron.*, vol. 51, no. 3, pp. 661–668, June 2004.
- [135] M. Jalla, A. Emadi, G. Williamson, and B. Fahimi, "Modeling of multiconverter more electric ship power systems using the generalized state space averaging method," in *30th Annu. Conf. of IEEE Industrial Electronics Society*, vol. 1, Nov 2004, pp. 508–513.
- [136] C. Nwankpa, J. Jimenez, and S. Jayasuriya, "Modeling and simulation of information-embedded multi-converter power systems," in *IEEE Int. Symp. on Circuits and Systems (ISCAS)*, 2013, pp. 1544–1547.
- [137] Z. Amjadi and S. Williamson, "Power-electronics-based solutions for plug-in hybrid electric vehicle energy storage and management systems," *IEEE Trans. Ind. Electron.*, vol. 57, no. 2, pp. 608–616, 2010.
- [138] X. Wang, F. Blaabjerg, and W. Wu, "Modeling and analysis of harmonic stability in an ac power-electronics-based power system," *IEEE Tran. Power Electron.*, vol. 29, no. 12, pp. 6421–6432, Dec. 2014.
- [139] S. Glover, S. Sudhoff, H. Hegner, and H. Robey, "Average value modeling of a hysteresis controlled dc/dc converter for use in electromechanical system studies," in *Proc. of the 1997 Naval Symposium on Electric Machines*, Newport, RI, 1997, pp. 77–84.
- [140] R. Redl, "Small-signal high-frequency analysis of the free-running current-mode-controlled converter," in *22nd Annu. Power Electronics Specialists Conf.*, 1991, pp. 897–906.
- [141] L. Yan-Fei and P. C. Sen, "Large-signal modeling of hysteretic current-programmed converters," *IEEE Trans. Power Electronics*, vol. 11, no. 3, pp. 423–430, 1996.

- [142] P. Garces, J. Calvente, R. Leyva, R. Giral, and L. Martinez-Salamero, "Simulation-oriented continuous model of hysteretic controlled dc-to-dc converters," in *Int. Symp. on Industrial Electronics*, 2007, pp. 633–637.
- [143] B. P. Loop, "Estimating regions of asymptotic stability of nonlinear systems with applications to power electronics systems," Ph.D. dissertation, Dept. Elect. Eng., Purdue Univ., West Lafayette, IN, 2005.
- [144] S. Mondal, B. Bose, V. Oleschuk, and J. O. P. Pinto, "Space vector pulse width modulation of three-level inverter extending operation into overmodulation region," *IEEE Trans. Power Electron.*, vol. 18, no. 2, pp. 604–611, Mar. 2003.
- [145] A. Gupta and A. Khambadkone, "A simple space vector PWM scheme to operate a three-level NPC inverter at high modulation index including overmodulation region, with neutral point balancing," *IEEE Trans. Ind. Appl.*, vol. 43, no. 3, pp. 751–760, May 2007.
- [146] K. A. Corzine, S. D. Sudhoff, and H. J. Hegner, "Analysis of a current-regulated brushless dc drive," *IEEE Trans. Energy Convers.*, vol. 10, no. 3, pp. 438–445, 1995.
- [147] S. G. R. Galam, S. Raghu, and N. Rajasekaran, "Design of feedback controller for boost converter using optimization technique," *International Journal of Power Electronics and Drive Systems (IJPEDS)*, vol. 3, no. 1, pp. 117–128, 2013. [Online]. Available: <http://iaesjournal.com/online/index.php/IJPEDS/article/view/1737>
- [148] V. Mishra, A. Tiwari, and N. Sharma, "A three phase pwm rectifier: A novel optimization technique to find scale factor of PI controller parameters of ac/dc PWM converter using genetic algorithms," *International Journal of Power Electronics and Drive Systems (IJPEDS)*, vol. 2, no. 2, pp. 151–159, 2012. [Online]. Available: <http://iaesjournal.com/online/index.php/IJPEDS/article/view/156>
- [149] J. Wang, B. Bao, J. Xu, G. Zhou, and W. Hu, "Dynamical effects of equivalent series resistance of output capacitor in constant on-time controlled buck converter," *IEEE Trans. Ind. Electron.*, vol. 60, no. 5, pp. 1759–1768, 2012.
- [150] E. Sakai and M. Nakahara, "Effect of ripple on frequency response characteristics of boost converter - analysis in consideration of ESR of output capacitor," in *31st Int. Telecommunications Energy Conf.*, 2009, pp. 1–6.
- [151] J. Wang, B. Bao, J. Xu, G. Zhou, and W. Hu, "Dynamical effects of equivalent series resistance of output capacitor in constant on-time controlled buck converter," *IEEE Trans. Ind. Electron.*, vol. 60, no. 5, pp. 1759–1768, 2013.
- [152] T. Qian, W. Wu, and W. Zhu, "Effect of combined output capacitors for stability of buck converters with constant on-time control," *IEEE Trans. Ind. Electron.*, vol. 60, no. 12, pp. 5585–5592, 2013.

- [153] “MATLAB R2012b,” The MathWorks Inc.
- [154] S. D. Sudhoff, B. P. Loop, J. Byoun, and A. M. Cramer, “A new procedure for calculating immittance characteristics using detailed computer simulations,” in *Power Electronics Specialists Conf.*, Jun. 2007, pp. 901–908.
- [155] M. N. F. Nashed, S. M. Mahmoud, M. Z. El-Sherif, and E. S. Abdel-Aliem, “Hysteresis current control of switched reluctance motor in aircraft applications,” *International Journal of Power Electronics and Drive Systems (IJPEDS)*, vol. 4, no. 3, pp. 376–392, 2014. [Online]. Available: <http://iaesjournal.com/online/index.php/IJPEDS/article/view/6210>
- [156] Y. Li, M. Jian, Y. Qiang, and L. Jiangyu, “A novel direct torque control permanent magnet synchronous motor drive used in electrical vehicle,” *International Journal of Power Electronics and Drive Systems (IJPEDS)*, vol. 1, no. 2, pp. 129–138, 2011. [Online]. Available: <http://iaesjournal.com/online/index.php/IJPEDS/article/view/141>
- [157] A. Ghamri, M. T. Benchouia, and A. Golea, “Sliding-mode control based three-phase shunt active power filter: Simulation and experimentation,” *Electric Power Components and Systems*, vol. 40, no. 4, pp. 383–398, 2012.
- [158] R. Ordoez and D. Sadarnac, “Hysteresis describing method for control of an active filter,” in *34th Annual Conference of IEEE Industrial Electronics*, Nov 2008, pp. 772–777.
- [159] D. M. E. Ingram and S. D. Round, “A fully digital hysteresis current controller for an active power filter,” *International Journal of Electronics*, vol. 86, no. 10.
- [160] B.-J. Kang and C.-M. Liaw, “Development of a robust random switching hysteresis pwm inverter for linear positioning control,” *Electric Power Components and Systems*, vol. 30, no. 7, pp. 741–767, 2002.
- [161] J. Rodriguez, J. Pontt, C. Silva, S. K. *, A. Liendo, and J. Rebolledo, “Hysteresis current control of a vector controlled induction motor and dtc: an assessment,” *International Journal of Electronics*, vol. 91, no. 11, pp. 639–651, 2004.
- [162] H. Komurcugil, “Combined use of double-band hysteresis current and proportional resonant control methods for single-phase ups inverters,” in *40th Annual Conference of the IEEE Industrial Electronics Society*, Oct 2014, pp. 1305–1311.
- [163] O. Husev, D. Vinnikov, C. Roncero-Clemente, and E. Romero-Cadaval, “New hysteresis current control for grid connected single-phase three-level quasi-z-source inverter,” in *Twenty-Ninth Annual IEEE Applied Power Electronics Conference and Exposition*, March 2014, pp. 1765–1770.
- [164] O. Varaprasad, D. Kumar, and D. Sarma, “Three level hysteresis current controlled vsi for power injection and conditioning in grid connected solar pv systems,” in *IEEE International Conference on Power Electronics, Drives and Energy Systems*, Dec 2014, pp. 1–5.

- [165] M. Kadjoudj, M. Benbouzid, C. Ghennai, and D. Diallo, "A robust hybrid current control for permanent-magnet synchronous motor drive," *IEEE Trans. Energy Convers.*, vol. 19, no. 1, pp. 109–115, Mar. 2004.
- [166] F. Wu, F. Feng, L. Luo, J. Duan, and L. Sun, "Sampling period online adjusting-based hysteresis current control without band with constant switching frequency," *IEEE Trans. Industrial Electronics*, vol. 62, no. 1, pp. 270–277, Jan 2015.
- [167] N. Belhaouchet and L. Rahmani, "Development of adaptive hysteresis-band current control of pwm three-phase ac chopper with constant switching frequency," *Electric Power Components and Systems*, vol. 37, no. 6, pp. 583–598, 2009.
- [168] A. E. M. Ehsani, "Multiconverter power systems and their applications," *Electric Power Components and Systems*, vol. 29, no. 10, pp. 949–963, 2001.
- [169] M. Chai, D. Xiao, R. Dutta, and J. Fletcher, "Overmodulation techniques for the three-to-five phase indirect matrix converter with space vector pwm," in *40th Annual Conference of the IEEE Industrial Electronics Society*, Oct 2014, pp. 3330–3336.
- [170] M. Dahidah, G. Konstantinou, and V. Agelidis, "A review of multilevel selective harmonic elimination pwm: Formulations, solving algorithms, implementation and applications," *IEEE Transactions on Power Electronics*, vol. 30, no. 8, pp. 4091–4106, Aug 2015.
- [171] H. Chen and A. Cramer, "Average-value modeling of hysteresis current controlled brushless dc motor drives," in *Transportation Electrification Conference and Expo*, June 2014, pp. 1–6.
- [172] H. Chen, A. M. Cramer, and B. P. Loop, "Slew-rate-limitation-based model of hysteresis current control in boost converters," *IEEE Trans. Ind. Electron.*, submitted for publication.
- [173] A. Emadi and M. Ehsani, "Multi-converter power electronic systems: definition and applications," in *32nd Annu. Power Electronics Specialists Conf.*, vol. 2, 2001, pp. 1230–1236.
- [174] M. Jalla, A. Emadi, G. Williamson, and B. Fahimi, "Real time state estimation of multi-converter more electric ship power systems using the generalized state space averaging method," in *30th Annu. Conf. of IEEE Industrial Electronics Society*, vol. 2, Nov. 2004, pp. 1514–1519.
- [175] A. Muntean, M. Radulescu, and A. Miraoui, "Torque analysis and control of a double-layer interior permanent-magnet synchronous motor for electric vehicle propulsion applications," in *8th Int. Symp. on Advanced Electromechanical Motion Systems Electric Drives Joint*, July 2009, pp. 1–8.

- [176] M. Farasat, E. Karaman, A. Trzynadlowski, and M. Fadali, “Hybrid field orientation and direct torque control for electric vehicle motor drive with an extended kalman filter,” in *IEEE Energytech*, May 2012, pp. 1–6.
- [177] A. Tashakori Abkenar and M. Motamed Ektesabi, “Direct torque control of in-wheel bldc motor used in electric vehicle,” in *IAENG Transactions on Engineering Technologies*, ser. Lecture Notes in Electrical Engineering, G.-C. Yang, S.-l. Ao, and L. Gelman, Eds. Springer Netherlands, 2013, vol. 229, pp. 273–286.
- [178] C. S. Mitter, “Device considerations for high current, low voltage synchronous buck regulators,” in *Proc. Wescon’ 97 Conf.*, 1997, pp. 281–288.

Vita

Hanling Chen was born in Xianyang, Shaanxi Province, P. R. China.

Education

2011-2015 Ph.D. Student, University of Kentucky

2010-2011 Master of Science, University of Kentucky

2008-2010 Bachelor of Science, University of Kentucky

2006-2008 Bachelor of Science, China University of Mining and Technology

Research Interest

Power electronics, power systems